

## 学位論文

Development of a Transmission Electron Microscope  
Adopting Two-Mode Superconducting RF Accelerating  
Cavity for Achieving Low Energy Dispersion  
(低エネルギー分散を実現する2モード超伝導加速空  
洞を採用した透過型電子顕微鏡の開発研究)

平成28年7月博士(理学)申請

東京大学大学院理学系研究科  
物理学専攻  
東直



## Abstract

This doctoral thesis reports the development and the study about the overall system design and the fundamental technologies for the world's first application of superconducting radio frequency (SRF) technology to a transmission electron microscopes (TEM).

A TEM is a vital tool to image sub-nanometer structures of specimens. It has been utilized in a wide range of fields including material science and biology. It is necessary to process specimens into layers as thin as a few tens of nm for the present TEM with the accelerating voltage of a few 100 kV. This is because the imaging power with high spatial resolution cannot be realized for thicker specimens as a consequence of the energy loss of the electron beam due to inelastic scatterings with the specimen and the decrease of the electron beam flux due to scatterings including elastic ones.

Recently a project that aims to adopt various technologies developed for high-energy accelerators into TEM is being carried out at High Energy Accelerator Research Organization (KEK) in Tsukuba, Ibaraki, Japan. This employs Radio Frequency (RF) resonant cavity which can generate accelerating fields as high as a few 10 MV/m in order to realize a new type of TEM with higher accelerating voltage than ever. Moreover superconducting RF cavity is adopted so that a high beam current comparable with conventional TEMs can be acquired and the accelerating field can be controlled more precisely than normal-conducting cavities. This new type of TEM, superconducting RF transmission electron microscope (SRF-TEM) is expected to enable the observation of thicker specimens than ever owing to its high accelerating voltage.

The SRF-TEM is capable of realizing a significant increase in  $e^-$  beam energy with a reasonably compact facility. However, the RF acceleration scheme generally used in high-energy accelerators causes larger beam energy dispersion which degrades the spatial resolution of the TEM. In this study, a new type of accelerating cavity named “two-mode cavity” in which two oscillating accelerating fields coexist was developed. The two-mode cavity is capable of flattening the sharp peak of the accelerating RF wave by superimposing one resonant mode of  $TM_{010}$  whose resonant frequency is 1.3 GHz on its double resonant mode of  $TM_{020}$  (2.6 GHz). A photocathode electron gun that is already developed is introduced into the SRF-TEM instead of a thermal electron or a cold field emission gun normally used for a conventional TEM. This can generate ultra-short bunches of a few ps and supply electron bunches precisely synchronized to the period of the accelerating field of the two-mode cavity. This is also expected to provide the good time resolution to SRF-TEM.

In this thesis, I describe the overall system design of the SRF-TEM and the establishment of the essential technologies for the SRF-TEM with 300 kV as a proof-of-principle prototype and a future 3 MV SRF-TEM. As the system design, we confirmed that the two-mode cavity can achieve low energy dispersion for the SRF-TEM with 300 kV and 3 MV by beam dynamics simulations.

Essential technologies are 1) the two-mode cavity which can generate the high accelerating gradient of about 10 MV/m with two resonant modes of  $TM_{010}$  and  $TM_{020}$ , and 2) the RF feedback system which can control the accelerating fields generated in the two-mode cavity precisely;  $(0.0012 \pm 0.0003) \%$  in terms of amplitude and  $(0.04 \pm 0.01)$  mdeg. in terms of phase for the  $TM_{010}$  mode and  $(0.0005 \pm 0.0004) \%$  and  $(0.03 \pm 0.01)$  mdeg. for the  $TM_{020}$  mode.

With the above, we opened up the road to the fully new TEM, SRF-TEM.



# Contents

<b>1</b>	<b>Introduction</b>	<b>1</b>
1.1	Significance of This Study . . . . .	1
1.1.1	Suggestion of Superconducting Radio Frequency Transmission Electron Microscope . . . . .	1
1.1.2	Development of Superconducting Radio Frequency Transmission Electron Microscope . . . . .	4
1.2	Structure of This Thesis . . . . .	6
<b>2</b>	<b>Present Situation of Transmission Electron Microscope and Limitation</b>	<b>7</b>
2.1	History of Transmission Electron Microscope . . . . .	7
2.2	System of Conventional Transmission Electron Microscope . . . . .	8
2.3	Imaging Theory of Transmission Electron Microscope . . . . .	10
2.4	Limit of Thickness in Observation by Transmission Electron Microscope . . . . .	13
<b>3</b>	<b>Concept of Superconducting Radio Frequency Transmission Electron Microscope</b>	<b>15</b>
3.1	System Configuration of Superconducting Radio Frequency Transmission Electron Microscope . . . . .	15
3.1.1	Two-mode Cavity . . . . .	17
3.1.2	Photocathode Electron Gun . . . . .	19
3.1.3	RF Feedback System for Two-mode Cavity . . . . .	19
3.2	Configuration Comparison between Conventional Transmission Electron Microscope and Superconducting Radio Frequency Transmission Electron Microscope . . . . .	20
3.3	Advantage of Superconducting Radio Frequency Transmission Electron Microscope . . . . .	21
3.3.1	Ability to Observe Thicker Specimen . . . . .	21
3.3.2	Downsizing Facility . . . . .	26
3.3.3	Acquisition of Time Resolution . . . . .	26
<b>4</b>	<b>System Design of Superconducting Radio Frequency Transmission Electron Microscope with 300 kV and 3 MV by Numerical Simulation of Beam</b>	

<b>Dynamics</b>	<b>29</b>
4.1 Scheme of Simulation Study Using General Particle Tracer . . . . .	29
4.1.1 Scheme of Numerical Simulation . . . . .	30
4.1.2 Scheme of Design Optimization . . . . .	31
4.2 Comparison of Two-mode Acceleration and One-mode Acceleration . . . . .	33
4.2.1 Method of Optimization . . . . .	33
4.2.2 Condition of Beam Dynamics Simulation . . . . .	34
4.2.3 Optimization Result of 300 keV Acceleration . . . . .	38
4.2.4 The optimization result of the 3 MV acceleration . . . . .	40
4.3 Requirement for Cavity Control . . . . .	42
<b>5 Development of Two-mode Cavity</b>	<b>45</b>
5.1 Fundamental Property and Design of Superconducting Cavity . . . . .	45
5.1.1 Nature of Superconductivity . . . . .	45
5.1.2 Resonant Mode in Pillbox . . . . .	46
5.1.3 Performance Index of Superconducting Cavity . . . . .	51
5.1.4 Design of Two-mode Cavity . . . . .	54
5.2 Fabrication of Two-mode Cavity . . . . .	56
5.2.1 Fabrication of Niobium Material . . . . .	56
5.2.2 Electron Beam Welding . . . . .	59
5.2.2.1 Surface Polishing . . . . .	62
5.2.2.2 Annealing . . . . .	68
5.2.2.3 High-pressure Washing . . . . .	68
5.2.2.4 Assembling . . . . .	69
5.3 Performance Test of Two-mode Cavity . . . . .	70
5.3.1 Setup . . . . .	70
5.3.2 Measurement Scheme . . . . .	72
5.3.2.1 Cable correction . . . . .	72
5.3.2.2 $Q_L$ measurement . . . . .	73
5.3.2.3 Power measurement . . . . .	75
5.3.3 Result . . . . .	76
5.4 Frequency Tuning Test of Two-mode Cavity . . . . .	77
<b>6 Development of Feedback Control System for Two-mode Cavity</b>	<b>81</b>
6.1 Source of Disturbance . . . . .	81
6.2 Setup of Feedback System For Two-mode Cavity . . . . .	82
6.3 Performance Test . . . . .	87
6.3.1 Single feedback . . . . .	87
6.3.2 Dual Feedback . . . . .	91
6.3.3 Consideration of Ultimate Control Stability . . . . .	96

<b>7</b>	<b>Ultimate Performance of Superconducting-Radio-Frequency Transmission Electron Microscope</b>	<b>97</b>
7.1	Performance Summary of Essential Technology for Superconducting Radio Frequency Transmission Electron Microscope . . . . .	97
7.1.1	Performance of the Two-mode Cavity . . . . .	97
7.1.2	Performance of RF Feedback System . . . . .	98
7.2	Estimation of Ultimate Performance of 300 kV Superconducting Radio Frequency Transmission Electron Microscope . . . . .	98
7.3	Future Perspective . . . . .	100
7.3.1	Fabrication of Cryostat for Two-mode Cavity . . . . .	100
7.3.2	Performance Evaluation of 300 kV SRF-TEM Prototype . . . . .	100
7.3.3	Future SRF-TEM with Higher Accelerating Voltage than 300 kV . . . . .	101
7.4	Achievement in This Thesis . . . . .	102
<b>A</b>	<b>Imaging Theory of High-Resolution Transmission Electron Microscope</b>	<b>105</b>
A.1	Phase Change by Electrostatic Potential . . . . .	105
A.2	Phase Shift at Objective Lens . . . . .	108
<b>B</b>	<b>Response Calculation of Superconducting Cavity by Lumped-constant Circuit Modeling</b>	<b>109</b>
B.1	Relation Between Cavity and Coupler . . . . .	109
B.2	Differential Equation for Superconducting Cavity and General Solution . . . . .	111
B.3	Stationary State of Superconducting Cavity . . . . .	113
B.4	Response to Pulsed Power . . . . .	115
B.5	Estimate $Q_0$ and $V_c$ . . . . .	117
	<b>Bibliography</b>	<b>119</b>



# Chapter 1

## Introduction

In this chapter, the bases of this thesis are introduced. Firstly, the significance of this study is summarized. Next, the structure of this thesis is explained.

### 1.1 Significance of This Study

In this section, a fully new TEM called superconducting radio frequency transmission electron microscope (SRF-TEM) is introduced. Our study to establish the fundamental technologies for SRF-TEM is summarized.

#### 1.1.1 Suggestion of Superconducting Radio Frequency Transmission Electron Microscope

##### Motivation of Observation of Thick Specimen

TEM is a powerful tool for imaging sub-nm structures of specimens. Generally, the observation object has to be sliced thin as  $O(10\text{ nm})$  with the accelerating voltage of  $O(100\text{ kV})$  for the observation with good spatial resolution. Destruction of the original configuration is inevitable in the process of slicing specimens. There are phenomena which appear depending on the thickness of the specimen, for example, magnetic vortices in high-temperature superconductors[1] and skyrmions[2].

Type II superconductors do not expel the applied magnetic flux completely and permit the penetrations of the magnetic flux in the form of vortices. The movements of this vortices generate heat dissipations. By observing these with TEMs, we understand the superconducting nature of the materials. However the appearance of this phenomenon depends on the thickness of the material. Tonomura observed the movement of the magnetic vortices with a material of Bi-2212 and the thickness was 400 nm with the 1 MV TEM[1].

A new spin configuration called skyrmion was observed in 2010[2]. This skyrmion takes the configuration like a vortex, and is expected to become a next-generation magnetic memory element with its high-stability and the ultra-low driving current. Until this point, skyrmions have been observed only in specimens as thin as  $O(10\text{ nm})$ . The condition for skyrmions to

appear depends on the thickness of the specimen, and there is a prediction that skyrmions appear in the 570 nm FeGe sample[3].

In order to image more genuine structures and study further new materials and phenomena with thicker specimens, we need to realize the accelerating voltage higher than 3 MV, which is the highest values accomplished in the conventional TEM, to suppress the energy spread of the electron beam at the specimen (Sec. 2.4). However, we cannot improve the accelerating voltage with the DC acceleration utilized in conventional TEMs for the discharge limitation<sup>1</sup>.

## Adoption of Radio Frequency Acceleration

In order to resolve this discharge limitation, we introduce the radio frequency acceleration scheme (RF acceleration) with resonant cavities. Generally, resonant cavities can generate high accelerating fields up to 100 MV/m. It is easy to realize the accelerating energy higher than 3 MV using RF acceleration with resonant cavities.

The normal conducting cavities made of copper can easily be fabricated. They do not need to be cooled with liquid helium during the operation. However, the dissipating power is too high to operate in continuous wave mode (CW mode) which means the cavity cannot be operated at 100 % duty. Therefore, the beam current cannot be sustained as the same level as the conventional TEM. Additionally, it is difficult to operate the normal conducting cavities with accurate field strength and waveform due to the deformation of the cavity by the heat.

## Choice of Superconducting Cavity

In order to acquire high beam current, we choose superconducting resonant cavities. It can generate high accelerating field as  $O(10 \text{ MV/m})$ , and be operated in CW mode. CW mode realizes the stable accelerating field as well as the high beam current.

However, the oscillating electric field generated by the superconducting cavity inevitably increases the energy spread. This is because the electron bunch with a finite length passes the electric field whose distribution changes from moment to moment in the cavity. This makes the spatial resolution of the TEM machine worse. According to the latest data[4], the stability of the electrostatic accelerating voltage  $\Delta V/V = 3.0 \times 10^{-7}$ . On the other hand, a general RF accelerating mode accelerates electrons with the spread of  $\Delta V/V > 1.0 \times 10^{-4}$ . Therefore, we have to develop a new SRF acceleration scheme in order to realize a high-voltage TEM with a good spatial resolution.

## Development of Two-mode Cavity

In order to suppress the energy spread of the beam, we developed a fully new superconducting cavity named “two-mode cavity”. This cavity has two resonant modes; the first-order mode

---

<sup>1</sup>The discharge limitation in the vacuum state is dependent on the material of electrodes and the surface condition, however it is generally about 40-50 kV with 1 mm gap[5].

$TM_{010}$  (1.3 GHz) and the second-order mode  $TM_{020}$  (2.6 GHz) illustrated in Figure 1.1. Superimposing the  $TM_{020}$  mode onto the  $TM_{010}$  mode, the flatter peak of the accelerating electric field can be generated (see Figure 1.2). With the two-mode cavity, we can suppress the energy spread compared with the conventional single mode acceleration with the  $TM_{010}$  mode. In addition, a photocathode electron gun is introduced instead of the thermal gun. This enables electron bunches to synchronize the resonant frequency of two-mode cavity; 1.3 GHz.

We call the TEM employing this two-mode cavity “SRF-TEM”. The history of superconducting cavities is long, however the two-mode cavity is the world’s first superconducting cavity that has two resonant mode. As described in Chapter 5, Its development is very challenging. In addition, in order to realize the energy dispersion low enough to get the good spatial resolution, it is needed to control two resonant mode with high accuracy at the same time. This is also main task for the SRF-TEM. The detail of the two-mode cavity and the two-mode acceleration are described in Chapter 3 .

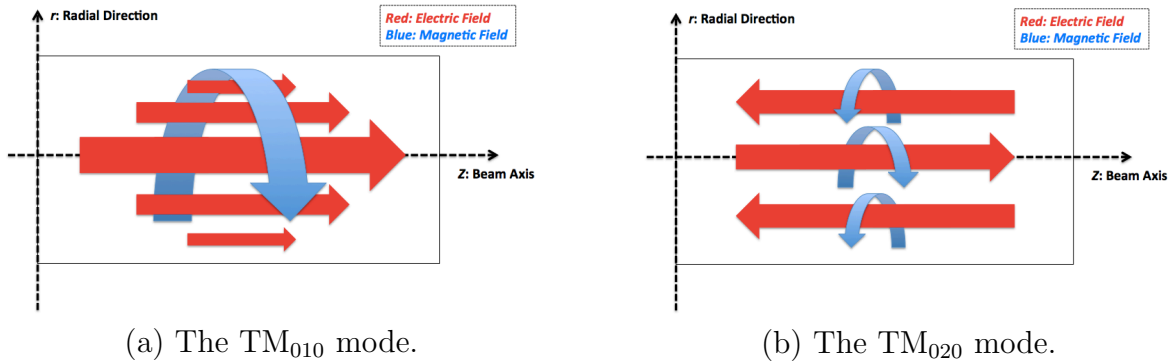


Figure 1.1: The distribution of the electromagnetic field utilized in the SRF-TEM.

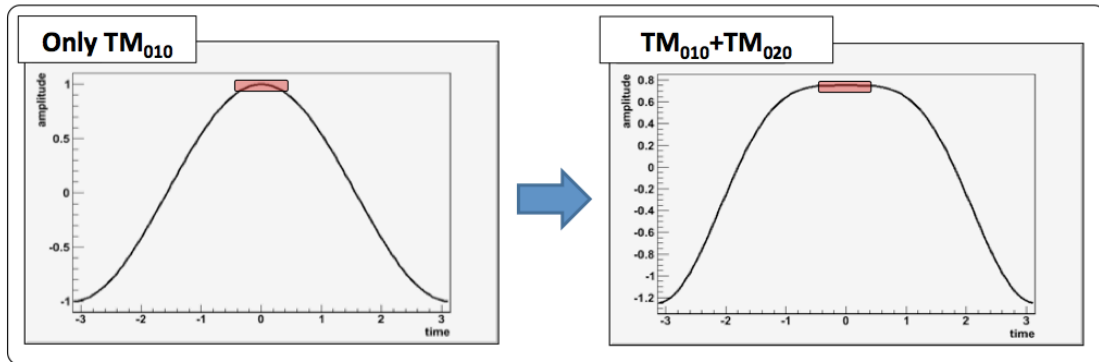


Figure 1.2: A schematic comparison of the single acceleration with only the  $TM_{010}$  mode and the dual acceleration with the  $TM_{010}$  mode and the  $TM_{020}$  mode. The time unit of the horizontal axis and the amplitude unit of the vertical axis are arbitrary.

## **Advantage of SRF-TEM**

The main advantage of the SRF-TEM is the ability of observing thick specimens. A calculation based on the TEM imaging theory has shown that a 10 MV SRF-TEM has the ability to observe about 100 times thicker specimens with 100 pm spatial resolution compared with the state-of-the-art 1.2 MV TEM in the case of aluminum film specimen.

This ability of observing thick specimens is expected with a compact facility owing to the accelerating field much higher than the conventional DC acceleration scheme. The state-of-the-art 1.2 MV TEM is as tall as about 10 m[6]. In contrast, our 1.0 MV SRF-TEM can be realized with the size of about 4 m.

In addition, the SRF-TEM is expected to provide good time resolution thanks to the bunched electron beam generated by the photocathode electron gun. The SRF-TEM can get the time resolution of 12  $\mu$ s for an assumed bunch intensity of 0.1 fC. Moreover, if the pumping probe method is employed, our SRF-TEM is able to acquire 2 ps time resolution.

### **1.1.2 Development of Superconducting Radio Frequency Transmission Electron Microscope**

In this section, the development plan of the SRF-TEM is explained. After that, the achievement in this thesis is summarized.

#### **Development Plan of SRF-TEM**

We are now developing the first prototype of SRF-TEM with 300 kV acceleration voltage. This is based on the conventional 300 kV TEM, H-9000 NAR. Figure 1.3 illustrates our development of the 300 kV prototype. In order to realize this, we have to design the overall system of the SRF-TEM. Technologies for the photocathode electron gun, the two-mode cavity and the RF feedback system have to be established. IN addition, 3 MV and 10 MV SRF-TEM are considered as the future machine that is superior to the present state-of-the-art TEM.

#### **Achievement in This Thesis**

This thesis explains my work of the system design of the SRF-TEM of 300 kV and 3 MV acceleration voltage and the establishment of the backbone technologies for the SRF-TEM. My work is summarized briefly as follows;

1. Simulated 3D beam dynamics for SRF-TEMs and confirmed that two-mode acceleration works effectively to reduce the energy spread compared with one-mode acceleration in the case of 300 kV acceleration and 3 MV acceleration,
2. Established the manufacturing process of the two-mode cavity and confirmed that the manufactured two-mode cavity satisfies the requirements for 300 kV SRF-TEM with the performance tests,

3. Developed the feedback system for the accelerating field generated by the two-mode cavity and confirmed that it satisfies the requirements for 300 kV SRF-TEM with the performance tests.

With the above, we opened up the road to the fully new TEM, SRF-TEM. This has the ability of observing specimens much thicker than the state-of-the-art TEM, and it is realized with more compact facility. The SRF-TEM is also expected to acquire the time resolution of  $O(\mu s)$  -  $O(ps)$ .

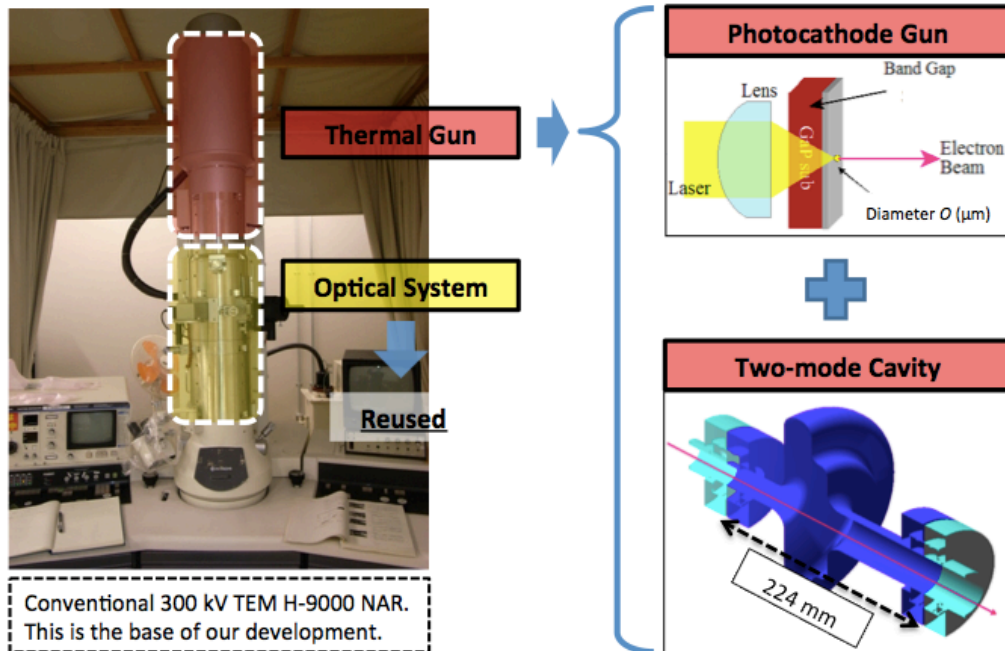


Figure 1.3: A concept of 300 kV SRF-TEM prototype development based on H-9000 NAR, conventional 300 kV TEM.

## 1.2 Structure of This Thesis

Here, the structure of this thesis is explained.

In chapter 2, the fundamental of the conventional TEM is introduced. Firstly, the history of TEM is described. After that, the general configuration of the present TEM is explained. Next, the imaging theory of TEM is introduced. Finally, the limitation of the observation for present TEMs in terms of energy losses of electron beams is described.

In chapter 3, the concept design and key technologies of the SRF-TEM are introduced. Next, the advantages of the SRF-TEM are explained in detail. Finally, the issues to realize the SRF-TEM is described and the quantitative requirements for the key technologies are set.

In chapter 4, the overall system designs of the SRF-TEM with the accelerating energy 300 kV and 3 MV are explained. These are based on the comparison of the two-mode acceleration and the one-mode acceleration. In addition, the requirements for the accelerating field of the two-mode cavity in the case of the 300 kV acceleration are defined. Next, the RF control error effects on the energy spread are investigated for the two-mode acceleration on the 300 kV SRF-TEM prototype.

Chapter 5 explains the fabrication of the two-mode cavity and its performance test.

Chapter 6 describes the configuration of the developed feedback system and its performance test.

Chapter 7 summarizes the results of the development of each fundamental technology and feedback the acquired performance values which were measured in each performance test to derive the ultimate performance of SRF-TEM in the 300 kV acceleration.

# Chapter 2

## Present Situation of Transmission Electron Microscope and Limitation

In this chapter,

1. the history of TEMs,
2. the system of TEMs,
3. the imaging theory of TEMs,
4. the limitation of the observation for present TEMs in terms of energy losses of electron beams.

are summarized.

### 2.1 History of Transmission Electron Microscope

TEM has been a strong tool to image various matters including industrial materials and biological ones. It has become an indispensable imaging device for semiconductor studies, batteries, magnets and biological matters (recently including iPS cells[7]). The development history of TEMs started when a limitation of a spatial resolution due to diffraction aberrations of optical microscopes would be overcome with the shorter wavelength of electrons. After the invention of TEM, the long successful history has been supported by the Japanese leading technology which gave a birth of an ultra-high voltage TEM ( $\sim 3$  MeV) to continue to establish a new record of the spatial resolution. However the improvement of the spatial resolution which was realized along with the shortening of de Broglie wavelengths was saturated. This was because spherical aberrations became the dominant contribution determining the spatial resolution. In late 1990s, Haider and others established the technology to correct spherical aberrations using the combination of quadrupole magnets or sextupole magnets[8]. With this new technology, the spatial resolutions better than 200 pm has been achieved with low voltage TEMs of up to 300 kV.

Now the best spatial resolution is recored by Hitachi Cooperation in Japan[4]. The TEM has the gun of cold field emission and the accelerating energy is 1.2 MV. Its spherical aberration is corrected to the third order. Using the 3 nm-thick specimen of GaN, the spatial resolution of 43 pm was achieved.

## 2.2 System of Conventional Transmission Electron Microscope

Here a general system of TEMs is explained. Figure 2.1 shows the overview of a conventional TEM. It has an electron gun, condenser lenses, a specimen part, an objective lens, an intermediate lens, a projector lens, an imaging detector from the top to the bottom. TEMs are electron beam accelerators as they have electron guns and accelerating parts as well as magnets to bend and focus beams. Thermal electron gun has been conventionally used, whereas the use of cold field emission gun is becoming more common. The radio frequency acceleration (RF acceleration) has rarely been used for TEMs, and generally TEMs employ electrostatic acceleration systems using Cockcroft-Walton circuits. TEMs' magnets are called "lenses" in analogy of the optical microscopes. It is the objective lens that determines TEM's performance dominantly. This has a strong magnetic field in order to focus electrons which pass thorough specimens and its aberrations (spherical and chromatic) limit the spatial resolution of TEMs. Above the objective lens, there is an objective aperture which cuts off electrons to determine the TEM performance. In the past, films used to be used as the imaging detector which can display images which are proportional to fluxes of electrons, though nowadays fluorescent screens are employed to convert electron signals into lights that are recored digitally by the CCD cameras. In the following, key components of TEMs necessary for later discussions will be explained in detail.

### Electron Gun

The electron gun is a crucial part to determine the quality of the beam. Today there are two main types of guns for TEMs; thermal electron guns which use  $\text{LaB}_6$  as cathodes and cold field emission guns which derive electrons using high electric fields. Photocathode electron guns which have been developed for high spin-polarized electron beams have now been applied in TEMs and our research is also employing this photocathode electron gun[9]. Table 2.1 compares these guns in several aspects. In this thesis, energy spread  $\Delta T_{\text{ini}}$  is the crucial parameter to affect the energy dispersion of the beam.

### Specimen

It is necessary to process the specimens so that features to observe can be seen. Specimens are needed to be thin enough to be observed as close as possible to the original structures with energy losses or electron beam flux losses, which would impair spatial resolution, limited as much as possible. Generally for TEMs with several 100 kV accelerating voltage, specimens

Table 2.1: A comparison of guns. Materials and each values are just typical ones.  $\Delta T_{\text{ini}}$  is an energy spread at its cathode.  $J_e$  is a current density and  $\beta$  is a brightness which is calculated dividing  $J_e$  by a solid angle. “Vacuum” means a general value needed to cooperate each gun.

Type of Source	Thermal [10]	Cold Field Emission [10]	Photocathode [11] [12]
Material	LaB <sub>6</sub>	W	GaAs-GaAsP
$\Delta T_{\text{ini}}$ [eV]	1.00	0.30	0.15
$J_e$ [A/m <sup>2</sup> ]	$\approx 10^6$	$\approx 10^9$	$\approx 10^6$
$\beta$ [A/m <sup>2</sup> sr]	$\approx 10^{10}$	$\approx 10^{12}$	$\approx 10^{11}$
Vacuum [Pa]	$< 10^{-4}$	$< 10^{-8}$	$< 10^{-8}$
Lifetime [hours]	$10^3$	$10^4$	10

have to be sliced to a few 10 nm of thickness<sup>1</sup>. Furthermore, in TEMs’ column, vacuum level

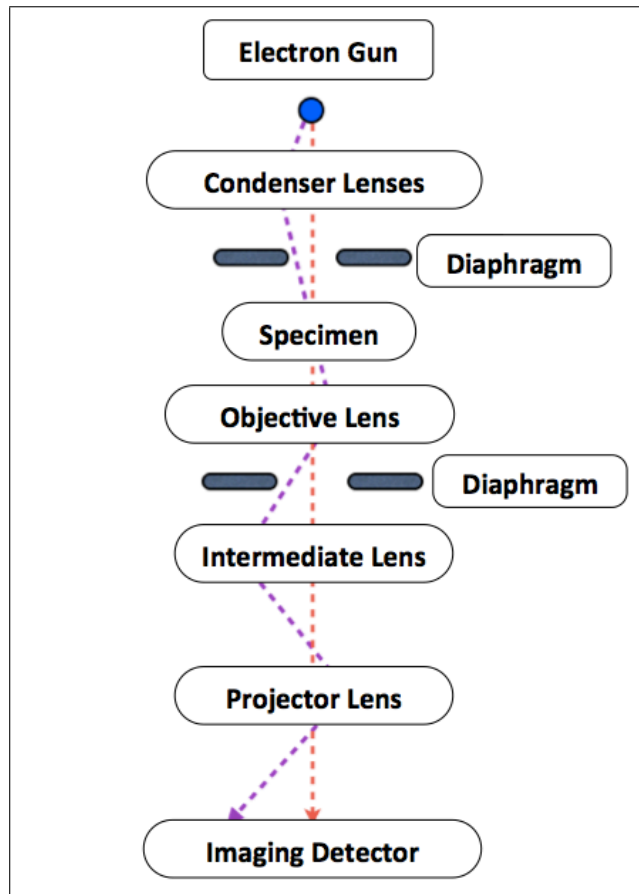


Figure 2.1: The overview of a conventional TEM.

<sup>1</sup>Needless to say, it depends on materials and density, more accurately “mass-thickness”.

has to be under  $O(10^{-3}\text{Pa})$  in order to avoid interferences of the electron beam with air and discharge problems, then specimens cannot be in wet state. Therefore when biological bodies are objects for observing, these have to be frozen.

## Objective Lens

The objective lens plays an important role in TEMs to determine spatial resolution. It has two aberration; spherical and chromatic. Spherical aberration arises from the difference of the focal length for each path of the electron due to the imperfection of the lens (deviation from the perfect convex lens). On the other hand, chromatic aberration is due to the difference of the focal length for different electron energy, and is affected by the finite energy spread of the electron beam.  $\Delta f$ , the quantity called “defocus” also influences the TEMs’ spatial resolution as well as aberrations. There are some definition for the sign of  $\Delta f$ . In this thesis, the stronger excitation than usual has minus sign called under-focus ( $\Delta f < 0$ ) and vice versa.

## 2.3 Imaging Theory of Transmission Electron Microscope

In this part, the imaging theory of TEMs is summarized. There are two ways to analyze the ability of TEM imaging; the scattering contrast scheme and the phase contrast scheme[13][14][15]. The scattering contrast scheme explains that the TEM image formation is made by the electron flux decrease due to scatterings. In contrast, the phase contrast scheme utilizes the phase change of the incident electrons by nucleus electrostatic potentials and lenses. Practical image simulation using the specimen structures is based on the phase changes and the wave functions. Therefore, we carried out the studies and developments based on the imaging performance analysis by the phase contrast scheme. Here a brief explanation of the theoretical basis of the phase contrast is made. More detail is described in Appendix A.

The phase contrast theory uses a wave function to express the phase change of electron wave by a nucleus. This wave function  $\psi_i$  is written as

$$\psi_i = \exp(i\sigma V_p), \quad (2.3.1)$$

where  $\sigma$  is the interaction coefficient of electrons and specimens and  $V_p$  is the projection potential which is the result of integration of all potentials along the beam axis (here,  $z$ ),

$$\int V(x, y, z)dz = V_p(x, y). \quad (2.3.2)$$

In practical usage, this wave function is modified with “lens transfer function (LTF)”, and

Table 2.2: The notation for lens transfer functions.

Symbol	Definition	Unit
$C_3$	coefficient of the third spherical aberration	m
$C_5$	coefficient of the fifth spherical aberration	m
$C_c$	coefficient of the chromatic aberration	m
$\Delta f$	defocus	m
$\Delta$	defocus spread	m
$\sigma(x)$	image spread	m
$\beta$	illumination tilt spread	rad

is expressed as

$$\text{LTF} = \exp(-i\chi_{\text{ps}}) \exp(\chi_{\text{fs}}) \exp(\chi_{\text{is}}) \exp(\chi_{\text{sc}}) \quad (2.3.3)$$

$$\chi_{\text{ps}} = \frac{\pi}{2} C_3 \lambda^3 u^4 + \frac{\pi}{3} C_5 \lambda^5 u^6 + \pi \Delta f \lambda u^2 \quad (2.3.4)$$

$$\chi_{\text{fs}} = -\frac{\pi^2}{2} \lambda^2 \Delta^2 u^4 \quad (2.3.5)$$

$$\chi_{\text{is}} = -2\pi^2 \sigma^2(x) u^2 \quad (2.3.6)$$

$$\chi_{\text{sc}} = -\pi^2 u_0^2 \{ (C_3 \lambda^2 u^2 + \Delta f) \lambda u \}^2, \quad (2.3.7)$$

where  $u$  is reciprocal space coordinate corresponding to  $x$ . Other notations are explained in Table 2.2. Image spread  $\sigma(x)$  is the  $x$  axis component of the mechanical fluctuation at the detector level due to stage deviation and column vibration.  $u_0$  is a physics quantity that satisfies  $u_0^2 = (\lambda/\beta)^2$  where  $\beta$  means the divergence angle of the electron beam at the specimen. The term  $\exp(-i\chi_{\text{ps}})$  is responsible for the spherical aberration of the objective lens and the defocus,  $\exp(\chi_{\text{fs}})$  accounts for the chromatic aberration of the objective lens, the energy dispersion of the beam and the deviation of the focal length for the instability of the current of the objective lens. Then defocus spread  $\Delta$  is given by

$$\Delta = C_c \sqrt{\left(\frac{\Delta T}{T}\right)^2 + \left(2\frac{\Delta J}{J}\right)^2}, \quad (2.3.8)$$

where  $\Delta T$  is the energy spread, and therefore  $\Delta T/T$  is the energy dispersion of the beam.  $\Delta J/J$  is the stability of the current of the objective lens which is generally  $O(10^{-5})$ .  $\exp(\chi_{\text{is}})$  is determined by the fluctuation of the imaging level along the horizontal axis and  $\exp(\chi_{\text{sc}})$  depends on the divergence angle of the beam against the specimen.

The phase wave function  $\psi_i$  is affected by the LTF above and modified as

$$\psi_i = 1 + i\sigma V_p \otimes \hat{F} [\exp(-i\chi_{\text{ps}} + \chi_{\text{R}})], \quad (2.3.9)$$

where  $\otimes$  represents convolution,  $\hat{F}$  stands for inverse Fourier transformation and  $\chi_{\text{R}}$  satisfies  $\chi_{\text{R}} = \chi_{\text{fs}} + \chi_{\text{is}} + \chi_{\text{sc}}$ . The image intensity  $I$  can be calculated as  $I = \psi_i \psi_i^*$ , thus

$$I = 1 + 2\sigma V_p \otimes \hat{F} [\sin(\chi_{\text{ps}}) \cdot \exp(\chi_{\text{fs}} + \chi_{\text{is}} + \chi_{\text{sc}})]. \quad (2.3.10)$$

Here the example of Hitachi 1.2 MV aberration-corrected FE-TEM is considered[4]. Figure 2.2 shows its theoretical lens transfer function (LTF). The horizontal axis stands for reciprocal space coordinate  $u$  whose unit is  $\text{nm}^{-1}$ . The notation of each  $E$  is defined as follows;  $E_{\text{ps}} = \sin(\chi_{\text{ps}})$ ,  $E_{\text{fs}} = \exp(\chi_{\text{fs}})$ ,  $E_{\text{is}} = \exp(\chi_{\text{is}})$  and  $E_{\text{sc}} = \exp(\chi_{\text{sc}})$ . The thick yellow line represents  $\sin(\chi_{\text{ps}}) \cdot \exp(\chi_{\text{fs}} + \chi_{\text{is}} + \chi_{\text{sc}})$  which corresponds to the term under the inverse Fourier transformation. Therefore this quantity plays a role to carry the projected electrostatic potentials in the specimen to the image as well as the interaction coefficient  $\sigma$ . The inverse Fourier transformation of constant  $A$  is

$$\hat{F}[A] = A \cdot \delta(x). \quad (2.3.11)$$

Now replacing  $\sin(\chi_{\text{ps}}) \cdot \exp(\chi_{\text{fs}} + \chi_{\text{is}} + \chi_{\text{sc}})$  with  $A$ , we get

$$I = 1 + 2\sigma V_{\text{p}} \otimes \hat{F}[A] \quad (2.3.12)$$

$$= 1 + 2\sigma A V_{\text{p}}(x). \quad (2.3.13)$$

Here we define  $u_{\text{max}}$  as the maximum value of  $u$ , where the LTF ( $\sin(\chi_{\text{ps}}) \cdot \exp(\chi_{\text{fs}} + \chi_{\text{is}} + \chi_{\text{sc}})$ ) reduces to  $1/e^2 \simeq 0.135$ . This corresponds to the inverse of the spatial resolution  $\Delta r$  of the TEM. For Hitachi 1.2 MV FE-TEM,  $u_{\text{max}} = 23\text{nm}^{-1}$ , then  $\Delta r$  is estimated as 43nm. In the practical observation of 3 nm-thick GaN specimen, the spatial resolution of 43nm was confirmed.

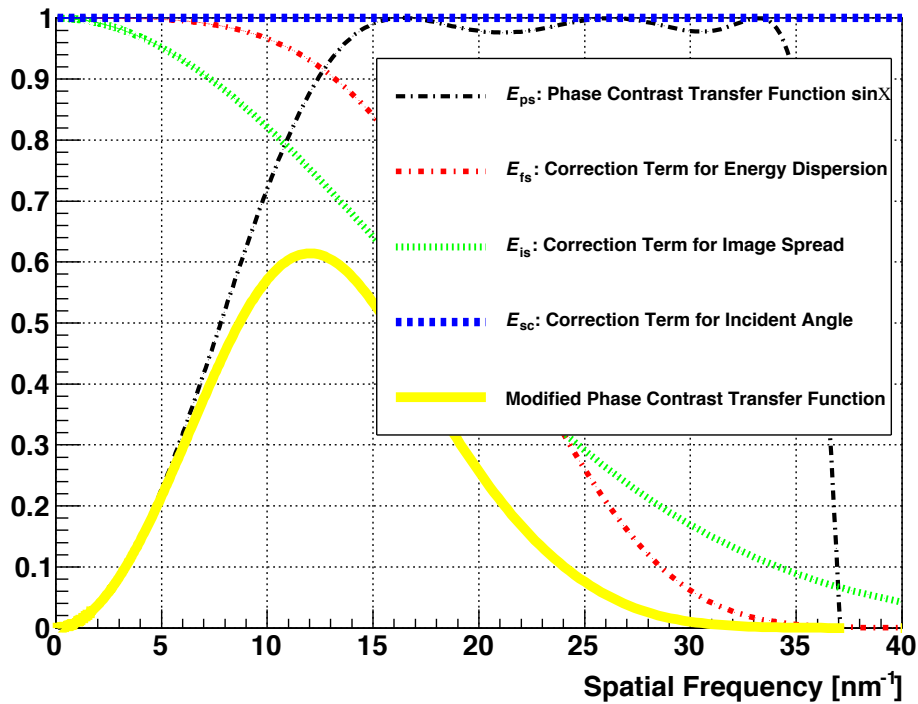


Figure 2.2: The lens transfer function of Hitachi 1.2 MV FE-TEM [4].

## 2.4 Limit of Thickness in Observation by Transmission Electron Microscope

In order to observe the object with the good spatial resolution, with the accelerating voltage of  $O(100 \text{ kV})$  we have to slice specimens thin as  $O(10 \text{ nm})$ . The allowed thickness is determined by the beam energy and the beam quality. The acceptable range of specimens' thickness can be extended as the accelerating energy of TEMs increases.

Here  $\Delta E_p$  is introduced as the most probable energy loss and can be calculated as

$$\Delta E_p = \frac{N_A e^4 Z x}{8\pi\epsilon_0^2 A m_e c^2 \beta^2} \left[ \ln \left( \frac{N_A e^4 Z x}{8\pi\epsilon_0^2 I^2 A (1 - \beta^2)} \right) - \beta^2 + 0.198 \right], \quad (2.4.1)$$

and  $\Delta E_H$  is the FWHM of energy loss, written as

$$\Delta E_H = 4.02 \frac{N_A e^4 Z x}{8\pi\epsilon_0^2 A m_e c^2 \beta^2} \quad (2.4.2)$$

by Landau's theory[13]. The symbols appear in Eq.(2.4.1) and Eq.(2.4.2) are explained in Table 2.3. The spread of the energy loss by interacting with specimen can be approximated by  $\Delta E_H$ . The FWHM for the energy loss as a function of the kinetic energy  $T$  is displayed in Figure 2.3<sup>2</sup>. It can be seen that FWHM of the beam energy loss decreases as increasing energy and approaches to a constant value. Figure 2.4 shows the energy dispersion<sup>3</sup>. As described in Sec. 2.3, the defocus spread  $\Delta$  is determined by the energy dispersion  $\Delta T/T$ , not the energy spread  $\Delta T$ . As the result, the higher accelerating energy can improve the spatial resolution. This can be understood by following the steps below;

1. the higher accelerating energy can reduce the energy dispersion (Figure 2.4),
2. the lower energy dispersion makes the lower defocus spread (Eq. (2.3.8)),
3. the lower defocus spread decelerate the decay speed of  $E_{fs}$  (Eq. (2.3.5) and Figure 2.2),
4. the  $u_{\max}$  gets larger, then the spatial resolution is improved.

It is necessary to calculate actual defocus spread and LTF in order to acquire the spatial resolution in practice (Sec. 3.3.1).

---

<sup>2</sup>Here the notation of  $T$  is used instead of  $E$  for the beam energy.

<sup>3</sup>The definition of the energy spread for the phase contrast theory is chosen as the standard deviation in place of the FWHM, then now  $\Delta T_H$  is converted into  $\Delta T$  as  $\Delta T_H = \sqrt{2 \ln 2} \Delta T$ .

Table 2.3: The notation for Landau's theory [16].

Symbol	Definition	Value or Unit
$N_A$	Avogadro's number	$6.02214129(27) \times 10^{23} \text{ mol}^{-1}$
$r_e$	classical electron radius	$2.8179403267(27) \text{ fm}$
$m_e c^2$	electron mass	$0.510998928(11) \text{ MeV}$
$\rho$	material density	- g/cm <sup>3</sup>
$Z$	atomic number	no-unit
$A$	atomic mass	- g/mol
$\alpha$	fine structure constant	$1/137.035990074(44)$
$I$	mean excitation energy	- eV

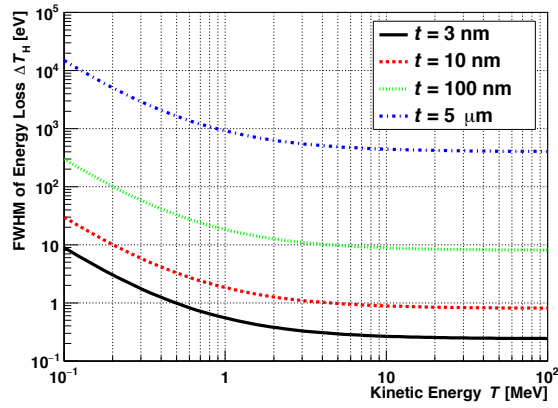


Figure 2.3: The variation of FWHM of the energy loss to the kinetic energy of the electron beam  $T$ . The thickness of the specimen  $t$  is chosen to 3 nm, 10 nm, 100 nm and 5  $\mu\text{m}$ .

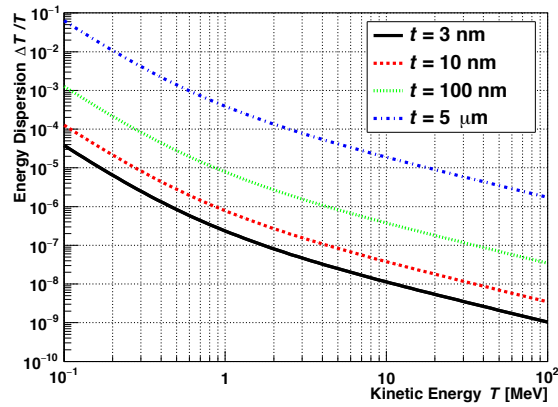


Figure 2.4: The variation of the energy dispersion to the kinetic energy of the electron beam  $T$ . The thickness of the specimen  $t$  is chosen of 3 nm, 10 nm, 100 nm and 5  $\mu\text{m}$ .

# Chapter 3

## Concept of Superconducting Radio Frequency Transmission Electron Microscope

In this chapter, the configuration and the key technologies of the SRF-TEM are described in detail. Next, the advantages provided by the SRF-TEM are introduced.

### 3.1 System Configuration of Superconducting Radio Frequency Transmission Electron Microscope

Figure 3.1 shows the overview of 300 kV SRF-TEM prototype. This is based on the conventional 300 kV TEM “H-9000 NAR” which was developed by Hitachi Cooperation. Because its accelerating voltage is the same as the prototype, the optical system can be reused. A newly developed 60 kV DC photocathode gun is introduced into the prototype instead of the thermal gun. The prototype has one two-mode cavity which can accelerate 60 keV-energy electrons emerging from the gun to 1.0 MeV, while the existing optics can receive electrons up to 300 keV. The Two-mode cavity is placed in a 4 K cryostat. In high energy accelerators SRF cavities are generally operated at 2.0 K to reduce the dissipating power. However this requires additional pumping system in order to cool 4 K liquid helium to 2K. Therefore the first SRF-TEM prototype employs the higher temperature drive (4 K). There is a buffer for liquid helium assuming that the circulation system for liquid He is not equipped in 300 keV SRF-TEM prototype. There is a differential pumping chamber because there is a difference of the required vacuum level between the conventional optical system and the photocathode electron gun. The required vacuum level for the optical system is  $O(10^{-5})$  Pa, while that for the photocathode electron gun is better than  $O(10^{-8})$  Pa.

In the following sub-sections, each element will be explained in detail.

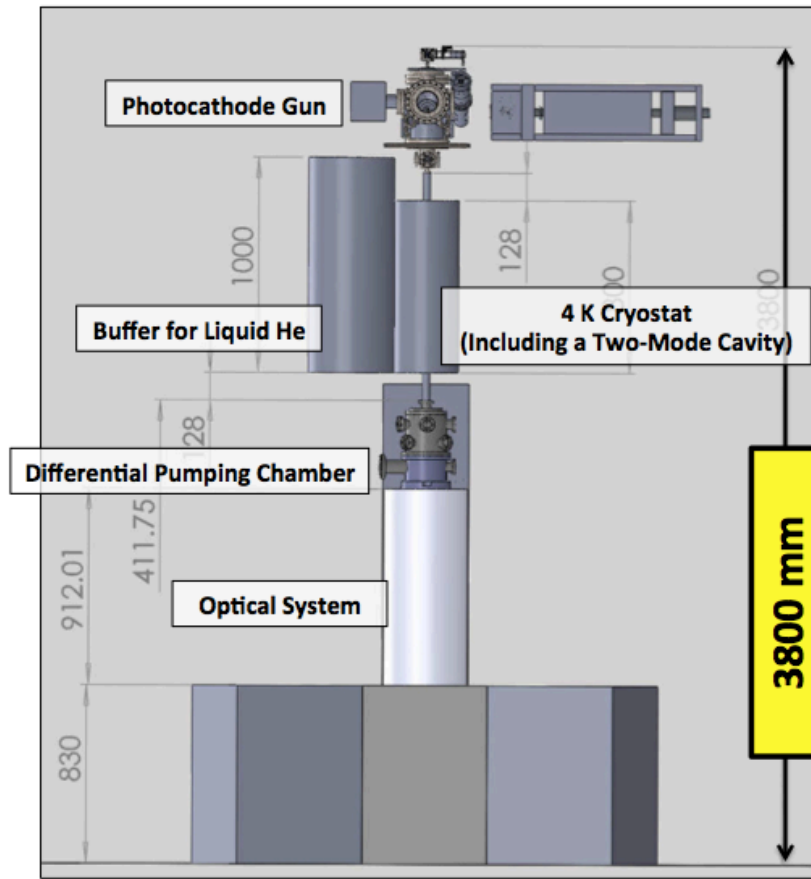


Figure 3.1: The overview of 300 kV SRF-TEM prototype.

### 3.1.1 Two-mode Cavity

The two-Mode cavity is one of the most important key technologies for SRF-TEM. A detailed explanation is given in Chapter 5. A brief description is given below.

A two-mode cavity has two resonant modes; the  $TM_{010}$  mode and the  $TM_{020}$  mode whose resonant frequencies are 1.3 GHz and 2.6 GHz respectively. Two mode cavity is designed so that the ratio of resonant frequencies is exactly 2.0000 in order to acquire flatter accelerating gradients in 100 % duty. Figure 3.2 shows the schematic overview of two-mode cavity. Two-mode cavity is made of niobium, the superconducting material which is widely utilized for accelerating cavities. Figure 3.3 displays the distributions of each resonant electric field calculated by the 3D electromagnetic fields simulation software “HFSS” .

As will be explained in Chapter 5, the excited resonant fields gets lower when the gap is occurred between the input RF frequency and the resonant frequency. This situation is called

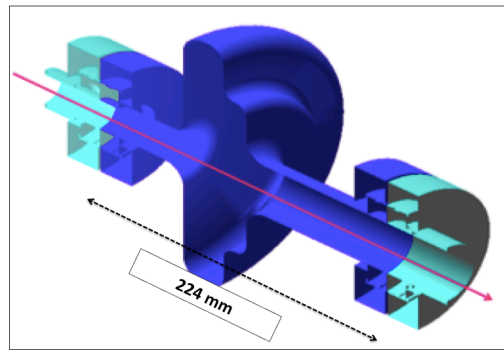


Figure 3.2: The schematic overview of the two-mode cavity. The red arrow represents the direction of the incoming electron.

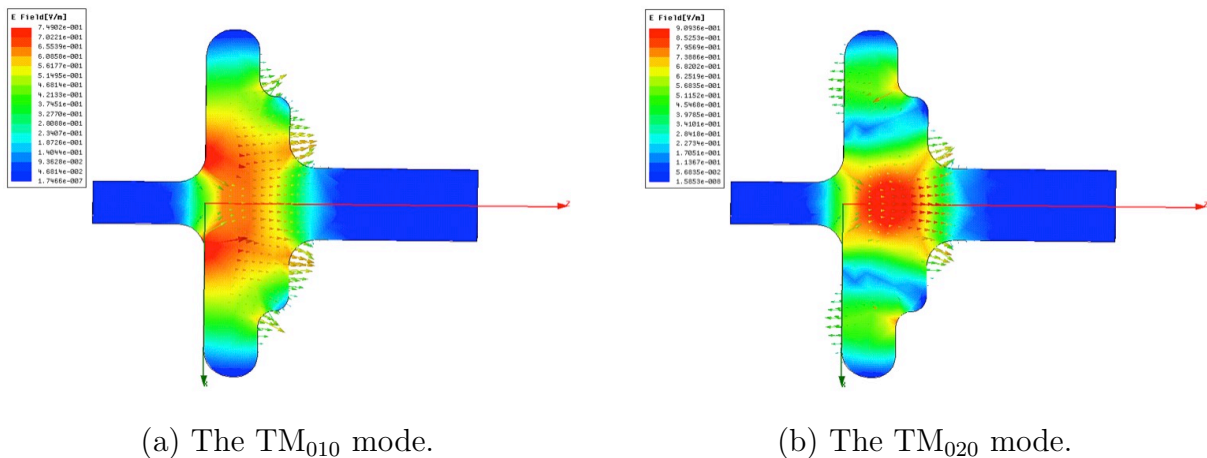


Figure 3.3: The distribution of each resonant electric field of the two-mode cavity. The red parts indicates the stronger electric field than blue ones.

detuned. Therefore two-mode cavity has two frequency tuner. One is “span tuner” and the other is “piezo tuner”. Figure 3.4 shows the placements of tuners. Figure 3.5 indicates how sensitive the resonant frequency when mechanically deformed at each position. Combining these tuners, deviated resonant frequency is pulled back to the input RF frequency.

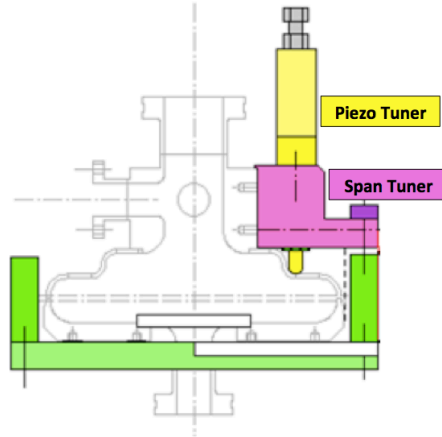


Figure 3.4: The span tuners and the piezo tuners equipped with the two-mode cavity. In this figure, only one set of tuners is depicted, however a two-mode cavity has two sets located symmetrically.

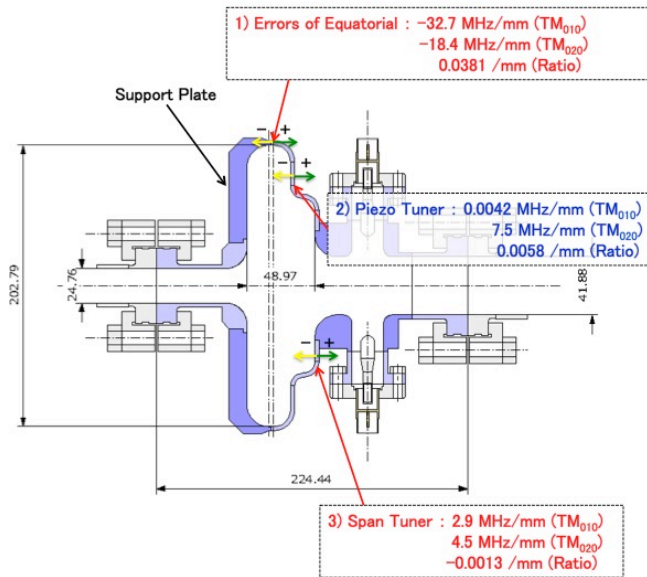


Figure 3.5: The sensitiveness of the resonant frequency for the tuning.

### 3.1.2 Photocathode Electron Gun

The SRF-TEM employs a photocathode electron gun instead of the thermal gun already installed in 300 kV H-9000 NAR. The photocathode gun adopts the mechanism that the coherent light emitted from lasers irradiates cathodes, and electrons that gain energy by photoelectric effect are extracted. This employs a transmission-type so that the diameter of the beam at the cathode can be minimized to place lenses behind the cathode. This transmission-type photocathode gun has been already utilized for a TEM[9].

Our gun accelerates electrons with the energy of 60 kV using DC acceleration scheme. Figure 3.6 is the overview of the entire of the gun. It is mainly composed of two chambers; one is the main chamber in which the cathode is installed and electrons are accelerated and the other is for cathode preparation.

The cathode is GaAs-GaAsP strained superlattice on a GaP substrate. This was originally developed for a high spin-polarized electron source of high energy accelerators and achieved the polarization of 90 %. Using this, the development of a spin-polarized TEM has been promoted[9]. Needless to say, SRF-TEM has this option.

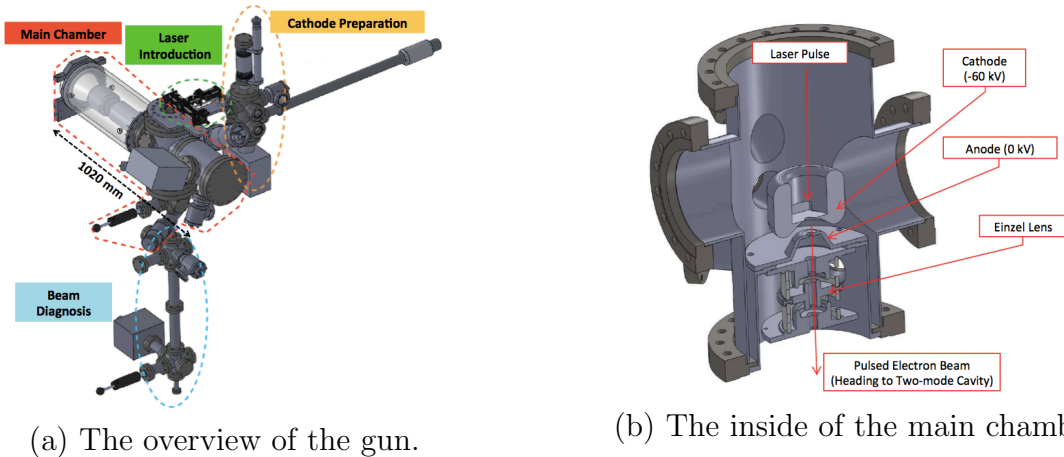


Figure 3.6: The 3D CAD of our photocathode gun.

### 3.1.3 RF Feedback System for Two-mode Cavity

The SRF-TEM has to control 4 parameters in one two-mode cavity; each amplitude and phase of the  $TM_{010}$  mode and the  $TM_{020}$  mode. As will be considered in Chapter 4, if there are some fluctuations of these parameters, the net accelerating field is deviated from the ideal, designed one (Figure 3.7). As mentioned above, two-mode cavity has two tuners to control the resonant frequency to deform its shape, though the speed of the operation of tuners are very slow. In SRF-TEM, the span tuner is considered to be fixed or operated in  $O(1 \text{ Hz})$  by a motor. Piezo tuner can be controlled electrically, then the operation speed is from DC to 200 Hz. The RF feedback system is a complementary tools to stabilize the resonant electric field

not to change the resonant frequency but adjust the amplitude and phase of the input power to maintain the resonant fields stable. The detailed explanation will be done in Chapter 6.

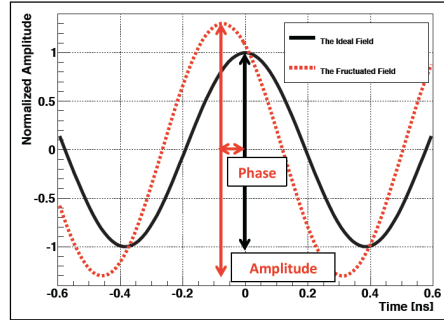


Figure 3.7: A conceptual situation of a deviated field.

### 3.2 Configuration Comparison between Conventional Transmission Electron Microscope and Superconducting Radio Frequency Transmission Electron Microscope

Here the new superconducting radio frequency transmission electron microscope (SRF-TEM) is compared with conventional TEMs. Table 3.1 compares their specifications and performances. Performance values of SRF-TEM mean the targets of the development. With 300 kV SRF-TEM prototype, the establishment of the two-mode cavity and the RF feedback system in order to satisfy the requirement of the energy spread  $\Delta T_{\text{mac}}$  on Table 3.1 is the goal.

Table 3.1: A comparison of the specifications and performances.  $\Delta T_{\text{mac}}$  indicates the energy spread which is determined by only of the machine, not including the interaction with the specimen.

	H-9000 NAR	300 kV SRF-TEM	3 MV SRF-TEM
Type of Gun	Thermal	Photocathode	Photocathode
Cathode	LaB <sub>6</sub>	GaAs-GaAsP	GaAs-GaAsP
Frequency of Beam	DC	1.3 GHz	1.3 GHz
$\Delta T_{\text{mac}}$	1 eV	10 eV	30 eV

### 3.3 Advantage of Superconducting Radio Frequency Transmission Electron Microscope

Here the advantages of Superconducting Radio Frequency Transmission Electron Microscope (SRF-TEM) are explained. These advantages are three;

1. the ability to observe thicker specimen
2. the downsizing of TEM facilities
3. the acquisition of the time resolution

All advantages owes to the features mentioned in the previous section. The detailed explanations are given in the following.

#### 3.3.1 Ability to Observe Thicker Specimen

As mentioned in Chapter 1, the most powerful advantage of the SRF-TEM is the ability of observing specimens thicker than ever. Here, one example is given to illustrate how SRF-TEM can improve this ability compared with Hitachi 1.2 MV FE-TEM.

Figure 3.8 shows the Lens Transfer Function (LTF) arranged to maximize the defocus spread  $\Delta$  keeping the spatial resolution 100 pm using the values achieved in Hitachi 1.2 MV FE-TEM. Each parameter values used in order to calculate the LTF functions in Figure 3.8 are listed in Table 3.2[4]. Here  $\Delta = 9.0$  nm.  $\Delta$  was already defined as

$$\Delta = C_c \sqrt{\left(\frac{\Delta T}{T}\right)^2 + \left(2\frac{\Delta J}{J}\right)^2}, \quad (3.3.1)$$

however this has to be modified by adding the energy spread occurred due to scattering at the specimen as

$$\Delta' = C_c \sqrt{\left(\frac{\Delta T_{\text{ini}}}{T}\right)^2 + \left(\frac{\Delta T_{\text{spe}}}{T}\right)^2 + \left(2\frac{\Delta J}{J}\right)^2} \quad (3.3.2)$$

where  $\Delta T_{\text{ini}}$  is the energy spread generated at the cathode of the gun and the electrostatic acceleration part and is as small as 0.3 ppm, and  $\Delta T_{\text{spe}}$  is the energy spread occurred at

Table 3.2: Parameters of Hitachi 1.2 MV FE-TEM[4].

$C_3$ : Coefficient of the third spherical aberration	$-23 \mu\text{m}$
$C_5$ : Coefficient of the fifth spherical aberration	29 mm
$\sigma(x)$ : Image spread	10 pm
$\beta$ : Illumination tilt spread	0.05 mdeg.

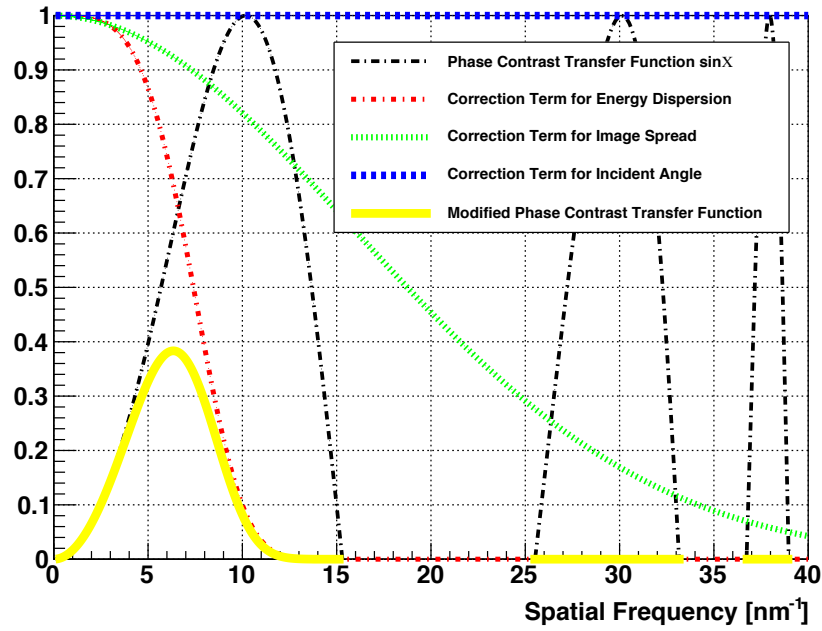


Figure 3.8: The lens transfer function for Hitachi 1.2 MV FE-TEM. This is the case of the maximum defocus spread  $\Delta$  with the spatial resolution of 100 pm.

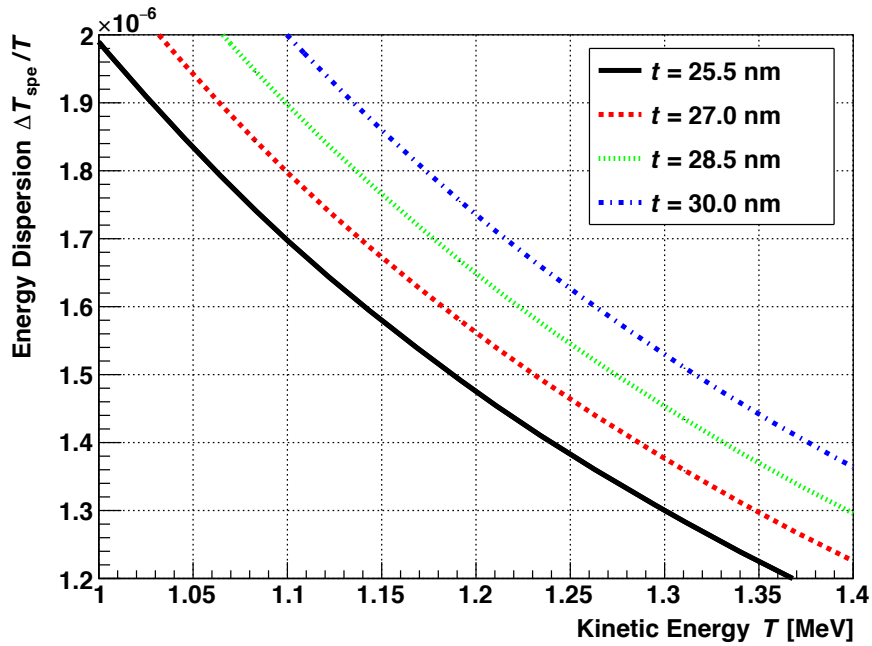


Figure 3.9: The energy dispersion for an Al specimen magnifying the energy range of 1.2 MeV.

the specimen due to scattering. The first and the last terms are determined by the machine performance, and the second depends on the specimen's material, thickness and density.  $\Delta T_{\text{spe}}/T$  can be written using Equations (3.3.1) and (3.3.2) as

$$\frac{\Delta T_{\text{spe}}}{T} = \frac{1}{C_c} \sqrt{\Delta'^2 - \Delta^2}. \quad (3.3.3)$$

[4] reveals  $\Delta = 1.1$  nm when the spatial resolution is recorded as 43 pm. If a degradation of the spatial resolution is allowed up to 100 pm, the maximum values of  $\Delta$  is 9.0 nm which becomes a new  $\Delta'$ . Then  $\Delta T_{\text{spe}}/T$  is calculated as  $\Delta T_{\text{spe}}/T = 1.65 \times 10^{-6}$  using Eq. (3.3.3). Figure 3.9 shows the energy dispersion in the case of that the specimen is Al. Reading this, for the beam energy of 1.2 MeV, the allowed thickness is about 28.5 nm.

Next the future 10 MV SRF-TEM will be considered. Figure 3.10 shows its LTF using parameters in Table 3.2 and the  $\Delta = 55$  nm maximized under the situation that the spatial resolution is 100 pm. For SRF-TEM, the defocus spread has to be modified again due to the energy spread for RF acceleration. Eq. (3.3.2) is modified as

$$\Delta'' = C_c \sqrt{\left(\frac{\Delta T_{\text{ini}}}{T}\right)^2 + \left(\frac{\Delta T_{\text{RF}}}{T}\right)^2 + \left(\frac{\Delta T_{\text{spe}}}{T}\right)^2 + \left(2\frac{\Delta J}{J}\right)^2} \quad (3.3.4)$$

where  $\Delta T_{\text{RF}}$  is the energy spread generated in the RF acceleration. Using Eq. (3.3.1),

$$\frac{\Delta T_{\text{spe}}}{T} = \frac{1}{C_c} \sqrt{\Delta''^2 - \Delta^2 - \left(C_c \frac{\Delta T_{\text{RF}}}{T}\right)^2}. \quad (3.3.5)$$

Here the value of  $\Delta T_{\text{RF}}$  is assumed as 30 eV<sup>1</sup>. Then the maximum  $\Delta T_{\text{spe}}/T$  to allow the observation with the spatial resolution of 100 pm becomes  $9.7 \times 10^{-6}$ . Figure 3.11 shows the energy dispersion for Al specimen, magnifying the range of  $T = 10$  MeV. With Figure 3.11, the maximum thickness to achieve spatial resolution of 100 pm is 2.6  $\mu\text{m}$  for 10 MV SRF-TEM.

Summarizing these considerations, 10 MV SRF-TEM has the ability to observe about 100 times thicker specimens with 100 pm spatial resolution compared with the state-of-the-art Hitachi 1.2 MV FE-TEM. More precise calculations needs simulations to consider each specimen's configuration.

Looking at this advantage of observing thicker specimens from another perspective, when observing specimens of the same thickness, SRF-TEM can achieve better spatial resolution. As described above, the spatial resolution of 100 pm is sustained when the Al specimen's thickness is 28.5 nm with Hitachi 1.2 MV FE-TEM. Figure 3.12 shows the energy dispersion from  $T = 1$  MeV to 10 MeV with 28.5 nm-thick Al specimen. It can be seen that the energy dispersion is  $1.0 \times 10^{-7}$  when kinetic energy  $T = 10$  MeV. Therefore it leads to  $\Delta'' = 16.3$  nm using Eq. (3.3.4). Substituting this into the LTF equations, Figure 3.13 is acquired. This spatial resolution is derived as 60 pm. This is because the phase contrast transfer function  $\sin\chi_{\text{ps}}$  decreases owing to the shortening of the de Broglie wave length.

---

<sup>1</sup>Later it will be discussed whether this value is proper.

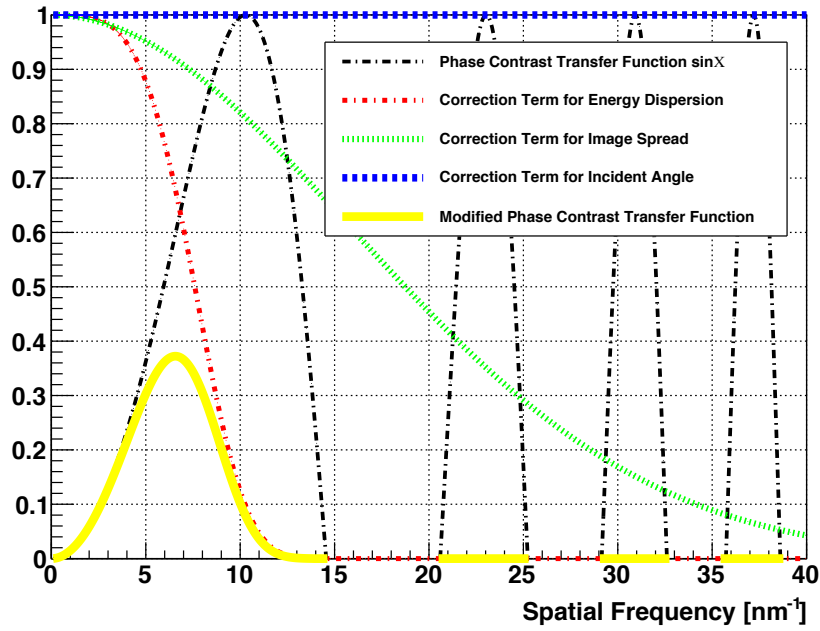


Figure 3.10: The lens transfer function for the future 10 MV SRF-TEM. This is the case of maximizing the defocus spread  $\Delta$  with the spatial resolution of 100 pm.

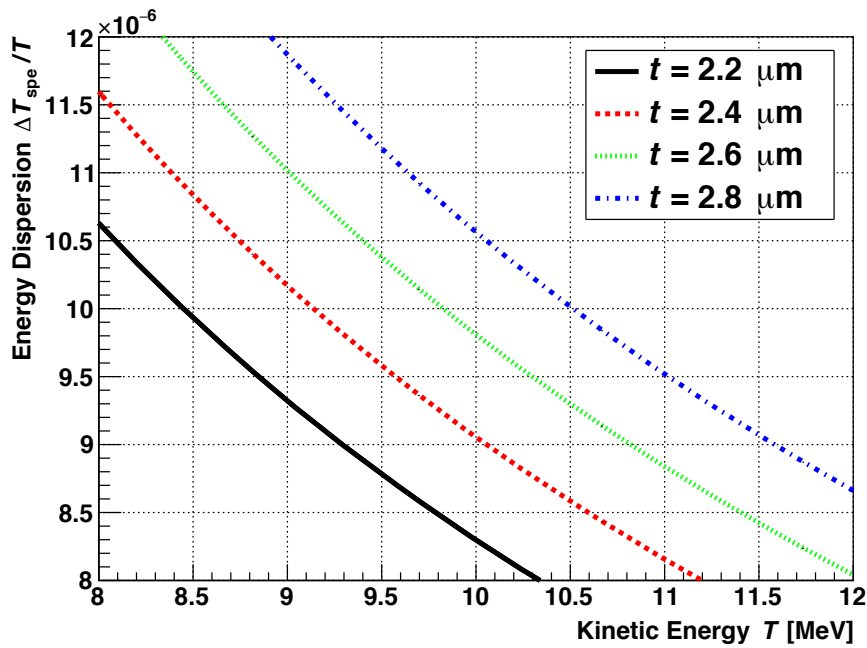


Figure 3.11: The energy dispersion for an Al specimen magnifying the energy range of 10 MeV.

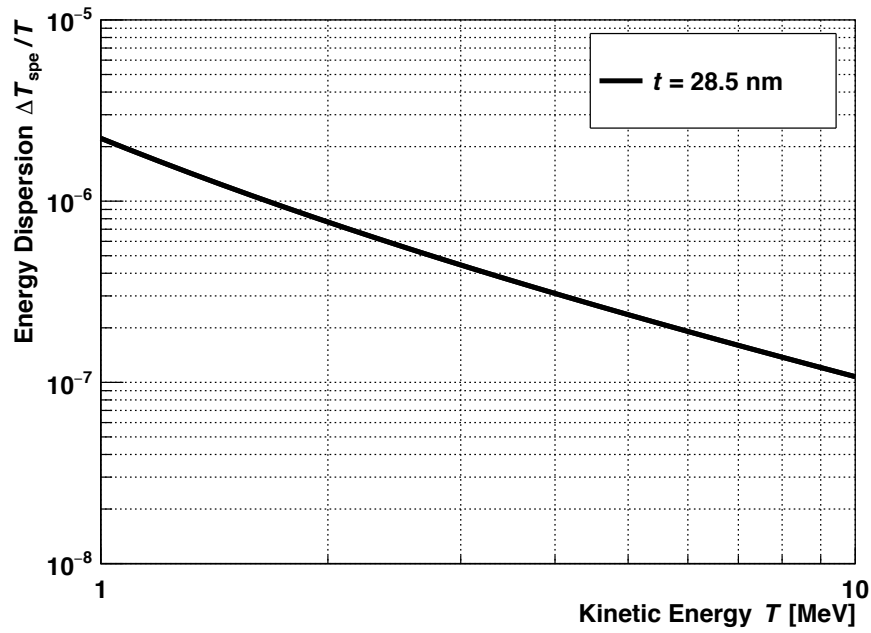


Figure 3.12: The energy dispersion for a 28.5 nm-thick Al specimen.

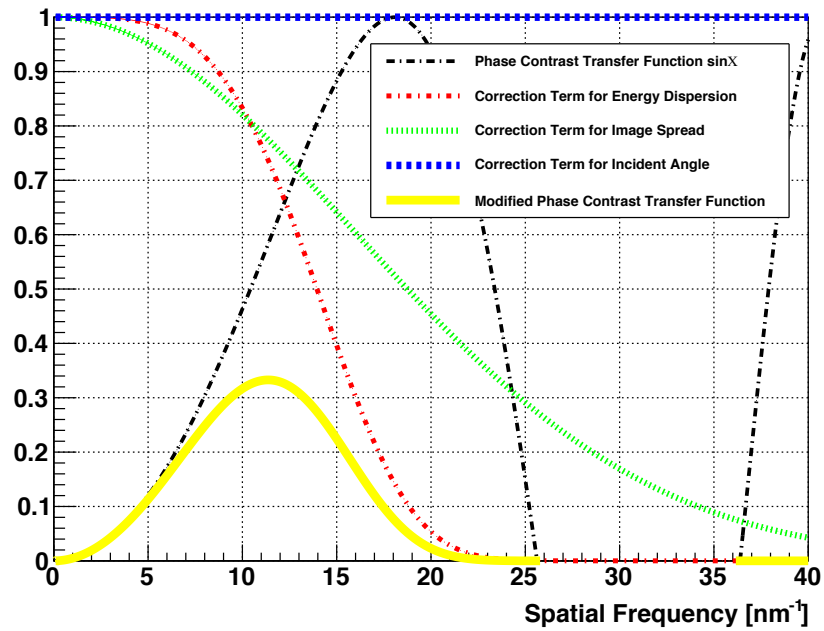


Figure 3.13: The lens transfer function for 10 MV SRF-TEM with a 28.5 nm-thick Al specimen in the case of  $\Delta'' = 16.3$  nm and  $\Delta f = 13$  nm. The spatial resolution is 60 pm.

### 3.3.2 Downsizing Facility

RF resonant cavities can generate much higher accelerating gradient so that the TEM facilities can be compact. For example, 1.2 MV FE-TEM of Hitachi is tall as about 10 m[6]. In our SRF-TEM, only one two-mode cavity is needed to accelerate electrons to 1.0 MV even when applying two-mode acceleration<sup>2</sup>. In this case, the entire system is designed as Figure 3.1 and its height is about 4 m. This scale is comparable with a few hundred of keV acceleration voltage TEMs which are the most common type. However, our SRF-TEM needs a helium circulation system including a liquefaction facility and a helium gas collection line. General laboratories has its own helium facility. When the SRF-TEM is installed, it is necessary to construct new gas collection lines connected to the existing helium facility.

### 3.3.3 Acquisition of Time Resolution

Conventional TEMs use DC electron beams with thermal guns or cold field emission guns. Therefore it is difficult to observe specimens with time resolution. In contrast, SRF-TEM employs a photocathode gun which supplies the electron bunches in synchronization with the period of the two-mode cavity's acceleration; 1.3 GHz. This allows SRF-TEM to observe specimens with time resolution. Figure 3.14 shows the density distribution of electrons at the cathode, calculated based on the thermal diffusion model[17]. The optimized bunch charge is 0.1 fC which corresponds to 640 electrons for our SRF-TEM. In order to acquire one TEM image, about  $10^7$  electrons are needed[18]<sup>3</sup>. This indicates that about 15600 bunches are needed for one image for our SRF-TEM. If bunches are supplied with 1.3 GHz (this situation is called 100 % duty), SRF-TEM has the time resolution of 12  $\mu$ s.

There is another observation scheme with time resolution; pumping probe method. This utilizes both exciting light pulse (pumping) and imaging electrons (probe). This type of

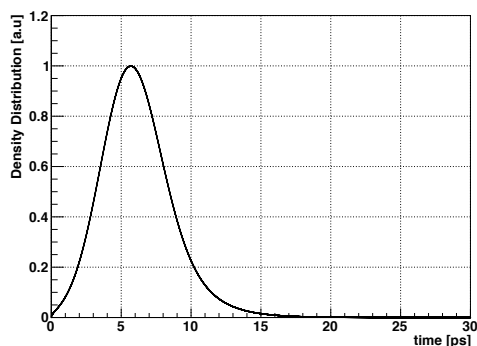


Figure 3.14: The density distribution of electrons at the cathode.

---

<sup>2</sup>Two-mode acceleration utilizes both of accelerations and decelerations with two resonant modes. This means if the first priority to minimize the energy spread was abandoned, higher gradients can be acquired and this enables the downsizing the facility.

<sup>3</sup>Strictly speaking, it depends on the brightness of the beam and the number of the pixel of CCD sensors.

TEMs are called dynamic transmission electron microscopes (DTEMs). The transition of the specimen is reconstructed virtually<sup>4</sup> to change the phase difference between the pumping light and probing electrons. Time resolution  $\tau$  is estimated as

$$\tau = \sqrt{\tau_{\text{pum}}^2 + \tau_{\text{pro}}^2 + \tau_{\text{jit}}^2}, \quad (3.3.6)$$

where  $\tau_{\text{pum}}$  represents the time width of the pumping laser,  $\tau_{\text{pro}}$  represents the time width of the imaging electron bunch and  $\tau_{\text{jit}}$  represents the jitter of the phase between pumping lights and imaging electron bunches.  $\tau_{\text{pum}}$  and  $\tau_{\text{jit}}$  can be suppressed to 100 fs.  $\tau_{\text{pro}}$  is 2 ps for our SRF-TEM (see Figure 3.14). In this way, our SRF-TEM is able to acquire 2 ps time resolution using the pumping probe method. It is noted that when pumping probe method is employed, one electron bunch has to generate one image. This increase the bunch charge which leads to additional energy dispersion.

---

<sup>4</sup>It is noted that the pumping probe method cannot record one picked process with many temporal slices. It records one image in one process. Therefore this method can be applied only for repeatable phenomena and it just reconstructs the transition.



## Chapter 4

# System Design of Superconducting Radio Frequency Transmission Electron Microscope with 300 kV and 3 MV by Numerical Simulation of Beam Dynamics

This chapter shows how effectively the two-mode acceleration realized by the two-mode cavity can restrain the energy spread for 300 kV and 3 MV acceleration. In order to achieve this goal, the numerical simulation program, called General Particle Tracer (GPT) is utilized[19]. This employs the fifth order Runge-Kutta solver which is capable of calculating 3D beam dynamics to trace the trajectory of each charged particle. It can account for space charge effect (not considered in this thesis).

### 4.1 Scheme of Simulation Study Using General Particle Tracer

In this section, a brief explanation concerning GPT is given, and this is the summary quoted from GPT manual[19]. And, the explanation of modified Powell method is based on [20].

### 4.1.1 Scheme of Numerical Simulation

This part explains the method of the numerical simulation adopted by GPT. GPT calculates the dynamics of charged particles based on the relativistic equation of motion,

$$\frac{d\mathbf{P}_i}{dt} = \mathbf{F}_i \quad (4.1.1)$$

$$\frac{d\mathbf{x}_i}{dt} = \mathbf{v}_i = \frac{\mathbf{p}_i c}{\sqrt{\mathbf{p}_i^2 c^2 + m_i^2 c^2}} \quad (4.1.2)$$

where  $\mathbf{P}_i$  is the relativistic momentum of the  $i$ -th particle,  $\mathbf{F}_i$  is the power applied on the  $i$ th particle,  $\mathbf{x}_i$  is the coordinate of the  $i$ -th particle,  $\mathbf{v}_i$  is the velocity of the  $i$ th particle,  $m_i$  is the mass of the  $i$ th particle and  $c$  is the speed of light.  $\mathbf{F}_i$  is given by

$$\mathbf{F}_i = q(\mathbf{E}_i + \mathbf{v}_i \times \mathbf{B}_i) \quad (4.1.3)$$

where  $\mathbf{E}_i$  and  $\mathbf{B}_i$  are the electric and magnetic field applied on the  $i$ th particle respectively and  $q$  is the particle charge.

GPT can consider the space charge effect which is the mutual repulsion effect of charged particles inside the beam bunch. Including this effect, Eq. (4.1.1), (4.1.2) and (4.1.3) are summarized as

$$\frac{d\mathbf{y}(t)}{dt} = \mathbf{f}(t, \mathbf{y}(t)) \quad (4.1.4)$$

where  $\mathbf{y}(t)$  is  $(N \times 6)$ -dimensional vector of all particles coordinates and momentums.

GPT employs the fifth order embedded Runge-Kutta method in order to calculate Eq.(4.1.4). This can automatically optimize the next step size  $h$  to consider whether the current step size is adequate in each step. Each step is calculated as

$$\begin{aligned} k_1 &= hf(x_n, y_n) \\ k_2 &= hf(x_n + a_2h, y_n + b_{21}k_1) \\ &\dots \\ k_6 &= hf(x_n + a_6h, y_n + b_{61}k_1 + \dots + b_{65}k_5) \\ y_{n+1} &= y_n + c_1k_1 + \dots + c_6k_6 + O(h^6). \end{aligned} \quad (4.1.5)$$

The coefficients of  $a_i$ ,  $b_i$  and  $c_i$  are given in Table 4.1. On the other hand, by replacing  $c_i^*$  with  $c_i$ , Eq. (4.1.5) becomes 4th-order Runge-Kutta equation,

$$y_{n+1}^* = y_n + c_1^*k_1 + \dots + c_6^*k_6 + O(h^5). \quad (4.1.6)$$

Embedded Runge-Kutta method can always modify the step size to decide whether the current step size is appropriate by calculating the difference between two answers  $y_{n+1}$  and  $y_{n+1}^*$  as

$$\Delta = y_{n+1} - y_{n+1}^* = \sum_{i=1}^6 (c_i - c_i^*)k_i \quad (4.1.7)$$

Table 4.1: Coefficients of embedded Runge-Kutta method utilized in General Particle Tracer.

$i$	$a_i$	$b_{ij}$					$c_i$	$c_i^*$
1							37/378	2825/27648
2	1/5	1/5					0	0
3	3/10	3/40	9/40				250/621	18575/48384
4	3/5	3/10	-9/10	6/5			125/594	13525/55296
5	1	-11/54	5/2	-70/27	35/27		0	277/14336
6	7/8	1631/55296	175/512	575/13824	44275/110592	253/2096	512/1771	1/4
$j =$		1	2	3	4	5		

where  $\Delta$  is the sum of every sixth vector of all particles. Naming  $\gamma\beta$  and  $x$  of the particle that has the maximum  $\Delta$  with  $(\gamma\beta)_{\max}$  and  $x_{\max}$  respectively, then a new parameter of  $\Lambda$  is defined as

$$\Lambda = \max \left( \frac{(\gamma\beta)_{\max}}{(\gamma\beta)_{\text{err}}}, \frac{x_{\max}}{x_{\text{err}}} \right), \quad (4.1.8)$$

This is used in order to evaluate the adequacy of the current step size. Here  $(\gamma\beta)_{\text{err}}$  and  $x_{\text{err}}$  are the reference values and  $(\gamma\beta)_{\text{err}} = 1.0 \times 10^{-4}$  and  $x_{\text{err}} = 1.0 \times 10^{-4}$  unless specified in the GPT program. In each step, the calculation of  $\Lambda$  is done. In the case that  $\Lambda > 1$ , the new step size  $h$  is suggested as

$$h_{\text{new}} = \begin{cases} S\Lambda^{1/4}h_{\text{old}} & (S\Lambda^{1/4} > 0.10) \\ 0.10h_{\text{old}} & (\text{otherwise}) \end{cases}$$

and in the case that  $\Lambda \leq 1$ , the new step size  $h$  is suggested as

$$h_{\text{new}} = \begin{cases} S\Lambda^{1/5}h_{\text{old}} & (S\Lambda^{1/5} < 5.0) \\ 5h_{\text{old}} & (\text{otherwise}) \end{cases}$$

where  $S = 0.85$  unless specified in the GPT program.

As explained above, GPT can minimize the consuming time required for calculation to maintain the accuracy that users set. However this automation of the step size is done by comparing the fifth-order accuracy with forth-order one, which means that users have to set the step size anew when calculating the dynamics in the high gradient fields.

### 4.1.2 Scheme of Design Optimization

GPT has the optimization scheme to minimize or maximize the specified variable. The scheme employed by GPT is the modified Powell method[20]. The second-order Taylor expansion of

the function  $f(\mathbf{x})$  that has  $N$  variables is

$$\begin{aligned} f(\mathbf{x}) &= f(\mathbf{x}_0) + \sum_i \left. \frac{\partial f}{\partial x_i} \right|_{\mathbf{x}=\mathbf{x}_0} (x_i - x_{i0}) + \frac{1}{2} \sum_{i,j} \left. \frac{\partial^2 f}{\partial x_i \partial x_j} \right|_{\mathbf{x}=\mathbf{x}_0} (x_i - x_{i0})(x_j - x_{j0}) + \dots \\ &\approx c - \mathbf{b} \cdot (\mathbf{x} - \mathbf{x}_0) + \frac{1}{2} (\mathbf{x} - \mathbf{x}_0) \cdot \mathbf{A} \cdot (\mathbf{x} - \mathbf{x}_0) \end{aligned} \quad (4.1.9)$$

where

$$c \equiv f(\mathbf{x}_0) \quad (4.1.10)$$

$$\mathbf{b} \equiv -\nabla f|_{\mathbf{x}=\mathbf{x}_0} \quad (4.1.11)$$

$$[\mathbf{A}]_{ij} \equiv \left. \frac{\partial^2 f}{\partial x_i \partial x_j} \right|_{\mathbf{x}=\mathbf{x}_0}. \quad (4.1.12)$$

$\mathbf{A}$  is called Hessian matrix and is a symmetric square matrix if  $f(\mathbf{x})$  is continuous for every variable. Take gradient of Eq. (4.1.10),

$$\nabla f = \mathbf{A} \cdot (\mathbf{x} - \mathbf{x}_0) - \mathbf{b} \quad (4.1.13)$$

is given, then

$$\delta(\nabla f) = \mathbf{A} \cdot \delta\mathbf{x}. \quad (4.1.14)$$

If the minimum point is found in a direction of  $\mathbf{u}$ , using  $\mathbf{u} \cdot \delta(f) = 0$ ,

$$\mathbf{u} \cdot \mathbf{A} \cdot \delta\mathbf{x} = 0 \quad (4.1.15)$$

is given. Based on this, the next direction to find the minimum is  $\delta\mathbf{x}$  that satisfies Eq. (4.1.15). These directions which are more than one are called conjugated direction.

Here, the process that finds the minimum point in the case of two variables is illustrated in practice (Figure 4.1).

1. Find the minimum point  $\mathbf{x}_1$  in the direction of  $\mathbf{u}_1$  from the initial point  $\mathbf{x}_0$ .
2. Find the minimum point  $\mathbf{x}_2$  in the direction of  $\mathbf{u}_2$  from the previous minimum point  $\mathbf{x}_1$ .
3. Set  $\mathbf{x}_2 - \mathbf{x}_0 = \mathbf{u}_2$  and  $\mathbf{u}_2 = \mathbf{u}_1$ , then find the new minimum point  $\mathbf{x}_0$ .

Repeating the process, the calculation is finished when the current minimum point is converged. The minimization of the one direction is conducted by successive parabolic interpolation method of golden section search method. It is necessary to set the appropriate initial values in order to minimize the variable correctly. Without this, the minimization is converged at a metastable point or the calculation diverges. To prevent from these problems, it is useful to sweep the variable and estimate the appropriate initial values to some extent. GPT has the function of MR where the variable can be swept, and using this, incorrect minimization can be avoided.

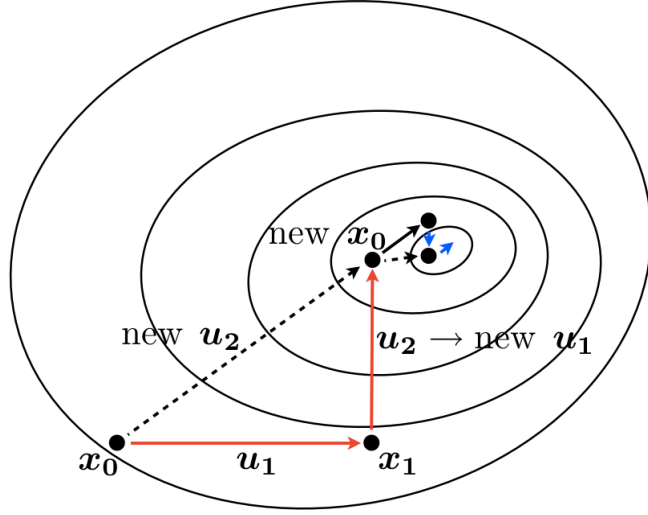


Figure 4.1: The concept of modified Powell method.

## 4.2 Comparison of Two-mode Acceleration and One-mode Acceleration

In this section, the capability of the two-mode acceleration in reducing the energy spread is confirmed by carrying out GPT simulations. The objective accelerating energy is 300 keV for the first SRF-TEM prototype and 3 MeV which is the same value as the world's highest energy of TEMs. For each accelerating energy, the energy spread  $\Delta T$  and the energy dispersion  $\Delta T/T$  is calculated in the both case of the one-mode acceleration which employs only the  $TM_{010}$  mode and the two-mode acceleration which employs both the  $TM_{010}$  mode and the  $TM_{020}$  mode.

### 4.2.1 Method of Optimization

For the one-mode acceleration, there are two variables to control in order to minimize the energy spread, ; the amplitude and the phase of the  $TM_{010}$  mode. For the two-mode acceleration, there are four variables to control; each amplitude and phase of the  $TM_{010}$  mode and the  $TM_{020}$  mode. It is difficult to find the minimum point in this optimization. In order to resolve this, I used the MR function which is equipped with GPT. This program sweeps the designated variables to observe the variation of the target value which is the energy spread  $\Delta T$  here. After obtaining the information around the minimum point, the optimization is carried out around the estimated point.

Figure 4.2 shows an example of the result of MR function. This is the one-mode acceleration employing only the  $TM_{010}$  mode and the goal accelerating energy is 300 keV. In this example, the designated variable to be swept is the phase of the  $TM_{010}$  mode, whereas the amplitude of the  $TM_{010}$  mode is fixed. The most probable point where the energy dispersion

converges to the minimum value is estimated to be about 28.6 degree (0.50 radian<sup>1</sup>). This is followed by optimization.

The example above is the easiest one. In the case of four free parameters, the basis of the optimization process is the same.

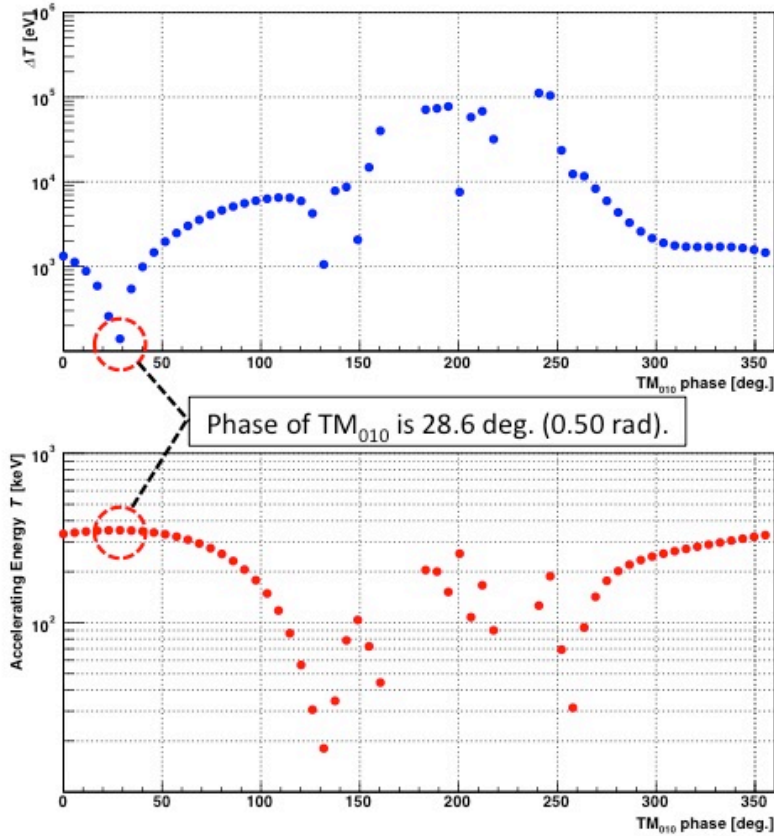
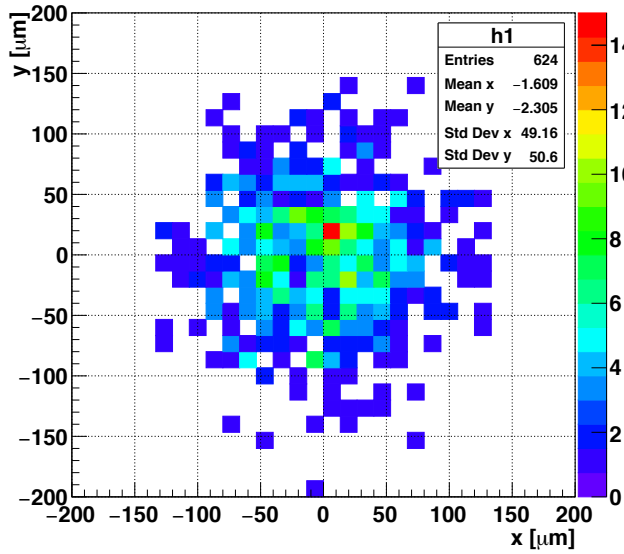


Figure 4.2: An example of MR function. Here the one-mode acceleration for 300 keV is the case. The accelerating field is fixed as 7.46 MV/m and the phase is swept, then the energy spread  $\Delta T$  and the accelerating energy  $T$  are recorded. The minimum point of the energy dispersion which corresponds to the maximum point of the accelerating energy is about 28.6 degree of the phase of the TM<sub>010</sub> mode.

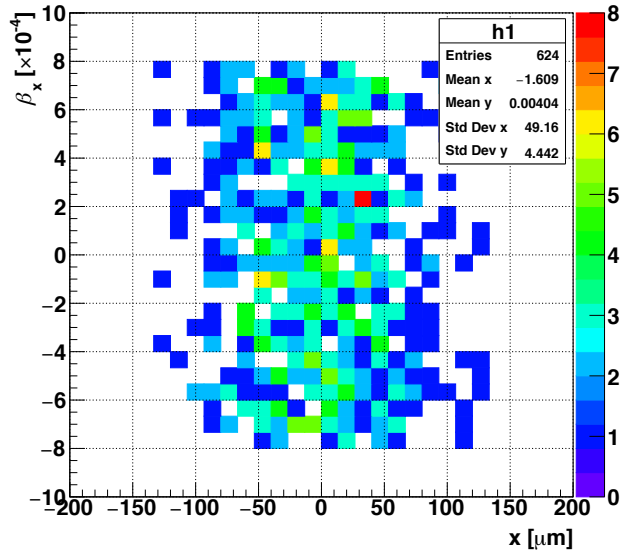
## 4.2.2 Condition of Beam Dynamics Simulation

In this sub-section, the conditions utilized to simulate the beam dynamics are explained. The initial condition is defined by the cathode and is common for all simulations. The initial parameters are summarized in Table 4.2. The initial distribution of electrons are depicted in Figure 4.3.

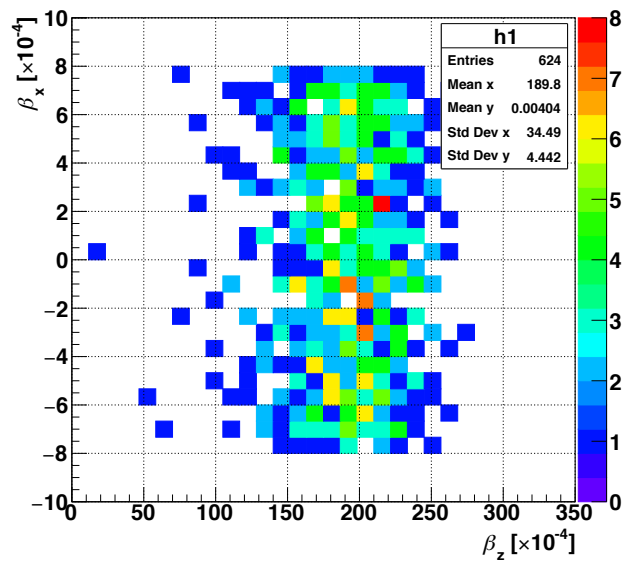
<sup>1</sup>GPT describes the phase in the unit of radian.



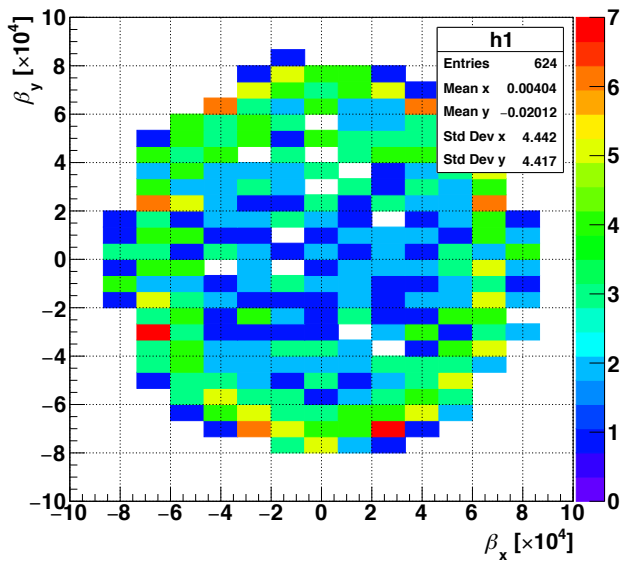
(a)  $x$  vs.  $y$ .



(b)  $x$  vs.  $\beta_x$ .



(c)  $\beta_z$  vs  $\beta_x$ .



(d)  $\beta_x$  vs  $\beta_y$ .

Figure 4.3: Electron Distribution at  $t = 2.0 \times 10^{-12}$ .

Table 4.2: The initial condition for GPT simulation.  $C$  represents the charge of one bunch,  $r_{\text{ini}}$  represents the initial radius on the cathode,  $f_{010}$  and  $f_{020}$  represent the resonant frequency of the  $\text{TM}_{010}$  mode and the  $\text{TM}_{020}$  mode respectively and  $\Delta E_{\text{ini}}$  represents the initial energy spread at the cathode.

$C$	-0.1 fC
$r_{\text{ini}}$	100 $\mu\text{m}$
$f_{010}$	1.3 GHz
$f_{020}$	2.6 GHz
$\Delta E_{\text{ini}}$	0.15 eV

The distribution of electric fields of 60 kV DC gun and the two-mode cavity are installed into GPT simulations. Those are calculated by the software Superfish. Figure 4.4 shows the distributions of the electric field for the two-mode cavity.

The geometry of the simulation is depicted in Figure 4.5. This is the case of 300 kV acceleration and the required number of the two-mode cavity is one. Figure 4.6 shows the geometry in the case of 3 MV acceleration and the number of the two-mode cavity is three. The spaces between each component are determined to reflect the actual size of components and the vacuum tools.

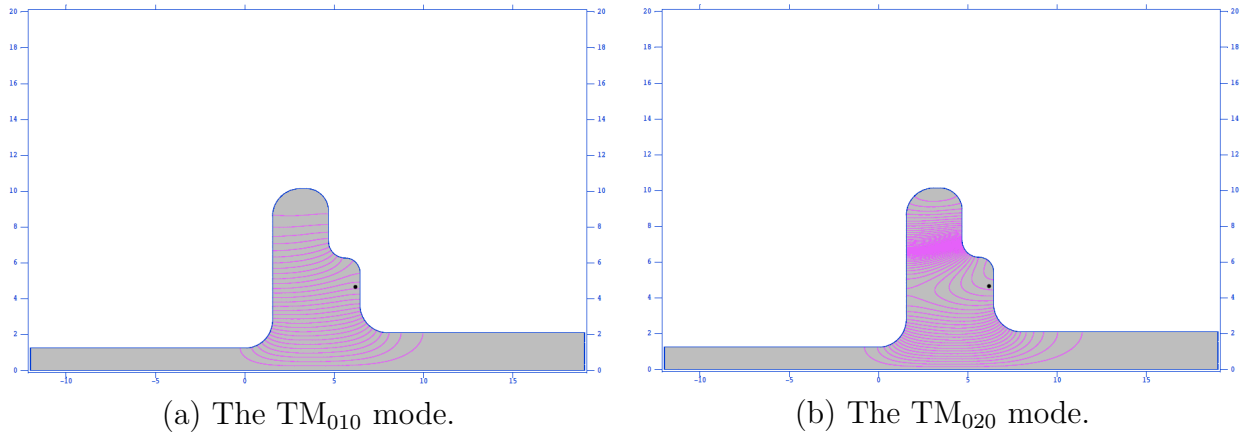


Figure 4.4: The distribution of the electric fields of the two-mode cavity.

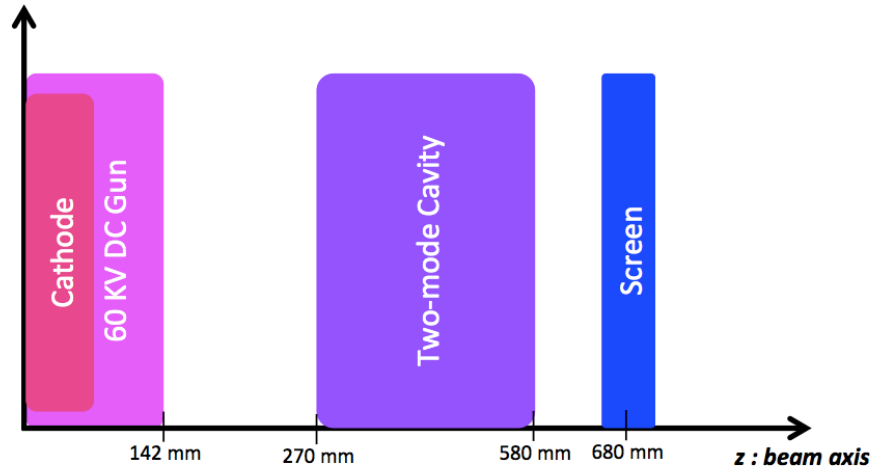


Figure 4.5: The geometry of the simulation for 300 kV.

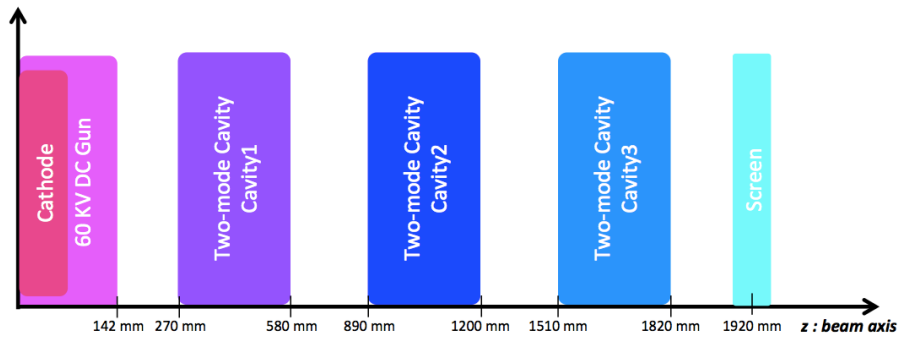


Figure 4.6: The geometry of the simulation for 3 MV.

### 4.2.3 Optimization Result of 300 keV Acceleration

Table 4.3 summarizes the simulation result for 300 keV acceleration. Owing to the two-mode acceleration, the energy dispersion  $\Delta T/T$  is reduced by a factor of twenty compared to the case of one-mode acceleration. Table 4.4 shows the optimal values in order to minimize the energy spread  $\Delta T$ . The electric field on the beam axis  $E_z$  in the two-mode cavity is built in the form of

$$E_z = E_{\text{ap}} \cos(\omega t + \theta) \quad (4.2.1)$$

in GPT simulations. Table 4.4 indicates the result for the amplitude  $E_{\text{ap}}$  and the phase  $\theta$ .  $\omega$  is  $2\pi \times 1.3$  GHz and  $2\pi \times 2.6$  GHz for the  $\text{TM}_{010}$  mode and the  $\text{TM}_{020}$  mode respectively.  $t$  indicates the elapsed time starting from the firing of the gun. The values of  $E_{\text{ap}}$  directly become the performance requirements for the practical two-mode cavities in order to manufacture the 300 kV SRF-TEM prototype.

Figure 4.7 - 4.8 show the variations of the accelerating energy  $T$  for the optimal one-mode acceleration and two-mode acceleration respectively.

Table 4.3: The simulation result of the 300 kV acceleration.

	$T$	$\Delta T$	$\Delta T/T$
One-mode Acceleration	330 keV	57.6 eV	$1.75 \times 10^{-4}$
Two-mode Acceleration	272 keV	2.19 eV	$7.91 \times 10^{-6}$

Table 4.4: The optimal vales of the accelerating modes for the 300 kV acceleration.

	Amplitude of $\text{TM}_{010}$	Phase of $\text{TM}_{010}$	Amplitude of $\text{TM}_{020}$	Phase of $\text{TM}_{020}$
One-mode	6.98 MV/m	0.456 rad.	-	-
Two-mode	7.46 MV/m	0.454 rad.	7.20 MV/m	0.500 rad.

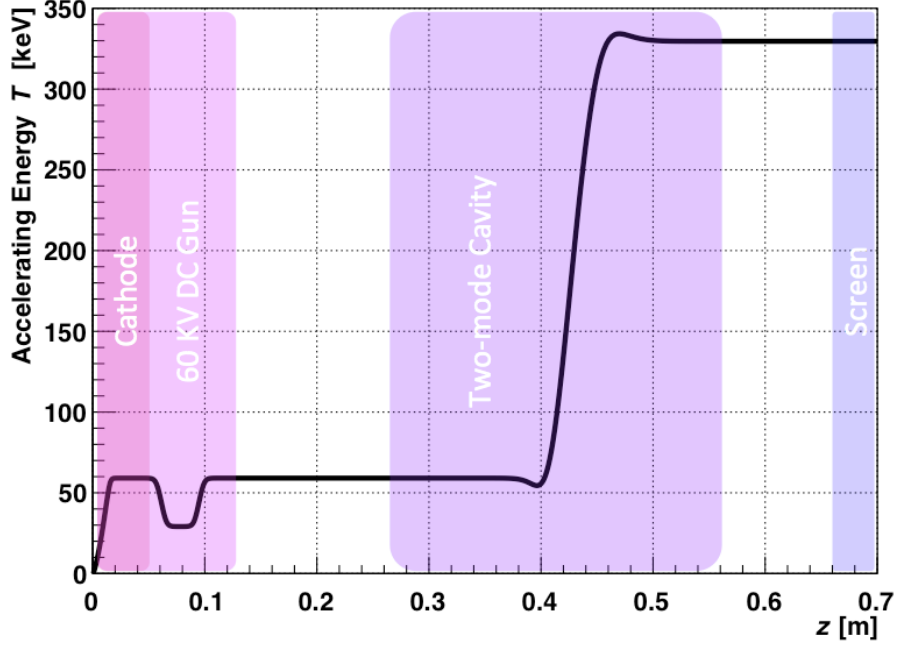


Figure 4.7: The variation of the accelerating energy  $T$  for the optimal 300 kV one-mode acceleration.

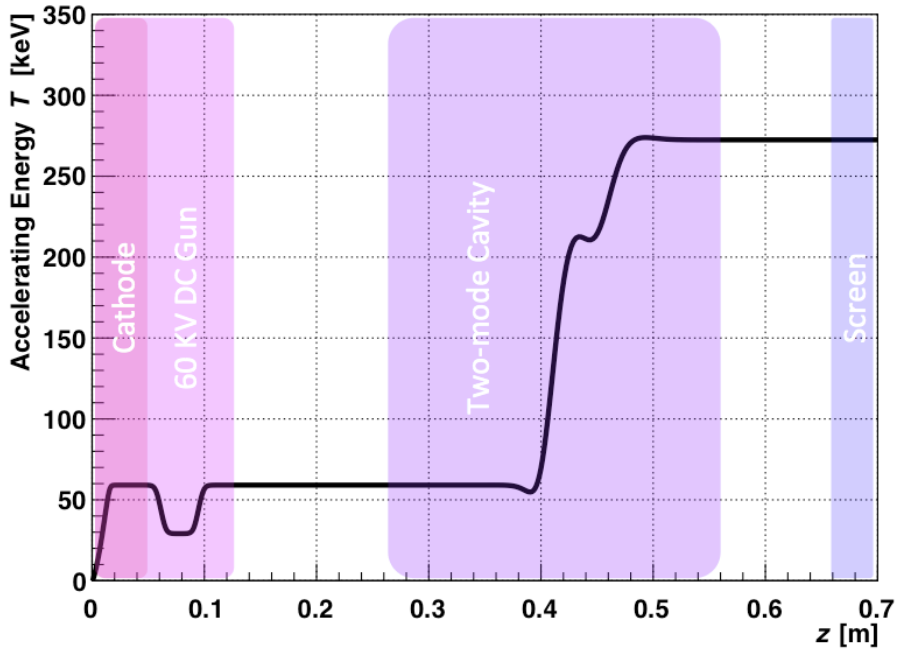


Figure 4.8: The variation of the accelerating energy  $T$  for the optimal 300 kV two-mode acceleration.

#### 4.2.4 The optimization result of the 3 MV acceleration

Table 4.5 summarizes the simulation result for 3 MeV acceleration. In this case, the system has three two-mode cavities. In order to minimize the energy dispersion  $\Delta T/T$  just below the last cavity, I optimized the system in each step to add the cavity one by one. Owing to the two-mode acceleration, the energy dispersion  $\Delta T/T$  can be reduced by ten times than the one-mode acceleration to compare the values at the outlet of Cavity3.

Table 4.6 shows the optimal values in order to minimize the energy spread  $\Delta T$ . These Amplitudes directly become the performance requirements for the practical two-mode cavities in order to manufacture the future 3 MV SRF-TEM

Figure 4.9 - 4.10 show the variations of the accelerating energy  $T$  for the optimal one-mode acceleration and two-mode acceleration respectively.

Table 4.5: The simulation result of the 3 MV acceleration. Each value is at the outlet of each cavity.

		Cavity1	Cavity2	Cavity3
One-mode Acceleration	$T$	1.17 MeV	2.38 MeV	3.59 MeV
	$\Delta T$	163 eV	269 eV	368 eV
	$\Delta T/T$	$1.39 \times 10^{-4}$	$1.13 \times 10^{-4}$	$1.03 \times 10^{-4}$
Two-mode Acceleration	$T$	1.13 MeV	2.17 MeV	3.07 MeV
	$\Delta T$	23.3 eV	29.4 eV	29.5 eV
	$\Delta T/T$	$2.06 \times 10^{-5}$	$1.35 \times 10^{-5}$	$9.61 \times 10^{-6}$

Table 4.6: The optimal vales of the accelerating modes for the acceleration for 3 MV

		Cavity1	Cavity2	Cavity3
One-mode	Amplitude of $TM_{010}$	24.8 MV/m	24.8 MV/m	24.8 MV/m
	Phase of $TM_{010}$	0.695 rad.	1.700 rad.	2.800 rad.
	Amplitude of $TM_{020}$	-	-	-
	Phase of $TM_{020}$	-	-	-
Two-mode	Amplitude of $TM_{010}$	18.3 MV/m	24.7 MV/m	24.7 MV/m
	Phase of $TM_{010}$	0.900 rad.	1.100 rad.	2.800 rad.
	Amplitude of $TM_{020}$	28.1 MV/m	6.2 MV/m	10.8 MV/m
	Phase of $TM_{020}$	3.200 rad.	2.100 rad.	5.520 rad.

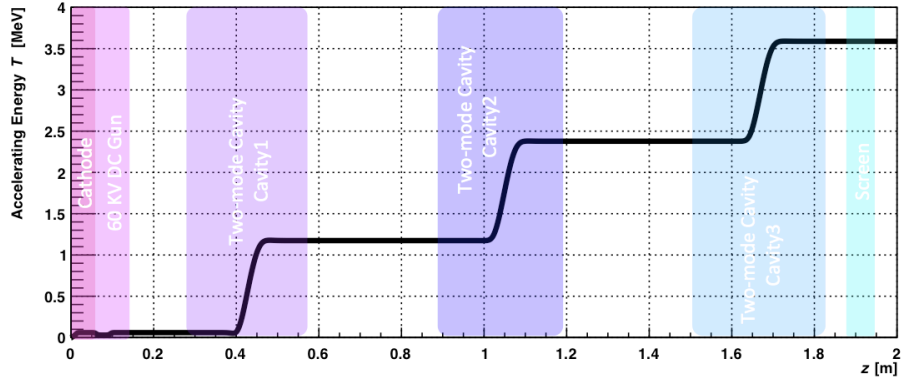


Figure 4.9: The variation of the accelerating energy  $T$  for the optimal 3 MV one-mode acceleration.

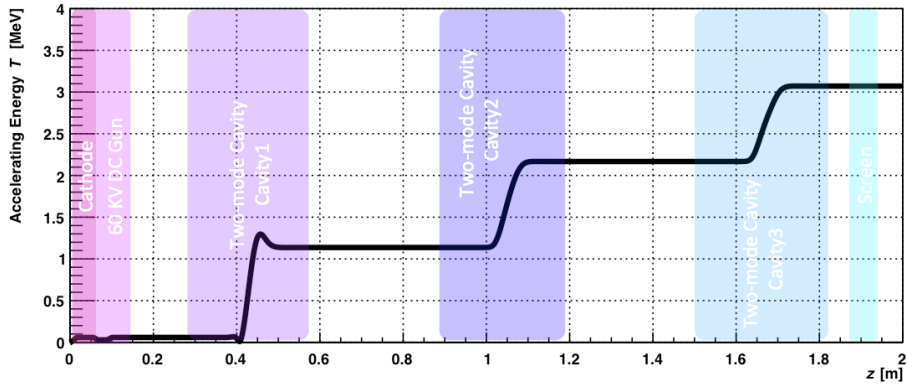


Figure 4.10: The variation of the accelerating energy  $T$  for the optimal 3 MV two-mode acceleration.

### 4.3 Requirement for Cavity Control

In the previous sections, it is confirmed that the two-mode acceleration is effective to reduce the energy spread  $\Delta T$ . And the set values in order to function the two-mode acceleration correctly are derived. In practical operations, we only have to set the previous values for each amplitude and phase. However, it is impossible to set these values without any errors. In this section, the control error effects on the energy spread  $\Delta T$  are investigated for the two-mode acceleration on 300 kV SRF-TEM prototype.

Now two types of the energy spread are introduced;  $\Delta T_1$  and  $\Delta T_2$ .  $\Delta T_1$  is the same as the previous section, which indicates the energy spread in one electron bunch.  $\Delta T_2$  is the energy spread resulting from the deviation of the averaged accelerating energy  $T$ . The ultimate energy dispersion  $\Delta T$  is calculated by

$$\Delta T = \sqrt{\Delta T_1^2 + \Delta T_2^2}. \quad (4.3.1)$$

Figure 4.11 - 4.14 show each control error effect on the energy spread and the energy dispersion. The horizontal axis indicates the quantity of the error. The top-left figure shows the deviation of averaged accelerating energy  $T$ . The top-right figure shows  $\Delta T_1$ . The bottom-left figure shows  $\Delta T_2$ . The top-right figure shows  $\Delta T_1$ . The bottom-left figure shows  $\Delta T_2$ . The bottom-right figure shows the energy dispersion  $\Delta T/T$  where ultimate energy spread  $\Delta T$  is calculated by Eq. (4.3.1). Here some goals of the energy dispersion  $\Delta T/T$  are set.  $\Delta T/T$  of  $1.0 \times 10^{-4}$  is the first goal for 300 kV SRF-TEM prototype. And  $\Delta T/T$  of  $4.0 \times 10^{-5}$  is the ultimate goal for 300 kV SRF-TEM prototype after commissioning. Table 4.7 summarizes the requirements on each parameter control for both energy dispersion goals. These values are used to define the targets for the RF control system for SRF-TEM.

Table 4.7: The control requirement for the two-mode acceleration of 300 kV SRF-TEM prototype.

Target	Amplitude of TM <sub>010</sub>	Amplitude of TM <sub>020</sub>	Phase of TM <sub>010</sub>	Phase of TM <sub>020</sub>
$1.0 \times 10^{-4}$	0.010 %	0.037 %	0.320 deg.	0.120 deg.
$4.0 \times 10^{-5}$	0.004 %	0.014 %	0.150 deg.	0.055 deg.

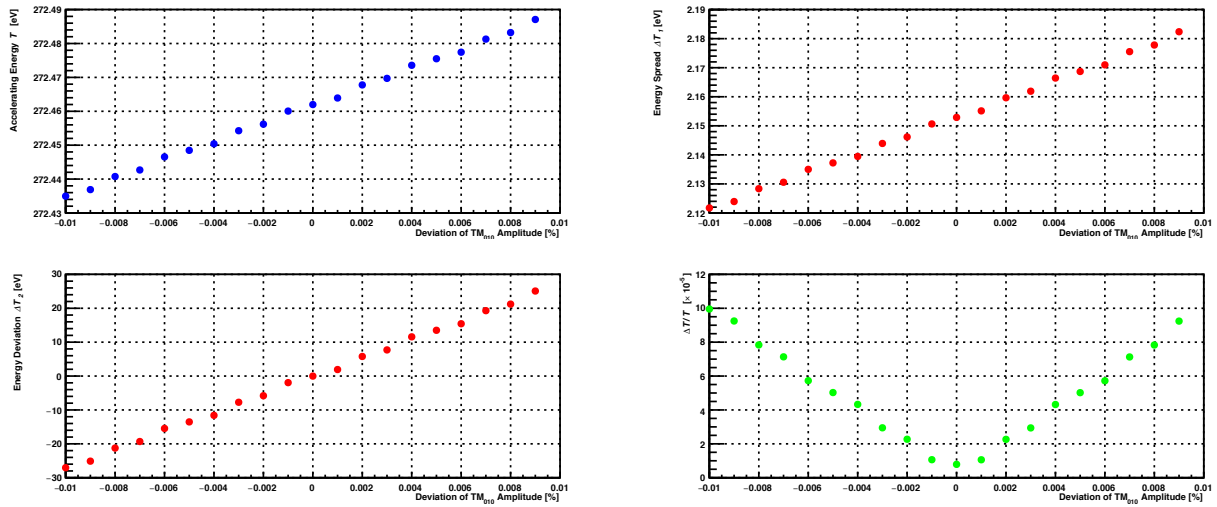


Figure 4.11: The control error effect on the energy spread for the amplitude of the  $TM_{010}$  mode.

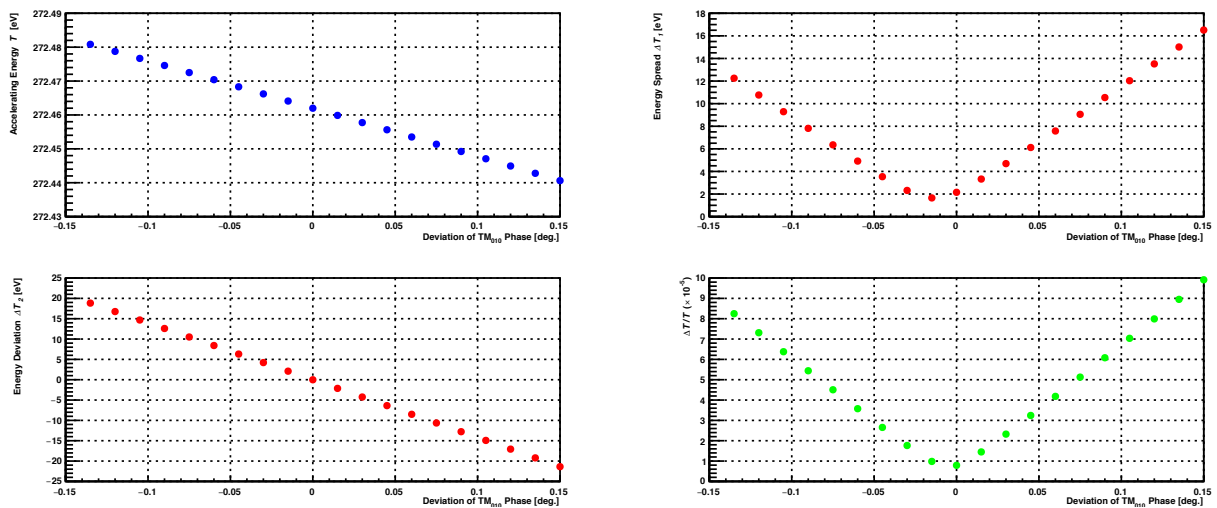


Figure 4.12: The control error effect on the energy spread for the phase of the  $TM_{010}$  mode.

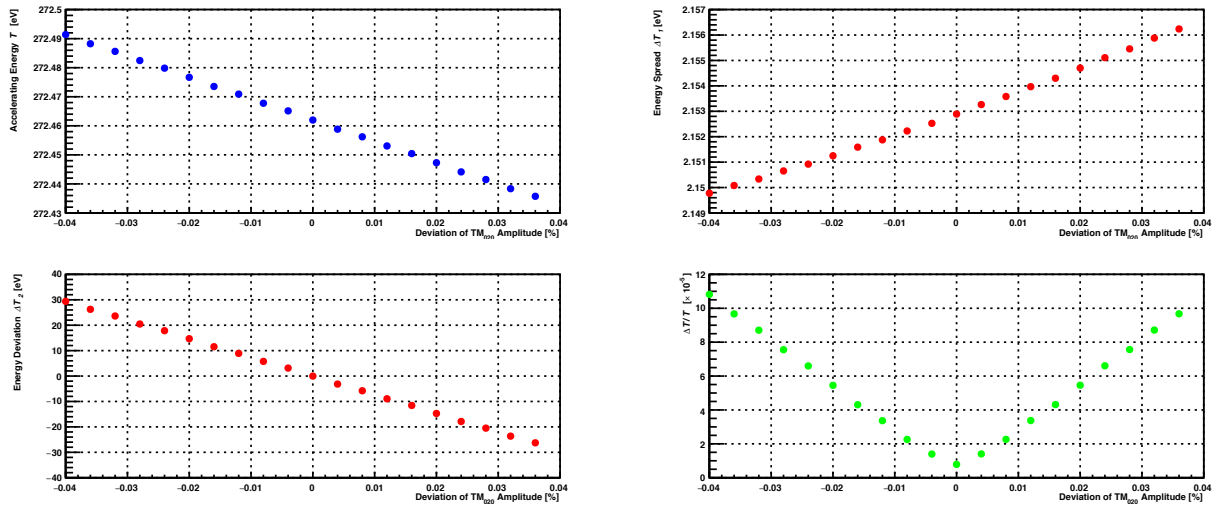


Figure 4.13: The control error effect on the energy spread for the amplitude of the  $TM_{020}$  mode.

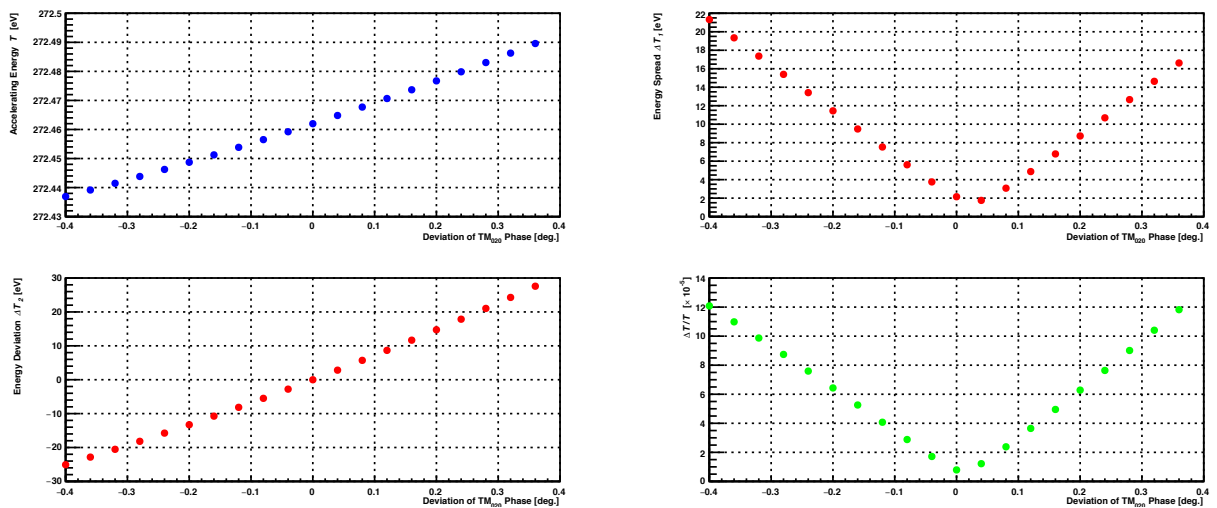


Figure 4.14: The control error effect on the energy spread for the phase of the  $TM_{020}$  mode.

# Chapter 5

## Development of Two-mode Cavity

This chapter describes the development of the two-mode cavity. First comes a fundamental description of superconducting cavities, followed by an explanation of design of the two-mode cavity. The fabrication process of the two-mode cavity is different from that of the conventional superconducting cavities. Finally the performance tests of the two-mode cavity is described.

### 5.1 Fundamental Property and Design of Superconducting Cavity

#### 5.1.1 Nature of Superconductivity

The phenomenon of superconductivity was found by Kammerlingh Onnes. The DC resistance of superconducting matter drops to zero when it is cooled. Superconductivity was theoretically explained by Bardeen, Cooper and Schrieffer[21]. Pairs of two electrons make Cooper pairs owing to the interaction with phonons and indicates the phenomena of Bose-Einstein condensation in lower energy state. This superconducting component carries the current with zero resistance. However in case of AC, normal conducting components also carry the current in the superconducting material, which leads to finite power dissipation. This dissipating power  $P_{\text{dis}}$  is defined as

$$P_{\text{dis}} = \frac{1}{2}R_s H^2 \quad (5.1.1)$$

where

$$R_s = R_{\text{BCS}} + R_0. \quad (5.1.2)$$

$R_{\text{BCS}}$  is the component which is explained by BCS theory, and satisfies the following equation;

$$R_{\text{BCS}} = \frac{A}{T} f^2 \exp\left(-\frac{\Delta(0)}{k_B T}\right) \quad (5.1.3)$$

Table 5.1: The characteristics of niobium[22][23][24].

Atomic Number	41
Atomic Weight	92.91
Density	8.570 kgm <sup>-3</sup>
Melting Point	2750 K
Boiling Point	5017 K
Transition Temperature	9.3 K
Specific Heat Capacity@298 K	265 JK <sup>-1</sup> kg <sup>-1</sup>
Thermal Conductivity@273 K	53 Wm <sup>-1</sup> K <sup>-1</sup>
Coefficient of Linear Expansion@293 K	7.3 × 10 <sup>-6</sup> K <sup>-1</sup>
Resistivity@273 K	273 nΩm
Re-crystallization Temperature	1200 K - 1600 K
Stress Release Temperature	1100 K

where  $A$  is a constant and  $\Delta(0)$  is a half of the energy required to destroy one Cooper pair at absolute zero temperature.  $k_B$  is Boltzmann constant.  $R_0$  represents the contribution from lattice defects and impurities and never disappear even at absolute zero temperature.

There are several materials which indicate the characteristics of superconductivity. The most suitable material for accelerating cavities is niobium (Nb). The transition temperature  $T_c$  is as high as 9.3 K, and it is possible to acquire niobium as highly pure state. Furthermore it is easy to process the material. The  $R_{BCS}$  of niobium satisfies the following empirical equation well when  $T < T_c/2$ ;

$$R_{BCS} = 2 \times 10^{-4} \frac{1}{T} \left( \frac{f}{1.5} \right)^2 \exp \left( -\frac{17.67}{T} \right). \quad (5.1.4)$$

Therefore we employ pure niobium as the material of the two-mode cavity. Table 5.1 summarizes several characteristics of niobium.

### 5.1.2 Resonant Mode in Pillbox

In this sub-section, a brief explanation of the RF acceleration principle by superconducting cavities is given (based on [25] and [26]) There are two types of RF accelerating cavities; normal conducting and superconducting. The difference lies in the boundary condition on the surface of the cavity. This sub-section features the boundary conditions for the superconducting cavities. In order to calculate the resonant electromagnetic fields, and Maxwell equations and the boundary conditions led by the nature of the superconductivity are used.

First,

$$\operatorname{div} \mathbf{D} = \rho \quad (5.1.5)$$

$$\operatorname{div} \mathbf{B} = 0 \quad (5.1.6)$$

$$\operatorname{rot} \mathbf{H} = \mathbf{j} + \frac{\partial \mathbf{D}}{\partial t} \quad (5.1.7)$$

$$\operatorname{rot} \mathbf{E} = -\frac{\partial \mathbf{B}}{\partial t} \quad (5.1.8)$$

and

$$\mathbf{D} = \varepsilon \mathbf{E} \quad (5.1.9)$$

$$\mathbf{B} = \mu \mathbf{H} \quad (5.1.10)$$

$$\mathbf{j} = 0 \quad (5.1.11)$$

$$\rho = 0 \quad (5.1.12)$$

are given. Here, considering a traveling wave along the  $z$ -direction in a cylindrical waveguide of radius  $a$  called “pillbox” like Figure 5.1,

$$\mathbf{E}(\mathbf{x}, t) = \mathbf{E}(x, y) \exp(ikx - i\omega t) \quad (5.1.13)$$

$$\mathbf{H}(\mathbf{x}, t) = \mathbf{H}(x, y) \exp(ikx - i\omega t). \quad (5.1.14)$$

Substituting these with  $\mathbf{E}$  and  $\mathbf{H}$  in Eq. (5.1.8), (5.1.7), and calculating each rotation,

$$(\nabla^2 - \omega^2 \varepsilon \mu) \mathbf{E} = 0 \quad (5.1.15)$$

$$(\nabla^2 - \omega^2 \varepsilon \mu) \mathbf{H} = 0 \quad (5.1.16)$$

are given. Here using a relational expression of  $\nabla_t^2 = \nabla^2 - \partial^2 / \partial z^2$ , Eq. (5.1.15) and (5.1.16) can be modified as

$$\{\nabla_t^2 + (\omega^2 \varepsilon \mu - k^2)\} \mathbf{E} = 0 \quad (5.1.17)$$

$$\{\nabla_t^2 + (\omega^2 \varepsilon \mu - k^2)\} \mathbf{H} = 0. \quad (5.1.18)$$

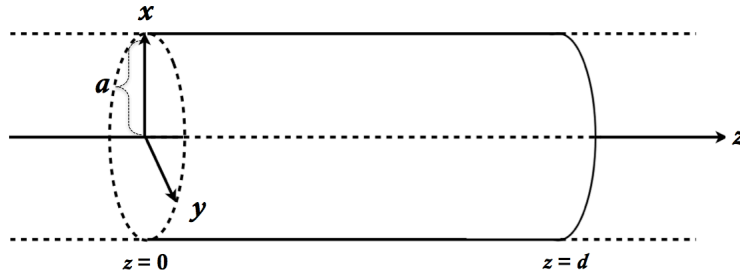


Figure 5.1: A pillbox-type cavity.

Table 5.2: The values of  $\rho_{mn}$ .

$m \setminus n$	1	2	3
0	2.405	5.520	8.654
1	3.832	7.016	10.173
2	5.136	8.417	11.620

Here, defining  $\omega^2 \varepsilon \mu - k^2 = \gamma^2$ , and focusing on  $E_z$  in cylindrical coordinate system, Eq. (5.1.17) gives

$$\nabla_{\text{t}}^2 E_z + \gamma^2 E_z = \left( \frac{\partial^2}{\partial r^2} + \frac{1}{r} \frac{\partial}{\partial r} + \frac{1}{r^2} \frac{\partial^2}{\partial \theta^2} + \gamma^2 \right) E_z = 0, \quad (5.1.19)$$

where  $r$  and  $\theta$  are new coordinates of cylindrical coordinate system, and

$$x = r \cos \theta \quad (5.1.20)$$

$$y = r \sin \theta \quad (5.1.21)$$

are satisfied with the original Cartesian coordinate system. Here, assuming that  $E_z$  can be written in the separable form as

$$E_z = R(r)\Theta(\theta) \quad (5.1.22)$$

and, that  $\Theta(\theta)$  satisfies the equation of a simple harmonic motion as

$$\frac{d^2 \Theta(\theta)}{d\theta^2} + m^2 \Theta(\theta) = 0, \quad (m = 1, 2, 3, \dots) \quad (5.1.23)$$

then, we get

$$\frac{d^2 R(\rho)}{d\rho^2} + \frac{1}{\rho} \frac{dR(\rho)}{d\rho} + \left( 1 - \frac{m^2}{\rho^2} \right) = 0. \quad (5.1.24)$$

Here  $\rho = \gamma r$ . Eq. (5.1.24) is the Bessel equation, whose solutions are the attenuated sine and cosine functions (Figure 5.2). In the case of superconducting, the cylindrical waveguide becomes a state close to a perfect conductor. Therefore at  $r = a$ ,  $E_{\parallel} = 0$  and  $H_{\perp} = 0$  are approximately established, and  $J_m(\gamma a) = 0$  is also satisfied. Figure 5.2 shows roots of  $J_m(\gamma a) = 0$ . Defining the  $n$ -th root of the  $m$ -th order Bessel function as  $\rho_{mn}$ ,  $\gamma a = \rho_{mn}$  is established. Each value of  $\rho_{mn}$  is listed in Table 5.2.

Using the above discussion, Eq. (5.1.22) is written as

$$E_z = E_0 e^{im\theta} J_m \left( \frac{\rho_{mn}}{a} r \right) e^{i(kz - \omega t)}. \quad (5.1.25)$$

In addition, modifying Eq. (5.1.17),

$$\begin{aligned} \mathbf{E}_t &= \frac{1}{\omega^2 \varepsilon \mu - k^2} (\nabla_t^2 \mathbf{E}_t) \\ &= \frac{1}{\omega^2 \varepsilon \mu - k^2} \left( \nabla_t \left( \frac{\partial E_z}{\partial z} \right) - i\omega \mu \mathbf{e}_z \times \nabla_t H_z \right) \end{aligned} \quad (5.1.26)$$

is given, where  $E_t$  is expressed only by  $E_z$  and  $H_z$ . In a similar way, Eq. (5.1.18) is written as

$$\mathbf{H}_t = \frac{1}{\omega^2 \varepsilon \mu - k^2} \left( \nabla_t \left( \frac{\partial H_z}{\partial z} \right) - i\omega \varepsilon \mathbf{e}_z \times \nabla_t E_z \right). \quad (5.1.27)$$

Accelerating modes which give the energy to charged particles satisfy both  $E_z \neq 0$  and  $H_z = 0$ . These modes are called “TM mode (transverse magnetic field modes)”. The complementary modes are “TE modes (transverse electric field modes)” which kick charged particles. Here focusing attention on TM modes, Eq. (5.1.26) and (5.1.27) are simplified as

$$\mathbf{E}_t = \frac{ik}{\gamma^2} (\nabla_t E_z) \quad (5.1.28)$$

$$\mathbf{H}_t = \frac{ik}{\gamma^2} (i\omega \varepsilon \mathbf{e}_z \times \nabla_t E_z) \quad (5.1.29)$$

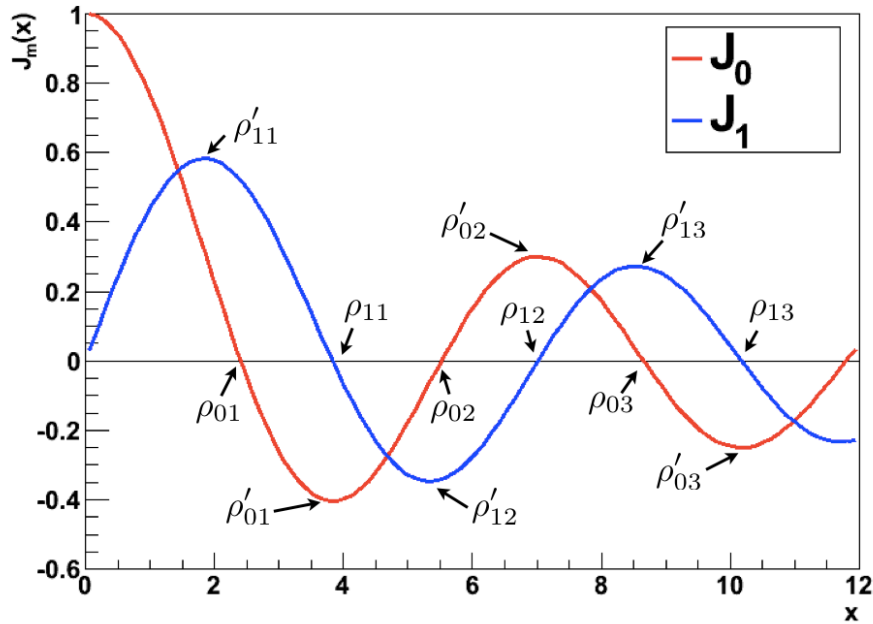


Figure 5.2: Bessel Functions.

respectively. Substituting Eq. (5.1.25) into these equations,

$$E_r = \frac{ik}{\gamma^2} \frac{\partial}{\partial r} E_z = \frac{ik}{\gamma} E_0 e^{im\theta} J'_m \left( \frac{\rho_{mn}}{a} r \right) e^{i(kz-\omega t)} \quad (5.1.30)$$

$$E_\theta = \frac{ik}{\gamma^2} \frac{1}{r} \frac{\partial}{\partial \theta} E_z = -\frac{k}{\gamma^2} \frac{m}{r} E_0 e^{im\theta} J_m \left( \frac{\rho_{mn}}{a} r \right) e^{i(kz-\omega t)} \quad (5.1.31)$$

$$H_r = \frac{i\omega\varepsilon}{\gamma^2} \frac{1}{r} \frac{\partial}{\partial \theta} E_z = -\frac{\omega\varepsilon}{\gamma^2} \frac{m}{r} E_0 e^{im\theta} J_m \left( \frac{\rho_{mn}}{a} r \right) e^{i(kz-\omega t)} \quad (5.1.32)$$

$$H_\theta = -\frac{i\omega\varepsilon}{\gamma^2} \frac{\partial}{\partial r} E_z = -\frac{i\omega\varepsilon}{\gamma} E_0 e^{im\theta} J'_m \left( \frac{\rho_{mn}}{a} r \right) e^{i(kz-\omega t)} \quad (5.1.33)$$

are given. These express TM modes propagating in the cylindrical waveguide. Furthermore, a pillbox-like cavity like Figure 5.1 is considered. The resonant field in this pillbox is limited by the boundary conditions of the cut-off walls at  $z = 0$  and  $d$ . When considering the superconducting state, the cavity becomes the state close to a perfect conductor. Therefore at  $z = 0$  and  $d$ ,  $E \perp = 0$ ,  $H \parallel = 0$  is approximately established, then  $E_r|_s = 0$  and  $E_\theta|_s = 0$  become the boundary conditions. Then the fields of TM modes in the superconducting cavity like Figure 5.1 are expressed as

$$E_z = E_0 J_m \left( \frac{\rho_{mn}}{a} r \right) \cos(m\theta) \cos \left( \frac{p\pi z}{d} \right) \quad (5.1.34)$$

$$E_r = \frac{k}{\gamma} E_0 J'_m \left( \frac{\rho_{mn}}{a} r \right) \cos(m\theta) \sin \left( \frac{p\pi z}{d} \right) \quad (5.1.35)$$

$$E_\theta = -\frac{k}{\gamma^2} \frac{m}{r} E_0 J_m \left( \frac{\rho_{mn}}{a} r \right) \sin(m\theta) \sin \left( \frac{p\pi z}{d} \right) \quad (5.1.36)$$

$$H_z = 0 \quad (5.1.37)$$

$$H_r = -\frac{\omega\varepsilon}{\gamma^2} \frac{m}{r} E_0 J_m \left( \frac{\rho_{mn}}{a} r \right) \sin(m\theta) \cos \left( \frac{p\pi z}{d} \right) \quad (5.1.38)$$

$$H_\theta = -\frac{\omega\varepsilon}{\gamma} E_0 J'_m \left( \frac{\rho_{mn}}{a} r \right) \cos(m\theta) \cos \left( \frac{p\pi z}{d} \right) \quad (5.1.39)$$

where  $\gamma = \rho_{mn}/a$  and  $k = p\pi/d$  are established. And  $m, p = 1, 2, 3, \dots$ , and  $n = 0, 1, 2, 3, \dots$ . Therefore the resonant frequency of  $TM_{mnp}$  in vacuum is

$$f = \frac{c}{2\pi} \sqrt{\left( \frac{\rho_{mn}}{a} \right)^2 + \left( \frac{p\pi}{d} \right)^2}. \quad (5.1.40)$$

This is the function of the radius and full-length of the cavity. The lowest-order mode of TM mode is  $TM_{010}$ , and its fields are

$$E_z = E_0 J_0 \left( \frac{2.405}{a} r \right) \quad (5.1.41)$$

$$H_\theta = -\frac{\omega\varepsilon}{\gamma} E_0 J'_0 \left( \frac{2.405}{a} r \right), \quad (5.1.42)$$

Table 5.3: The values of  $\rho'_{mn}$ .

$m \setminus n$	1	2	3
0	3.832	7.106	10.173
1	1.841	5.331	8.536
2	3.054	6.706	9.969

and other four components are all zero. High energy accelerators generally employ this  $TM_{010}$  mode, whose fields are distributed as (a) of Figure 1.1.

Calculating TE modes in the same way as TM modes, the electric-magnetic fields are

$$E_z = 0 \quad (5.1.43)$$

$$E_r = \frac{\omega\varepsilon m}{\gamma^2 r} E_0 J_m \left( \frac{\rho'_{mn}}{a} r \right) \sin(m\theta) \sin \left( \frac{p\pi z}{d} \right) \quad (5.1.44)$$

$$E_\theta = \frac{\omega\varepsilon}{\gamma} E_0 J_m \left( \frac{\rho'_{mn}}{a} r \right) \cos(m\theta) \sin \left( \frac{p\pi z}{d} \right) \quad (5.1.45)$$

$$H_z = E_0 J_m \left( \frac{\rho'_{mn}}{a} r \right) \cos(m\theta) \sin \left( \frac{p\pi z}{d} \right) \quad (5.1.46)$$

$$H_r = \frac{k}{\gamma^2} E_0 J_m \left( \frac{\rho'_{mn}}{a} r \right) \cos(m\theta) \cos \left( \frac{p\pi z}{d} \right) \quad (5.1.47)$$

$$H_\theta = -\frac{k m}{\gamma^2 r} E_0 J'_m \left( \frac{\rho'_{mn}}{a} r \right) \sin(m\theta) \sin \left( \frac{p\pi z}{d} \right) \quad (5.1.48)$$

where  $\gamma = \rho'_{mn}/a$  and  $\rho'_{mn}/a$  is the  $n$ -th root of the first derivative of  $m$ -th order Bessel function (Table 5.3). The resonant frequency of  $TE_{mnp}$  in vacuum is

$$f = \frac{c}{2\pi} \sqrt{\left( \frac{\rho'_{mn}}{a} \right)^2 + \left( \frac{p\pi}{d} \right)^2}. \quad (5.1.49)$$

Generally, the  $TM_{010}$  mode is called the fundamental mode, and plays a huge role in accelerating charged particles. Other higher order modes are called HOM, and disturb a stable acceleration and destabilize the beam.

### 5.1.3 Performance Index of Superconducting Cavity

Using the performance indices for superconducting cavities, we can evaluate the cavity performance quantitatively. In this sub-section, general performance indices and the important ones for this thesis are explained.

## Accelerating Voltage

When a charged particle path through the cavity where some resonant mode is existing, the total accelerating voltage  $V_{\text{acc}}$  that the particle receives is expressed as

$$V_{\text{acc}} = \left| \int_0^d E_z|_{r=0} e^{i\omega z/c\beta} dz \right|. \quad (5.1.50)$$

$V_{\text{acc}}$  is dependent on the relativistic  $\beta$  and the phase of the electric field. In general high energy accelerator developments,  $\beta = 1$  is chosen and the phase is set so that  $V_{\text{acc}}$  gets the maximum value. Therefore the averaged accelerating electric field  $E_{\text{acc}}$  becomes

$$E_{\text{acc}} = \frac{V_{\text{acc}}}{d}. \quad (5.1.51)$$

Generally,  $E_{\text{acc}}$  is an essential value to indicate the accelerating performance of the cavity. However it is not the most favorable one for our study, because the incident energy into the two-mode cavity is low as 60 kV ( $\beta = 0.45$ ). Therefore we use the maximum electric field on  $z$ -axis  $E_{\text{ap}}$ . This has no dependency on  $\beta$  and the incident phase.

## Quality Factor $Q_0$

Even if we cool a superconducting cavity, there must be a normal conducting component. This carries a finite current, then the stored energy in the cavity is lost. This dissipating power is called  $P_c$ , then the dissipating power per unit area is defined as

$$\frac{dP_c}{ds} = \frac{1}{2} R_s |\mathbf{H}|^2. \quad (5.1.52)$$

$R_s$  is about 10 n $\Omega$  in the case of superconducting cavities. The stored energy in the cavity is defined as

$$U = \frac{1}{2} \mu_0 \int_V |\mathbf{H}|^2 dv \quad (5.1.53)$$

$$= \frac{1}{2} \epsilon_0 \int_V |\mathbf{E}|^2 dv. \quad (5.1.54)$$

Here, a new performance index of “quality factor ( $Q_0$ )” is defined as

$$Q_0 = \frac{\omega_0 U}{P_c}. \quad (5.1.55)$$

This is the ratio of the stored energy in the cavity and the dissipating power on the cavity wall, and indicates how effective the energy can be stored in the cavity. Using Eq. (5.1.52) and (5.1.55),

$$Q_0 = \frac{\omega_0 \mu_0 \int_V |\mathbf{H}|^2 dv}{R_s \int_S |\mathbf{H}|^2 ds} \quad (5.1.56)$$

$$= \frac{G}{R_s} \quad (5.1.57)$$

Table 5.4: The performance indices of the designed two-mode cavity.

	TM <sub>010</sub>	TM <sub>020</sub>
Frequency [GHz]	1.30015224	2.59994554
$Q_0$	$1.86 \times 10^8$	$1.00 \times 10^8$
$R_{BCS}[\text{n}\Omega]$	$7.54 \times 10^2$	$3.01 \times 10^3$
$P_c[\text{W}]$	3.01	4.84
$R_a/Q_0[\Omega]$	$1.23 \times 10^2$	$4.53 \times 10^1$
$E_{ap}[\text{MV/m}]$	5.33	5.14
$A[\Omega^{1/2}\text{m}^{-1}]$	225.2	233.1

is established where  $G$  is called “form factor” which is not dependent on the size of the cavity but its shape. This value of  $G$  is calculated by electromagnetic simulations.

### Other Index

“Shunt impedance”  $R_a$

$$R_a = \frac{V_{acc}^2}{P_c} \quad (5.1.58)$$

indicates the accelerating efficiency. The ratio with  $Q_0$

$$\frac{R_a}{Q_0} = \frac{V_{acc}^2}{\omega U} \quad (5.1.59)$$

is independent of the size of the cavity and the resonant frequency, only determined by the cavity shape. Substituting Eq. (5.1.51) into Eq. (5.1.58) gives

$$E_{acc} = \frac{\sqrt{R_a/Q_0}}{d} \sqrt{Q_0 \cdot P_c}. \quad (5.1.60)$$

This  $\sqrt{R_a/Q_0}/d$  can be calculated by the electromagnetic simulation software “Superfish”. Furthermore, the relation of

$$E_{ap} \propto E_{acc} \quad (5.1.61)$$

is established, which leads to

$$E_{ap} = A \sqrt{Q_0 \cdot P_c}, \quad (5.1.62)$$

where this coefficient  $A$  can be calculated by Superfish as well.

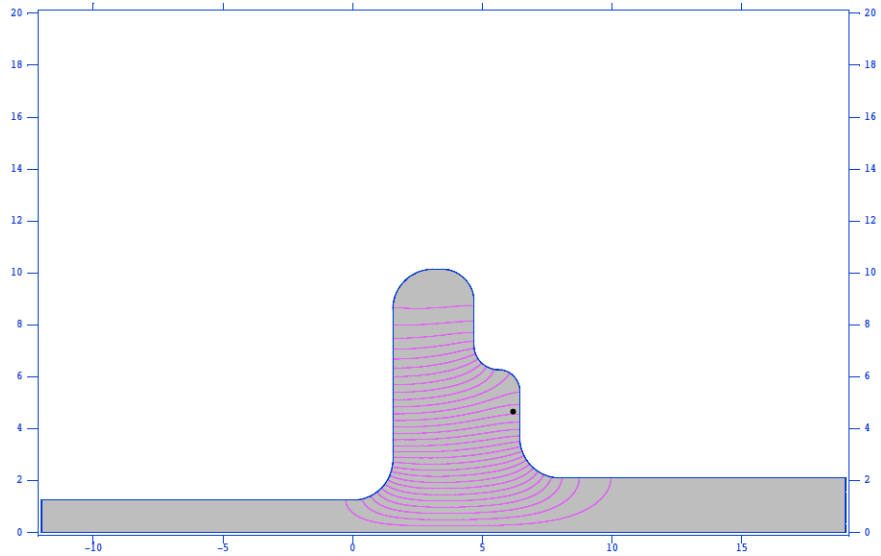
### 5.1.4 Design of Two-mode Cavity

In this subsection, the design of the two-mode cavity is described. The requirements for the design are the following;

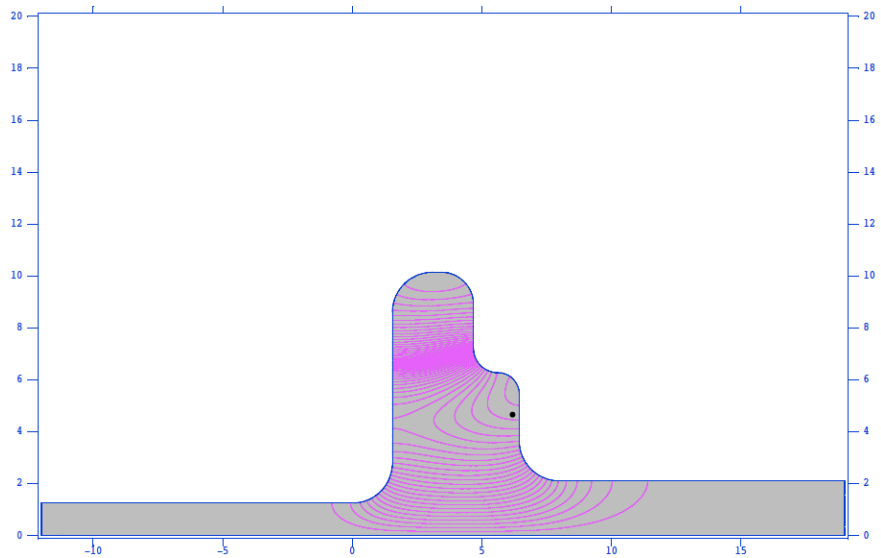
1. The  $Q_0$  of both the  $TM_{010}$  mode and the  $TM_{020}$  mode are almost the same value.
2. The ratio of the resonant frequency of the  $TM_{010}$  mode and the  $TM_{020}$  mode can reach 2.0000 using frequency tuners.

Conventionally, the higher-order resonant modes called HOM are unfavorable since they disturb accelerating beams. However, for our two-mode cavity, the  $TM_{020}$  mode, the second-harmonic resonant mode, is necessary in order to suppress the energy spread of the beam. Therefore, the quality factor  $Q_0$  which indicates the power efficiency to resonate the cavity has to be high for the  $TM_{020}$  mode as the fundamental  $TM_{010}$  mode. Additionally, in order to accelerate the electron bunch with 1.3 GHz, we have to set  $f_{020}$ , the resonant frequency of the  $TM_{020}$  mode just twice as much as  $f_{010}$ , the resonant frequency of the  $TM_{010}$  mode. However, in the process of the manufacturing the two-mode cavity, there must be some errors for the resonant frequencies. In order to correct these, we have two frequency turners as described in Sec. 3.1.1.

Superfish employs the finite difference method with non-uniform triangular meshes[27]. Using this, the two-mode cavity which satisfies the above requirements is designed. Figure 5.3 shows the section views and the electric field distributions of the designed two-mode cavity. Performance indices are listed in Table 5.4. These parameters are calculated by the condition that  $\beta = 1$ , accelerating length  $d = 1\text{m}$ ,  $E_{\text{acc}} = 1\text{ MV/m}$  and the temperature is 4.4 K. The temperature of 4.4 K is a little higher than the temperature of liquid helium (4.2 K), and this situation is realized when cooling the cavity with higher pressure than the atmosphere.



(a) The  $TM_{010}$  mode



(b) The  $TM_{020}$  mode

Figure 5.3: The section views and the electric field distributions of the two-mode cavity.

## 5.2 Fabrication of Two-mode Cavity

We manufactured the two-mode cavity of Figure 5.4 with the process as in Table 5.5. The main body of the cavity is made of seven parts described in Figure 5.4 - 5.5. The original niobium parts were processed in the form of ingots and sheets by the suppliers. After the delivery of materials, all fabrication processes were conducted in High Energy Accelerator Research Organization (KEK). In the following, a detailed explanation for each process is given.

### 5.2.1 Fabrication of Niobium Material

The cavity is made of pure niobium. The niobium comes from Brazil and Canada where niobium oxide is included in minerals. These minerals are crushed to powder, then melted in a vacuum furnace by electron beams in order to increase the purity of niobium. In this process, the cooled product called “ingot” includes high-purity niobium. Niobium sheets are produced by pressing and annealing the ingots. Niobium cavities are generally made of sheets. Our two-mode cavity is composed of ingots and sheets. Ingot shaving is conducted by a lathe, and the sheet is machined by the spinning process. Niobium sheets are fitted on a rotating iron mold, and deformed by a brass rod. Figure 5.5 shows all niobium parts that configures the body of the two-mode cavity.

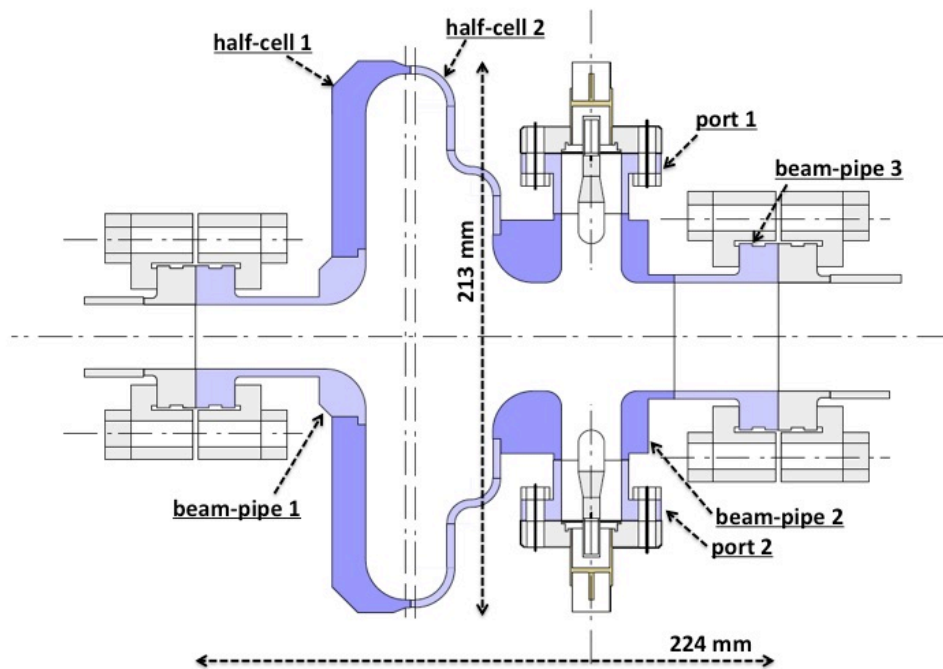
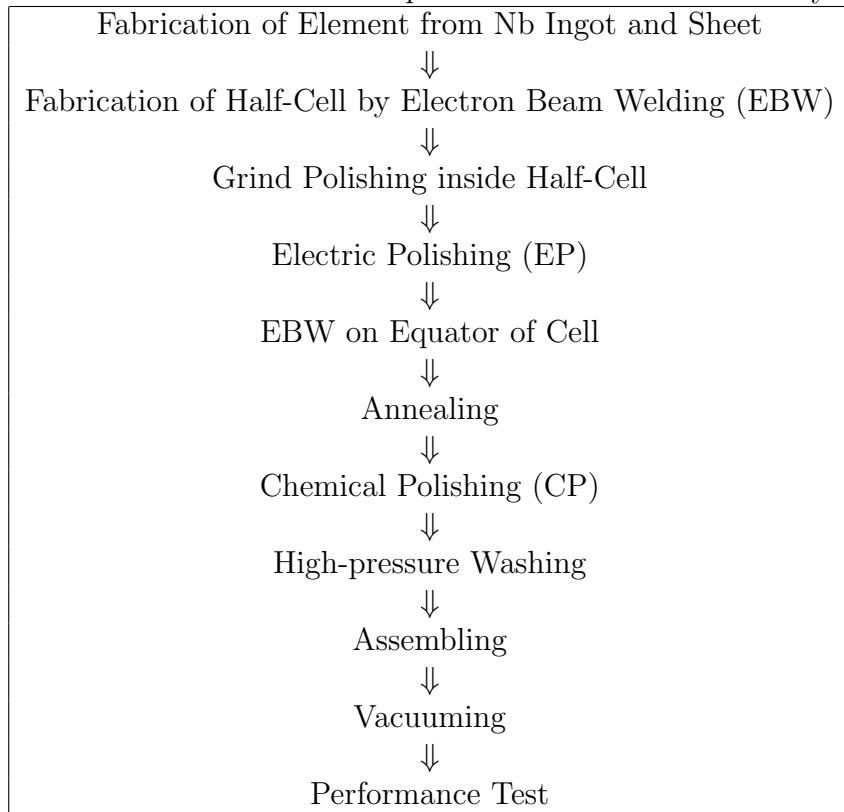


Figure 5.4: The overall design of the two-mode cavity.

Table 5.5: The fabrication process of the two-mode cavity.





(a) Half-cell 1.



(b) Half-cell 2.



(c) Beam-pipe 1.



(d) Beam-pipe 2.



(e) Beam-pipe 3.



(f) Port 1.



(g) Port 2.

Figure 5.5: The elements for the two-mode cavity fabricated from Nb ingots and sheets.

## 5.2.2 Electron Beam Welding

Generally, superconducting cavities are welded using the technique of “electron beam welding (EBW)”. EBW is performed in a vacuum furnace, where it is less likely for the welding point to be contaminated. Further, the penetration depth of EBW is large, thus it can weld thick material easily.

When using the technique of EBW, the following conditions have to be considered;

1. Electron beam current [mA]
2. Accelerating voltage of the electron beam [kV]
3. Feed rate of the welding point against the electron beam [mm/s]
4. Distance between the welding point and the electron gun (work distance) [mm]
5. Focal length of the EBW machine [mm].

It is important to find out the welding condition that leaves the clearest trace. However, it is more essential to find out the most stable condition, because there can be some deviations, for example, due to the non-uniformity of the cavity, the instability of the EBW machines. It is almost impossible to evaluate these deviations. On the other hand, it is possible to find out the sufficiently stable conditions.

To find out the stable conditions, we conducted the following;

1. Beam profile measurement with a comb-shaped sample
2. Plate EBW
3. Sample EBW.

We carried out the above steps for each welding point.

### Beam Profile Measurement With Comb-shaped Sample

It is important to know the beam size at the welding point in order to find out the stable conditions. However this is almost impossible to measure this directly. Instead, we did a beam profile measurement with a comb-shaped sample to know the beam size on the welding point indirectly. This comb-shaped sample is a long plate with a regular-pattern asperities resembling a washboard. Installed at 45 deg. angle with respect to the beam, this sample was sent in parallel to the gradient direction. The beam size was estimated by evaluating the welded traces. This enables us to determine the relationship between the bead width and the work distance at some focal length (Figure 5.6, 5.7).

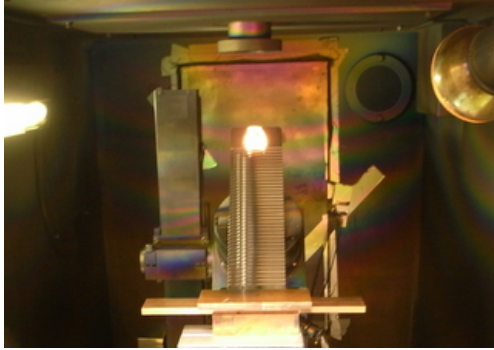


Figure 5.6: The setup for the comb measurement.

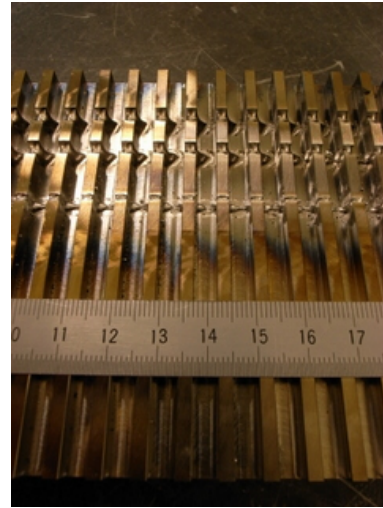


Figure 5.7: The weld bead made by the comb measurement.

### Plate EBW

The appropriate conditions of EBW are highly dependent on the thickness of the material. Therefore, using the plate sample with the same thickness as the cavity, it is possible to find a suitable condition to observe the welded beads. It is only a bead width that can be evaluate quantitatively. Other check points are; the presence of the back bead, the deepness of the depression of the bead, the uniformity of the bead surface. However it is difficult to evaluate these points quantitatively, then the observation depends on the subjective view of the observer. Figure 5.8 shows the result of a plate EBW test with several conditions for a beam current and a feed rate. Other conditions are; acceleration voltage of 140 kV, focal length 635 mm, work distance 270 mm.

### Sample EBW

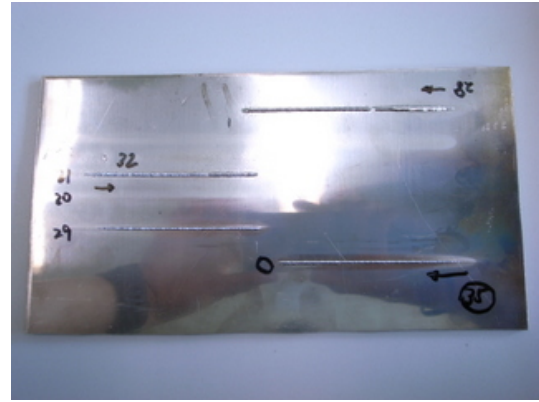
A sample EBW welds two materials on the boundary. It is preferable for the sample to have the work distance and the volume same as the real EBW. Figure 5.9 shows the tested material for a beam-pipe and a half-cell. After confirming that the condition is appropriate, the real EBW is conducted with the same current or higher current in the stable range. This is because the sample's volume is generally smaller than the real niobium materials.

### Real Production of EBW

The real production of EBW was conducted in the process of Table 5.6. Each production EBW was conducted under the condition that was acquired by the above three steps.



(a) The front bead.



(b) The back bead.

Figure 5.8: An example of the plane EBW.

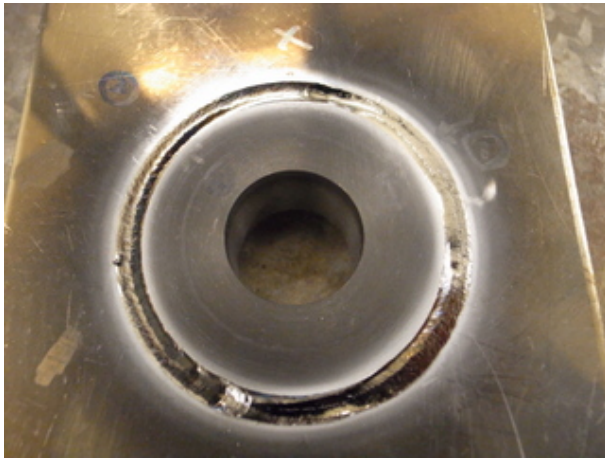
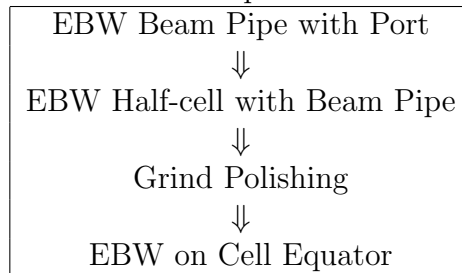


Figure 5.9: An example of the sample EBW.



Figure 5.10: EBW for an ingot Material.

Table 5.6: The real production of EBW.



### Ingot Material

General superconducting cavities uses 2.8 mm-thickness sheets for cavity walls. On the other hand, our two-mode cavity adopts the ingot material for the cavity wall in order to ensure

the strength enough to withstand the deforming of the tuning. Compared with sheets, the grain boundaries is much larger in ingot materials, and this may change the appropriate conditions for EBW. In order to investigate this effect, we conducted a EBW test with an ingot material. As a result, the bead is almost the same pattern as plates, and no conspicuous problem occurred at grain boundaries (Figure 5.10). Therefore, we treated ingots as well as plates with the same appropriate conditions.

### EBW on Equator of Cavity

The last EBW is for the equator of the two-mode cavity to bring together two half-cells. However, The back bead is inside the cavity, then it cannot be evaluated whether the welding is successful or not outside the cavity. KEK has an observation system to watch inside cavities called “Kyoto Camera”, however this was developed only for TESLA-like cavities, then cannot be utilized for our two-mode cavity due to the cavity’s narrow beam aperture. Therefore, a simple observation system was set up (Figure 5.11). In this system, a mirror is installed inside the cavity, and a telecamera was used to observe the back bead reflected on the mirror. Figure 5.12 shows the picture of the back bead, acquired by the system. With this picture, we decided that the back bead was observed, and the conducted EBW was successful. Based on these decision using this system, we conducted five discontinuous EBW at the equator.

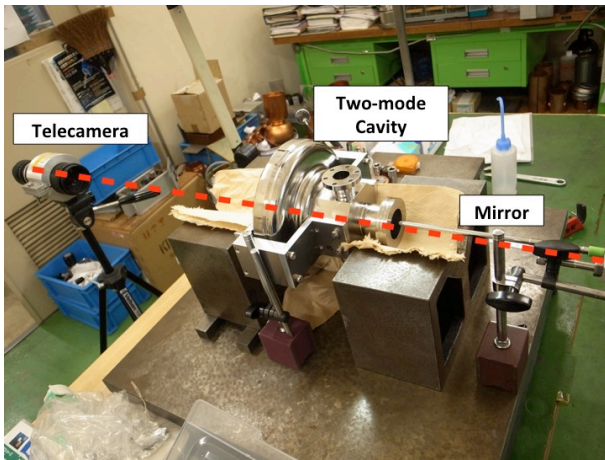


Figure 5.11: The observation system for the

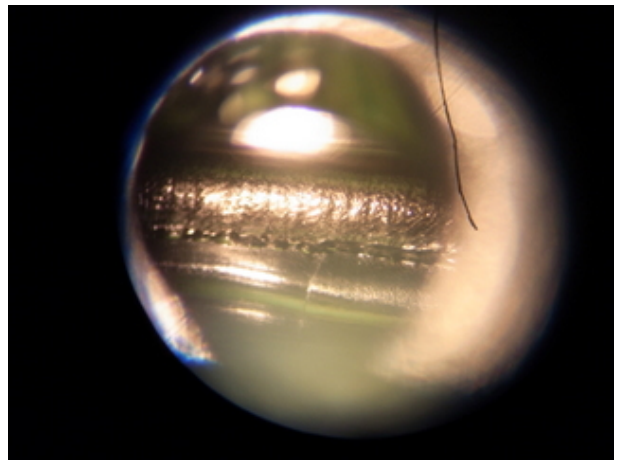


Figure 5.12: The observed back bead at the equator.

#### 5.2.2.1 Surface Polishing

It is desirable that there are less impurities and irregularities as much as possible on the surface of the cavity inside. If there are much impurities, these make the cavity’s resistance value large, then the destruction of superconducting state would occur locally. Additionally,

an electric field at irregularities gets larger, and emits field emission electrons, then this leads to the destruction of the superconducting state. Furthermore, much irregularities means an increase of the area, then this leads to the large resistance value as a whole cavity. Therefore, we tried to manufacture the better surface state to perform the following three processes.

## Grind Polishing

Figure 5.13 shows the back bead at the boundary between a half-cell and a beam-pipe. In order to polish mm-order irregularities like this picture, we did a grind polishing. This was conducted by a tool called “leutor” whose tip rotates at a high speed. On its tip, a carbide diamond cutter or grindstone are mounted (Figure 5.14). Half-cells are axial-symmetric. Then we set these on the electric pottery wheel, then polished stably by rotating it (Figure 5.15).

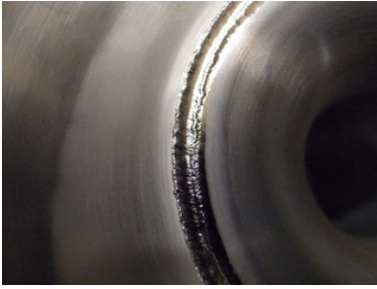


Figure 5.13: The back bead on the half-cell after the EBW.



Figure 5.14: The Leutor with a carbide blade and a grind stone.

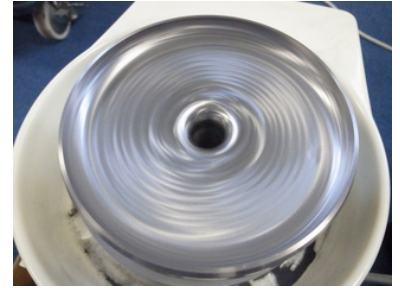
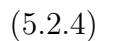
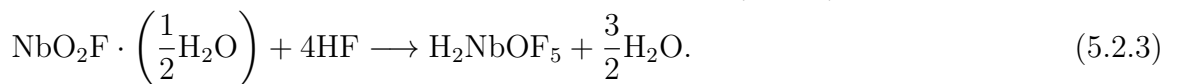
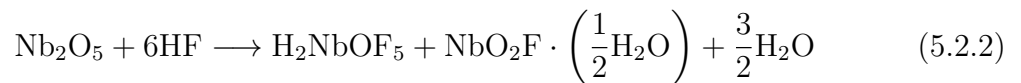


Figure 5.15: The half-cell on an electric pottery wheel after the grind polishing.

## Electro Polishing

Electro polishing (EP) is a technique where the object niobium is set as an anode, an aluminum rod is set as a cathode, and a container is filled with EP solution, then some voltage is applied (Figure 5.16). Our EP solution is composed of sulfuric acid (concentration: 98 %) and hydrofluoric acid (46 - 48 %), and the volume ratio is 9:1. The chemical reactions are the following three steps[28];



The first step is an oxidation of niobium. The second and the third steps are dissolution of niobium oxide. The reaction rate of EP can be adjusted by changing the applied voltage, and the polishing amount can be calculated by the integrated current. The polishing proceeds in proportion to the local strength of electric fields[29]. It is impossible to polish the surface uniformly, and the calculated polishing amount is only an approximate value. The reaction rate is strongly dependent on the temperature of the EP solution. The temperature increase of the EP solution is suppressed by a chiller.

Before the real EP, we conducted EP tests in order to determine the appropriate current density. This time,  $20 \text{ mA/cm}^2$  and  $50 \text{ mA/cm}^2$  were tested. The total polished amount was estimated to be  $52 \text{ }\mu\text{m}$  and  $40 \text{ }\mu\text{m}$  respectively by comparing the mass of the sample before and after the test. Figure 5.17 shows the tested sample. As can be seen, while the amount of polishing is the same level, the surface state are quite different. In order to observe in more detail, we utilized a laser microscope (Figure 5.18). Using its function, the average roughness was measured  $0.178 \text{ }\mu\text{m}$  at  $20 \text{ mA/cm}^2$  and  $0.161 \text{ }\mu\text{m}$  at  $50 \text{ mA/cm}^2$ . We chose the current of  $50 \text{ mA/cm}^2$ .

In the real EP, we aimed the  $70 \text{ }\mu\text{m}$  as the polishing amount. The polishing amount was measured by the integrated current in real time. The EP solution was kept at  $40 \text{ }^\circ\text{C}$  by the chiller. Figure 5.19 shows the half-cell after  $70 \text{ }\mu\text{m}$  EP. As can be seen, the surface was like a mirror, and the side of the beam aperture was recessed slightly. This is the trace of the grind polishing, and the concentration of the electric field never occur owing to its smooth surface.

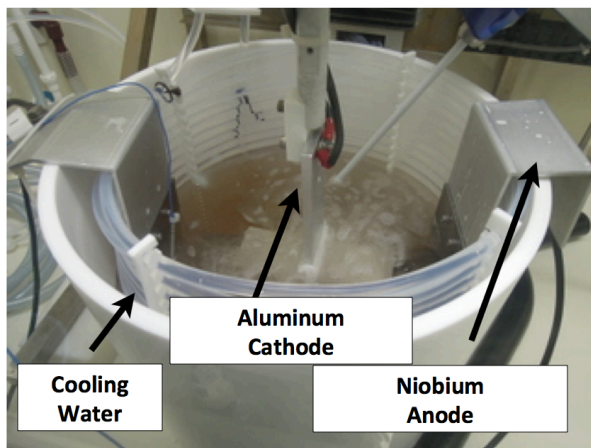


Figure 5.16: The setup of EP.

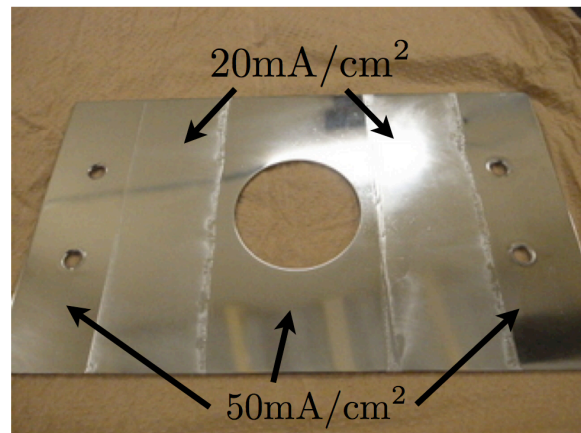
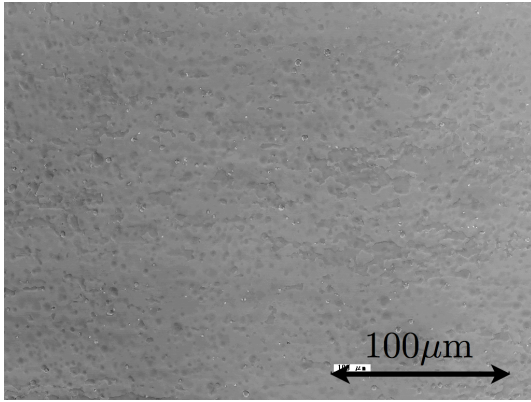


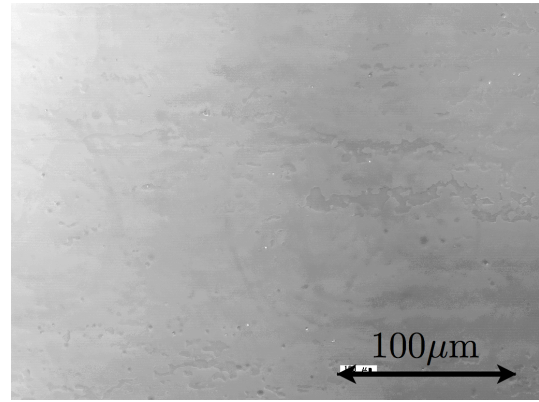
Figure 5.17: The test sample of EP.

## Chemical Polishing

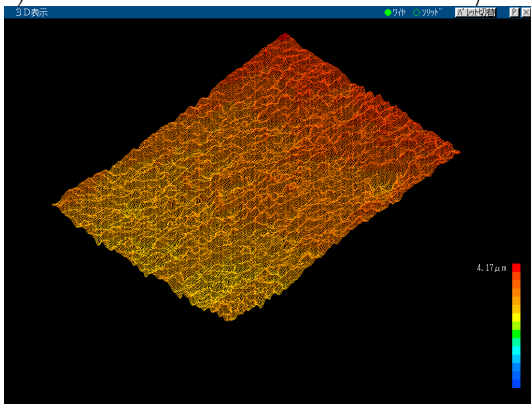
Chemical polishing (CP) utilizes the reaction of niobium with CP solution[30]. CP solution is composed of nitric acid (65 - 66 %), hydrofluoric acid (46 - 48%) and phosphoric acid (85



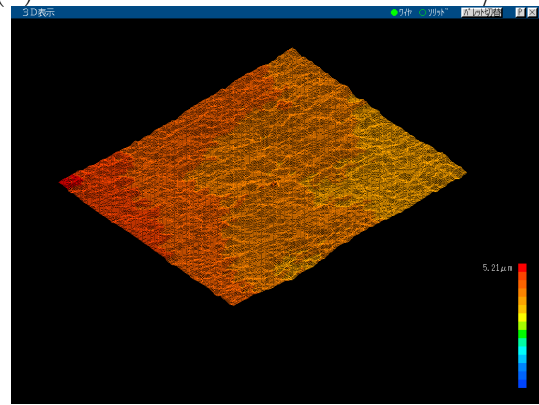
(a) The surface condition of 20 mA/cm<sup>2</sup>.



(b) The surface condition of 50 mA/cm<sup>2</sup>.



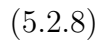
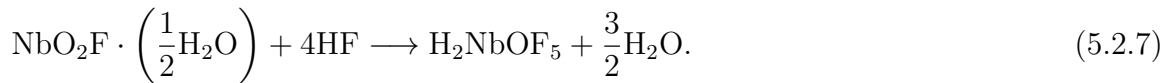
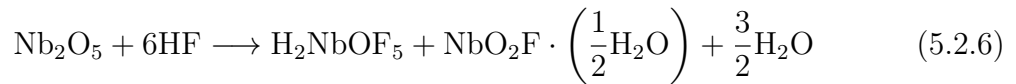
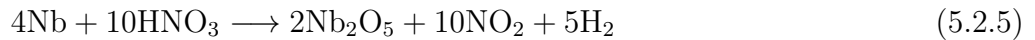
(c) The 3D surface condition of 20 mA/cm<sup>2</sup>.



(d) The 3D surface condition of 50 mA/cm<sup>2</sup>.

Figure 5.18: The observation of the EP test sample by a laser microscope.

%), and the volume ratio is 1: 1: 2 this time. The reaction proceeds as



The first reaction is the oxidation of niobium by nitric acid, and the second and the third reactions are the dissolution of niobium by hydrofluoric. The rate of CP reactions is much faster than EP, and increased exponentially depending on the solution temperature as is the case of EP. This saves time of polishing, however the control is difficult. In order to control the CP rate easily, we adjusted the amount of phosphoric acid which does not contribute to the reactions.

Another feature of CP is the non-uniform polishing due to the different rate at each grain

boundaries, and this makes the etchings of the grain boundaries. Our CP process was after the EP process in order to polish the equator of the cell, however the surface state worsened a little at other areas.

This time, we aimed 40  $\mu\text{m}$  CP polishing. As the volume rate was set as 1:1:2, the reaction rate was slow. Figure 5.20 shows the set up for CP. Ports of the cavity were closed and a valve was installed at the bottom beam-pipe. CP process was carried out for three minutes after closing this valve, filled with CP solution in the cavity, and functioning the mixer. After this, the valve was opened to dump the CP solution, then the inside of the cavity was cleaned with pure water. The polishing of 40  $\mu\text{m}$  was conducted repeating this process four times. After CP, we conducted an ultrasonic cleaning for thirty minutes with a cleaning solution called “FM-20” filled in the cavity and installing the cavity in the 50 °C bathtub in order to remove niobium oxide (Figure 5.21). After this, we washed the cavity with pure water for about fifteen minutes, closed the beam-pipes with aluminum foils, then carried the cavity to a cleanroom. The real polishing amount was estimated as 33  $\mu\text{m}$  by the amount of the niobium dissolved in the CP solution.

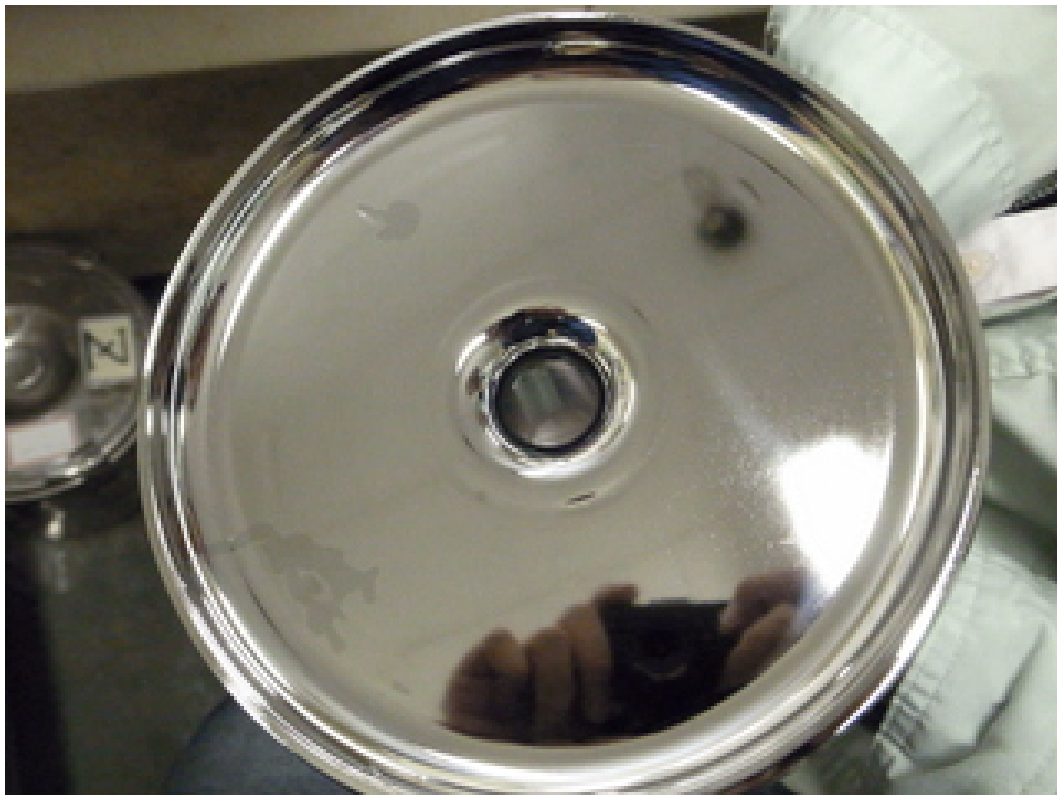


Figure 5.19: The half-cell after the EP process.



Figure 5.20: The setup of CP.



Figure 5.21: The ultrasonic cleaning after the CP process.

### 5.2.2.2 Annealing

Annealing is to heat the cavity installed in a vacuum furnace in order to release the stress in the cavity which was made in the process of EBW, and encourage the degasifying on the cavity surface. This time, we annealed the cavity at 800 °C for three hours. Figure 5.22 shows the cavity installed in the vacuum furnace. The cavity was set in a stainless jig in order to avoid non-uniform heating by direct radiation by heaters. Figure 5.23 shows the manufactured two-mode cavity after the annealing process.

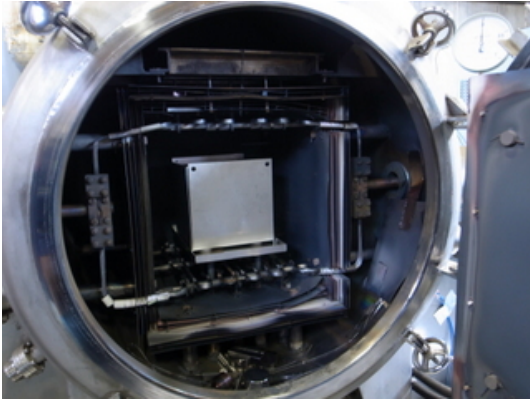


Figure 5.22: The two-mode cavity installed in a vacuum furnace.



Figure 5.23: The manufactured two-mode cavity after the annealing.

### 5.2.2.3 High-pressure Washing

We conducted a high-pressure washing in order to remove impurities on the cavity made in the process of EBW and polishings. This was conducted in a class 10 clean room<sup>1</sup> After this point, the inside of the cavity never touch the ambient air.

In order to wash the cavity uniformly, it was placed at a seat, and a bar was installed through the bottom beam-pipe (Figure 5.24). This bar has two holes with a diameter of 1 mm, located at 180 degrees opposite sides. Passing through these holes, high-pressure ultra-pure water was ejected with 3 - 5 MPa pressure<sup>2</sup>. By rotating the seat, and lowering the bar, we washed all inside area of the cavity. We wash the cavity for thirty minutes, and then, we assembled the cavity with jigs and flanges.

---

<sup>1</sup>Class 10 is a standard stipulated by the United States Federal Standard FS209, and this indicates the environment where there are less than 10 particles whose size is 0.5  $\mu\text{m}$  or more in 1  $\text{ft}^3$ . Now, FS209 is dead and replaced with JISB9920 compatible with international standards, and class 4 in JISB9920 responds to class 10 in FS209 [31].

<sup>2</sup>The purity of this water was maintained by the method using electric conductivity[32].

#### 5.2.2.4 Assembling

Impurities in the cavity cause residual resistance and become sources of field emission electrons that works as obstacles to put high power in the cavity. In order to shut out these, installing of jigs and flanges were carried out in the cleanroom, and the following processes of vacuuming and performance tests were conducted sealing the cavity. The cavity has two ports where each power antenna used for performance tests was installed. The cavity has two beam-pipe apertures, and the bottom one was closed out, and the vacuuming was carried out through the top one. Additionally, the frequency tuners were set in this step.

As the cavity is cooled to the temperature of liquid helium (4.2 K), the niobium body and other stainless jigs shrinks. The coefficient of linear thermal expansion of niobium and stainless are different <sup>3</sup>. In order to avoid the vacuum leak due to this difference of the shrink rate, we utilized an indium ribbon as a seal at the flange instead of a gasket (Figure 5.25). This indium ribbon is much flexible than usual gaskets, then reduces the probability of the leak. After assembling the cavity, it was vacuumed. The final vacuum level before the performance test was  $2 \times 10^{-6}$  Pa.

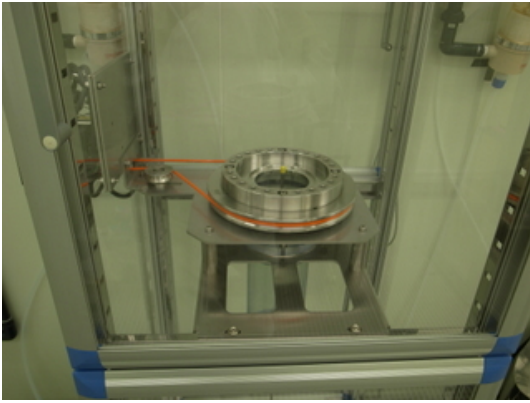


Figure 5.24: The seat for the high-pressure washing.



Figure 5.25: The indium ribbon for the sealing.

---

<sup>3</sup>Linear expansion coefficient of niobium at 293 K is  $7.3 \cdot 10^{-6} \text{ K}^{-1}$ , and stainless steel is  $14.7 \cdot 10^{-6} \text{ K}^{-1}$ [22][33].

## 5.3 Performance Test of Two-mode Cavity

In this section, the performance test of the manufactured two-mode cavity is described. Performance tests for superconducting cavities are called “vertical tests” where the cavities are settled in the 4.2 K (liquid He temperature) or 2 K (decompression) cryostat vertically, and cooled to be superconducting state. In this situation, the input power  $P_{\text{in}}$ , the reflection power  $P_{\text{r}}$  and the transmitted power  $P_{\text{t}}$  are measured to estimate the quality factor  $Q_0$  and the axial accelerating field  $E_{\text{ap}}$ <sup>4</sup>.

The cavity and the measurement system can be modeled as a lumped-constant circuit. A detailed description is given in Appendix B. Using that result, we estimated the performance indices.

### 5.3.1 Setup

The measurement system consists of the cooling system and the RF analog circuit (Figure 5.26). The two-mode cavity is cooled in the 4.2 K cryostat filled with liquid helium. This is surrounded by two heat-insulating layers. The inner one has a liquid nitrogen circulation system. The cavity hangs from the flange of the He layer, and has two ports where the RF powers come and go. These RF power  $P_{\text{in}}$ ,  $P_{\text{r}}$  and  $P_{\text{t}}$  are detected at the RF analog circuit by power sensors and monitors. The signals attenuate during propagating in cables. Therefore power values have to be corrected. This is called “cable correction”. The correction is made using correction factors

$$P_{\text{in}} = C_{\text{in}}P'_{\text{in}} \quad (5.3.1)$$

$$P_{\text{r}} = C_{\text{r}}P'_{\text{r}} \quad (5.3.2)$$

$$P_{\text{t}} = C_{\text{t}}P'_{\text{t}}, \quad (5.3.3)$$

where the power value with the prime symbol indicates the attenuated one measured at the RF analog circuit, and the bare one indicates the estimated power value at the port of the two-mode cavity. C indicates each correction factor.

The RF analog circuit is composed of several elements. In the following, a brief explanation is made for each component.

#### Signal Generator

This is the source of the RF signal, and determine the RF frequency. In vertical tests, this frequency can be changed in order to match the resonant frequency of the two-mode cavity. This signal generator receives the signal made at the mixer explained later. The amplitude of this signal is proportional to the frequency difference between the two-mode cavity and the signal generator.

---

<sup>4</sup>Generally,  $E_{\text{acc}}$  is calculated to discuss the cavity performance. However this is effective for  $\beta = 1$ , then we deal with  $E_{\text{ap}}$  which is the simple physical quantity.

## Frequency Counter

This measures the frequency of the output of the signal generator. Our frequency generator “HP 5350B” has a single digit accuracy[34].

## Linear RF Modulator

This can control the input RF power with an arbitrary factor from 0.000 to 10.000.

## RF Switch

This receives the signal which comes from a function generator, and output the product of the RF input from the linear RF moderator and the signal from the function generator. The received signal levels is TTL. When measuring the loaded quality factor  $Q_L$  of the two-mode cavity, square waves become the input and pulsed RF goes to the two-mode cavity. When measuring  $P_{in}$ ,  $P_r$  and  $P_t$ , 0 V becomes the input as logic 0. In the case of high voltage aging for discharge problems, the pulsed mode is utilized.

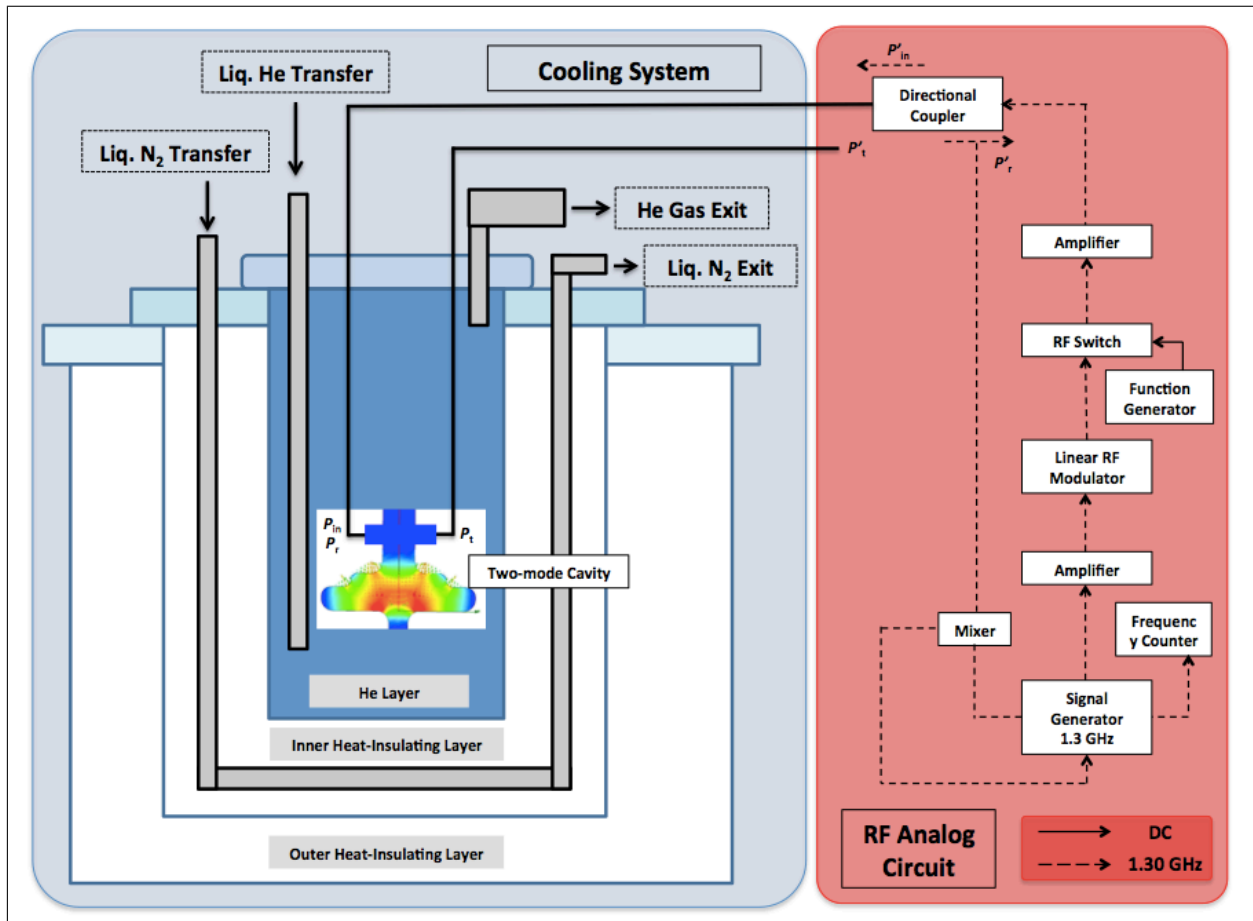


Figure 5.26: The setup for the vertical test.

## Directional Coupler

This can pick up the signal power of both the input RF  $P_{in}$  (going to the cavity) and the reflection RF  $P_r$  (coming from the cavity). The coupling constant is about 10 dB (1/10).

## Mixer

As described in the explanation of the “signal generator”, this outputs the signal whose amplitude is proportional to the frequency difference between the two-mode cavity and the signal generator. This signal goes to the signal generator, then the new frequency around 1.3 GHz goes around the system.

### 5.3.2 Measurement Scheme

The quality factor  $Q_0$  and the axial-peak accelerating field  $E_{acc}$  are estimated in the following steps;

1. Cable correction
2.  $Q_L$  measurement
3. Power measurement.

#### 5.3.2.1 Cable correction

As explained in the previous subsection, in order to estimate  $Q_0$  and  $E_{acc}$ , the RF values of  $P_{in}$ ,  $P_r$  and  $P_t$  at the port of the two-mode cavity are needed. However it is impossible to measure these directly, then using  $P'_{in}$ ,  $P'_r$  and  $P'_t$  measured at the RF analog circuit, we estimate the real  $P_{in}$ ,  $P_r$  and  $P_t$ . Figure 5.27 shows an example of the cable correction. In this case, we would like to know the attenuation of the path from ① to ②. First i), with an output signal from the signal generator, the power loss of the measurement system of the left side from the circulator is measured. Second ii), removing the reflection board, the target path between ① and ② is included. It is noted that during the cable correction, it is necessary to set the RF frequency “detuned” which means displaced from the resonant frequency of the two-mode cavity so that the RF signal cannot come into the cavity. In this case, the cable loss is calculated as

$$10.44 \text{ dBm} - 12.95 \text{ dBm} = -2.51 \text{ dB} \quad (5.3.4)$$

$$= 10^{-2.51/10} \quad (5.3.5)$$

$$\simeq \frac{1}{1.78}. \quad (5.3.6)$$

Here the unit of dBm is the absolute unit calculated as

$$x \text{ dBm} = 10^{x/10} \text{ mW} \quad (5.3.7)$$

For all paths to monitor  $P_{in}$ ,  $P_r$  and  $P_t$ , cable corrections have to be conducted in the same scheme.

### 5.3.2.2 $Q_L$ measurement

As explained in Sec. 5.1.3, the accelerating efficiency is expressed by the quality factor  $Q_0$  as

$$Q_0 = \frac{\omega_0 U}{P_c}. \quad (5.3.8)$$

In practice, there are other power losses; dissipating power at the input port  $P_e$  and transmitted power through the cavity  $P_t$ . Then the total dissipating power  $P_{tot}$  is calculated as

$$P_{tot} = P_c + P_e + P_t. \quad (5.3.9)$$

And a new parameter called the loaded quality factor  $Q_L$  is defined as

$$Q_L = \frac{\omega_0 U}{P_{tot}}. \quad (5.3.10)$$

In a similar way,  $Q_{in}$  and  $Q_t$  is defined as

$$Q_{in} = \frac{\omega_0 U}{P_e} \quad (5.3.11)$$

$$Q_t = \frac{\omega_0 U}{P_t}. \quad (5.3.12)$$

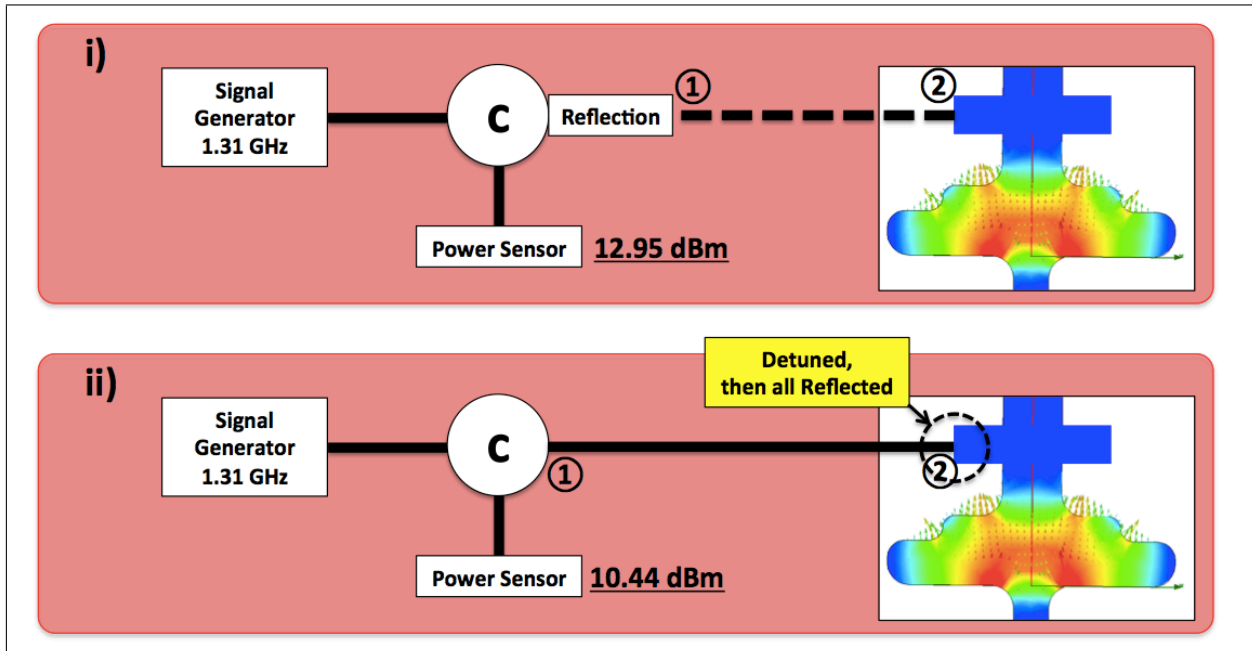


Figure 5.27: An example of cable correction. “C” indicates a circulator which has three ports, and only permits the counterclockwise path of the signal. “Reflection” indicates the RF reflection board where all power are reflected.

Using these parameters,  $Q_L$  is described as

$$\frac{1}{Q_L} = \frac{P_{\text{tot}}}{\omega_0 U} \quad (5.3.13)$$

$$= \frac{P_c + P_e + P_t}{\omega_0 U} \quad (5.3.14)$$

$$= \frac{1}{Q_0} + \frac{1}{Q_{\text{in}}} + \frac{1}{Q_t} \quad (5.3.15)$$

$$= \frac{1}{Q_0} \left( 1 + \frac{Q_0}{Q_{\text{in}}} + \frac{Q_0}{Q_t} \right) \quad (5.3.16)$$

$$= \frac{1}{Q_0} (1 + \beta_{\text{in}} + \beta_t) \quad (5.3.17)$$

$$= \frac{1}{Q_0} (1 + \beta^*), \quad (5.3.18)$$

where the new parameters  $\beta_{\text{in}}$  and  $\beta_t$  indicates the coupling strength of the power input coupler and output coupler respectively.  $\beta^*$  can be estimated using the values of  $P_{\text{in}}$  and  $P_r$  as described in Appendix B.

When the pulsed input power  $P_{\text{in}}$  is given into the cavity for a time enough to saturate the stored energy  $U$ , the transmitted power  $P_t$  decays with the rate as

$$P_t = \frac{4\beta^*\beta_t}{(1 + \beta^*)^2} P_{\text{in}} e^{-\omega_0(t-t_{\text{off}})/Q_L}, \quad (5.3.19)$$

where  $t$  indicates the elapsed time from  $P_{\text{in}}$  is turned on, and  $t_{\text{off}}$  indicates the time  $P_{\text{in}}$  is turned off (Figure 5.28). The decay time  $t - t_{\text{off}} = \tau_L$ , elapsing to reach a half value of the peak satisfies

$$e^{-\omega_0\tau_L/Q_L} = \frac{1}{2}. \quad (5.3.20)$$

Then,  $Q_L$  is calculated as

$$Q_L \simeq 0.6931 \times \tau_L \times \omega_0. \quad (5.3.21)$$

Now we measure this  $\tau_L$ , and already know the resonant angular frequency of the two-mode cavity  $\omega_0$ , then we can estimate the loaded quality factor  $Q_L$ .

Additionally, seeing the pattern of  $P_r$ , the coupling strength of  $\beta^*$  can be determined as “over-coupling ( $\beta^* \geq 1$ )” or “under-coupling ( $\beta^* < 1$ )” (Figure 5.28).  $\beta^*$  is estimated by

$$\beta^* = \frac{1 \pm \sqrt{\frac{P_r}{P_{\text{in}}}}}{1 \mp \sqrt{\frac{P_r}{P_{\text{in}}}}}, \quad (5.3.22)$$

where the upper double-sign corresponds is chosen for over-coupling and the down one is chosen for under-coupling. The values of  $P_{\text{in}}$  and  $P_r$  used to estimate  $\beta^*$  are measured in the next step “power measurement”.

### 5.3.2.3 Power measurement

Now we know the correction factors of cable correction and  $Q_L$  and whether  $\beta^*$  is over-coupling or under-coupling. Here, the ultimate goal to estimate  $Q_0$  and  $E_{ap}$  is accomplished.

First, using the corrected values of  $P_{in}$ ,  $P_r$  and Eq. (5.3.22), (5.3.18),  $Q_0$  is estimated. Next, replacing  $Q_0$  with  $Q_t$  in Eq. (5.1.60),

$$E_{acc} = \frac{\sqrt{R_a/Q_t}}{d} \sqrt{Q_t P_t} \quad (5.3.23)$$

is acquired. As described Sec. 5.1.3, there is a relation between  $E_{acc}$  and  $E_{ap}$  as

$$E_{ap} \propto E_{acc}, \quad (5.3.24)$$

then  $E_{ap}$  is expressed as

$$E_{ap} = A \sqrt{Q_t P_t}, \quad (5.3.25)$$

where  $A$  can be estimated by the numerical simulation and the values for the two-mode cavity is listed in Table. 5.4.

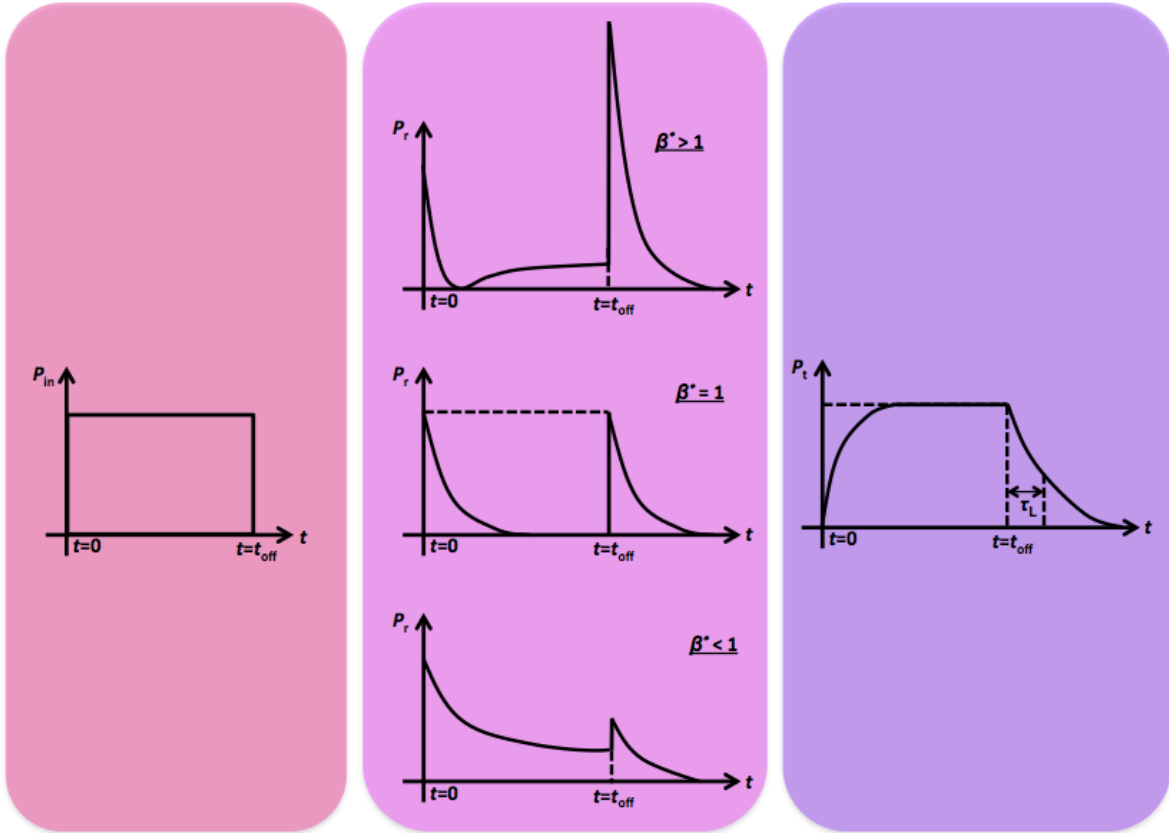


Figure 5.28: The schematic diagram of  $P_{in}$ ,  $P_r$  and  $P_t$ .

### 5.3.3 Result

Here the latest result is described. Figure 5.29 shows the result of  $E_{ap}$  and  $Q_0$ . The errors are due to the uncertainty of the power meter and the oscilloscope utilized in our measurement. Table 5.7 summarizes the highest achievement of  $E_{ap}$ , and  $Q_0$  at that time when the highest  $E_{ap}$  was recorded. The measured  $Q_0$  for both resonant modes are about a half of the simulated values listed in Table. 5.4 respectively. The practical values of  $Q_0$  are degenerated to some extent for the residual resistance and the outgassing.

The ratio of the resonant frequency  $f_{020}/f_{010}$  was measured as 1.9964. In order to satisfy

Table 5.7: The measured performance of the two-mode cavity.  $E_{ap}$  indicates the highest achievement and  $Q_0$  is the one estimated when the highest  $E_{ap}$  was recorded.

	TM <sub>010</sub>	TM <sub>020</sub>
Frequency [GHz]	1.30024902	2.59587465
$Q_0$	$(1.09 \pm 0.06) \times 10^8$	$(4.8 \pm 0.3) \times 10^7$
$E_{ap}$ [MV/m]	$11.0 \pm 0.3$	$7.8 \pm 0.3$

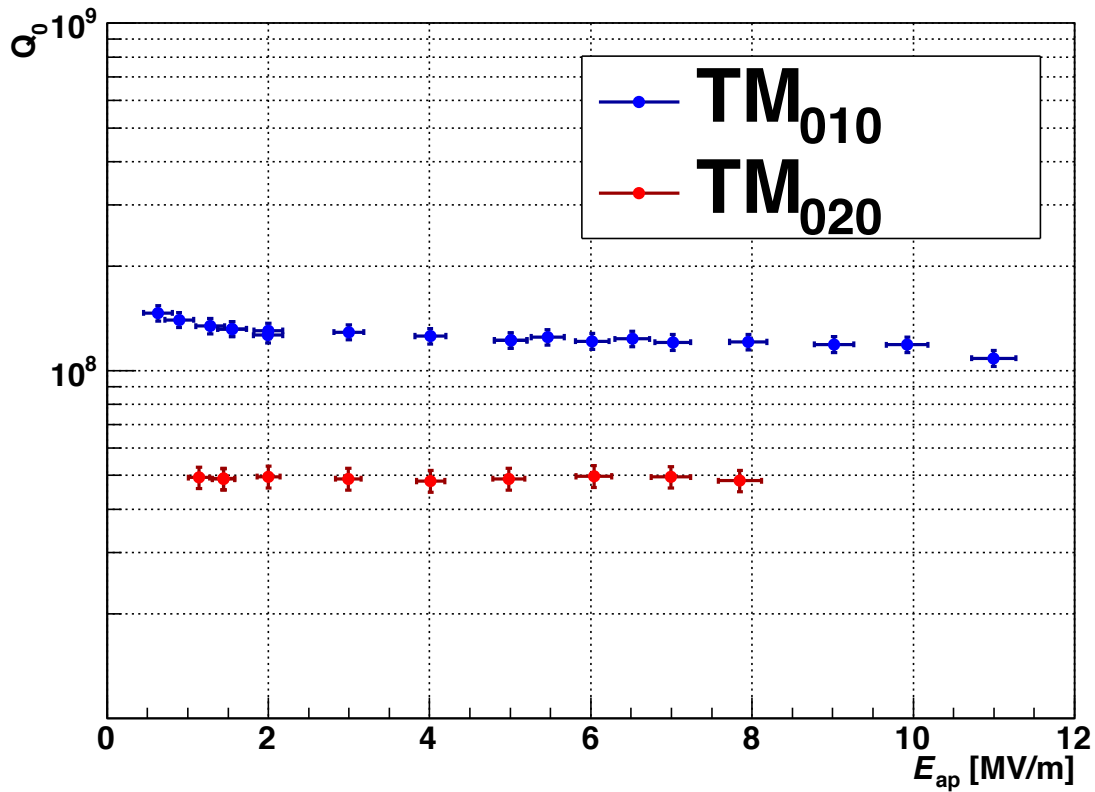


Figure 5.29: The latest result of the vertical test for the two-mode cavity.

all requirements for manufacturing the two-mode cavity raised in Sec. 5.1.4, we conducted the tuning test (next section).

## 5.4 Frequency Tuning Test of Two-mode Cavity

As described in Sec. 3.1.1, our two-mode cavity has two frequency tuners. Figure 5.30 indicates the tunable range of the frequency ratio of the manufactured two-mode cavity. The blue area indicates the tunable range in the case of the use of the span tuner, and the green one indicates in the case of the use of the piezo tuner. The red dotted line indicates the ratio of the manufactured two-mode cavity. This figure tells that we cannot reach 2.0000 in this two-mode cavity with the existing tuners.

In order to establish a new tuning process to realize 2.0000 as the frequency ratio, we manufactured a model cavity made of copper (Figure 5.31). This has the same shape as the niobium two-mode cavity. Firstly, the frequency ratio of this model cavity was 1.9949, which means it was impossible to realize 2.0000 with the existing tuners.

Thus, we introduced a new tuning process; shaving the inside of the model cavity (Figure 5.32). We shaved a point where the electric field of the  $TM_{020}$  mode is relatively stronger than that of the  $TM_{010}$  mode. Then,  $f_{020}$  can be altered largely, and the ratio can be changed. Table 5.8 summarizes the transition of the frequency and the ratio.

As the result, the ratio became 1.9976 that is inside of the tunable range of the niobium two-mode cavity. After the shaving process, we conducted the tuning test using the span tuner. Figure 5.33 shows the variation of the frequency ratio against the span tuner setting. In this test, we realized the frequency ratio of 2.0000. With this result, all requirements for manufacturing the two-mode cavity, described in Sec. 5.1.4, were achieved. When we manufacture the next niobium two-mode cavity, the above shaving process will be employed.

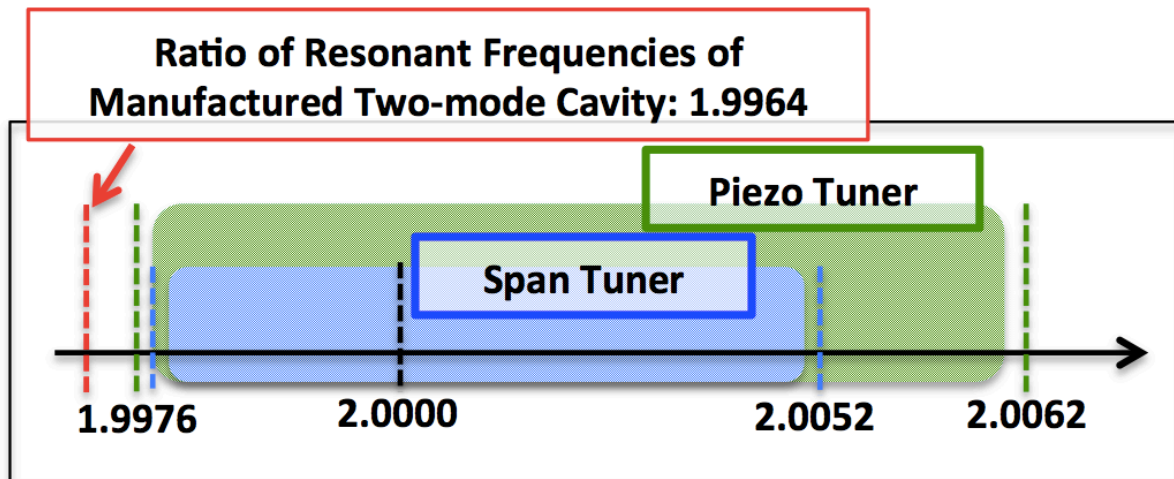
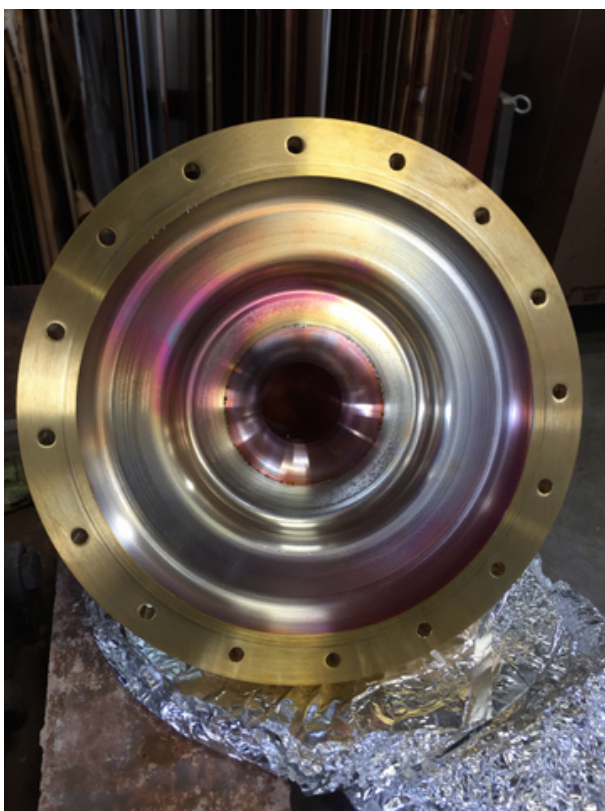


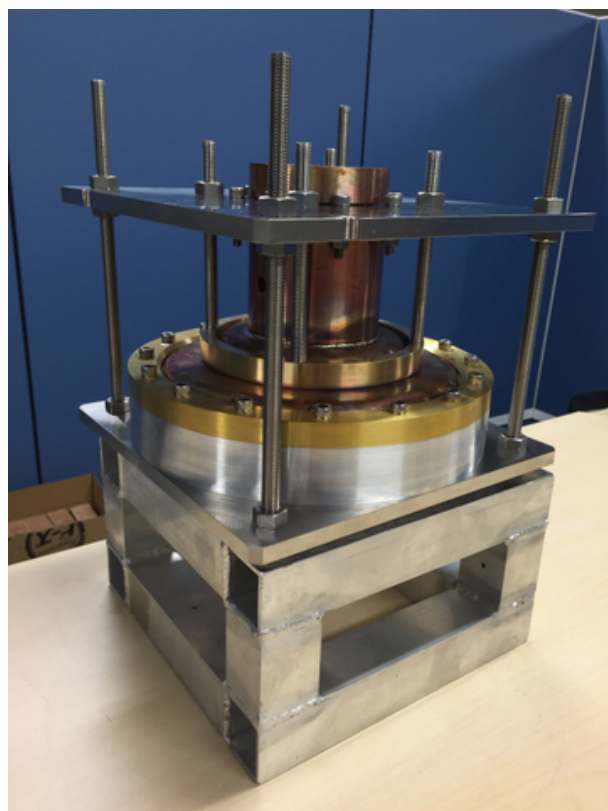
Figure 5.30: The tunable range of the frequency ratio of the manufactured two-mode cavity and its tuners.

Table 5.8: The transition of the frequency ratio before and after the shaving process.

	$f_{010}$ [GHz]	$f_{020}$ [GHz]	Ratio
Before shaving	1.2965	2.5864	1.9949
After shaving	1.2950	2.5869	1.9976



(a) The inside of the model cavity.



(b) The overview of the model cavity.

Figure 5.31: The model cavity made of copper.

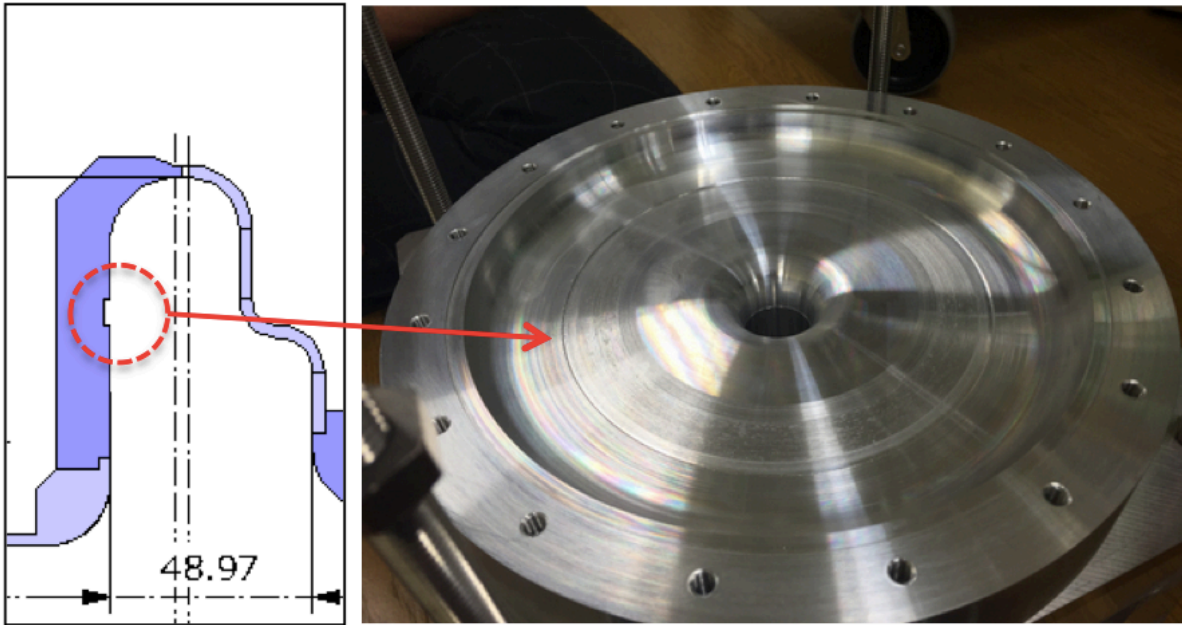


Figure 5.32: Shaving the inside of the model cavity. The width is 20.0 mm, and the depth is 1.0 mm.

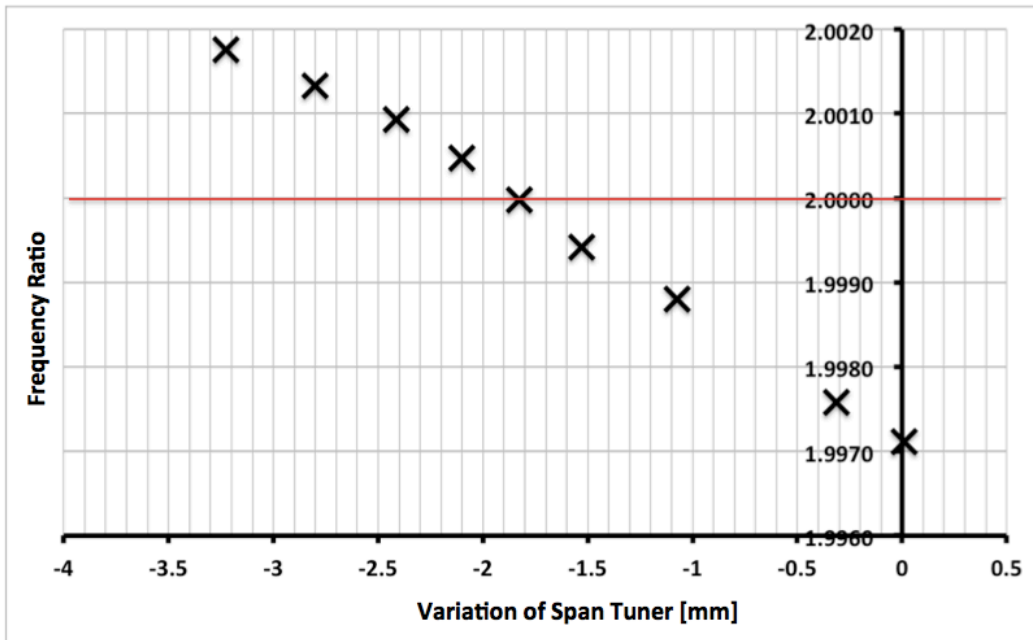


Figure 5.33: The variation of the frequency ratio against the span tuner.



# Chapter 6

## Development of Feedback Control System for Two-mode Cavity

This chapter describes the development of the feedback system for the two-mode cavity.

### 6.1 Source of Disturbance

In Appendix B, superconducting cavities are modeled by a lumped-constant circuit. Here, the important equations are shown again;

$$V_c \simeq \frac{2\sqrt{\beta^*}}{1 + \beta^*} \sqrt{R_a P_{in}} \frac{1}{1 + 2iQ_L} \frac{\omega - \omega_0}{\omega_0} e^{i\omega t} \quad (6.1.1)$$

$$= \frac{2\sqrt{\beta^*}}{1 + \beta^*} \sqrt{R_a P_{in}} \frac{1}{1 - i \tan \theta} e^{i\omega t} \quad (6.1.2)$$

$$= \frac{2\sqrt{\beta^*}}{1 + \beta^*} \sqrt{R_a P_{in}} \cos \theta e^{i(\omega t + \theta)} \quad (6.1.3)$$

$$\tan \theta = -2Q_L \frac{\omega - \omega_0}{\omega_0} \quad (6.1.4)$$

$$P_t = \frac{4\beta^* \beta_t \cos^2 \theta}{(1 + \beta^*)^2} P_{in} \quad (6.1.5)$$

where  $\theta$  is called as “tuning angle”, and  $V_c$  indicates the accelerating voltage. Using Eq. (6.1.3) and (6.1.5),

$$V_c \simeq \sqrt{\frac{R_a}{\beta_t}} \sqrt{P_t} e^{i(\omega t + \theta)} \quad (6.1.6)$$

is derived. Watching Eq. (6.1.3), it can be seen that the disturbance of  $P_{in}$  propagates to  $V_c$ . Additionally, if the deference between the input RF frequency  $\omega$  and the resonant frequency  $\omega_0$  fluctuate  $V_c$  too. In order to stabilize  $V_c$ , the transmitted power  $P_t$  can be used to monitor and control. Our feedback system was developed, based on the system of cEEL accelerator which monitors this  $P_t$ .

## 6.2 Setup of Feedback System For Two-mode Cavity

This section describes the configuration of our feedback system. The software part implemented on FPGA circuits is based on cERL accelerator. However, in our two-mode cavity both the  $TM_{010}$  mode and the  $TM_{020}$  mode have to be controlled at the same time. The configuration of the analog circuit is completely different from that of cERL accelerator. The schematic circuit for 1.3 GHz is shown in Figure 6.1. The configuration of 2.6 GHz is the same as the 1.3 GHz system. In the following, each component is explained.

### Signal Generator

The signal generator plays an important role in the functioning of the circuit. It supplies the 1.3 GHz signal to every circuit element so that it is called the “master oscillator”. In the vertical tests, its frequency is adjustable to match the two-mode cavity’s resonant frequency. On the other hand, the frequency is fixed in this feedback test. Therefore there occurs a difference between the frequency of the master oscillator and the resonant frequency which reduce the generated field according to Eq. (6.1.3) - (6.1.6). This is compensated by controlling the input power using FPGA based feedback circuit.

### Frequency Divider

The frequency divider is used to step-down the input frequency by a pre-determined factor. In this test, 1.3 GHz is divided to generate 81.25 MHz (1/16) and 10.15625 MHz (1/128). The former is the clock frequency for the FPGA circuit and it is also the sampling frequency for the RF signal which will be mentioned in detail later. The latter is used to make the 1.31 GHz signal (more precisely, 1.31015625 MHz) which is called the “local oscillator (LO)”. This is utilized to down-convert the RF signal of 1.3 GHz into 10 MHz signal which is called the “intermediate frequency (IF)”<sup>1</sup>.

### LO Signal Generator

This receives two signals; one is the 1.3 GHz master oscillators and the other is the 10 MHz signal which comes from the frequency divider. Using the two signals, the signal of 1.31 GHz is generated, whereas parasitic frequencies are also generated at the same time, for example 1.32 GHz and 1.29 GHz. A band pass filter is used to filter the signals from the down-converter in order to pass only the 1.31 GHz signal. In the case of the  $TM_{020}$  mode signal processing, the center frequency of the band pass filter is 2.61 GHz.

---

<sup>1</sup>More strictly this is 10.15625 MHz, however the notation of 10 MHz is utilized for the convenience.

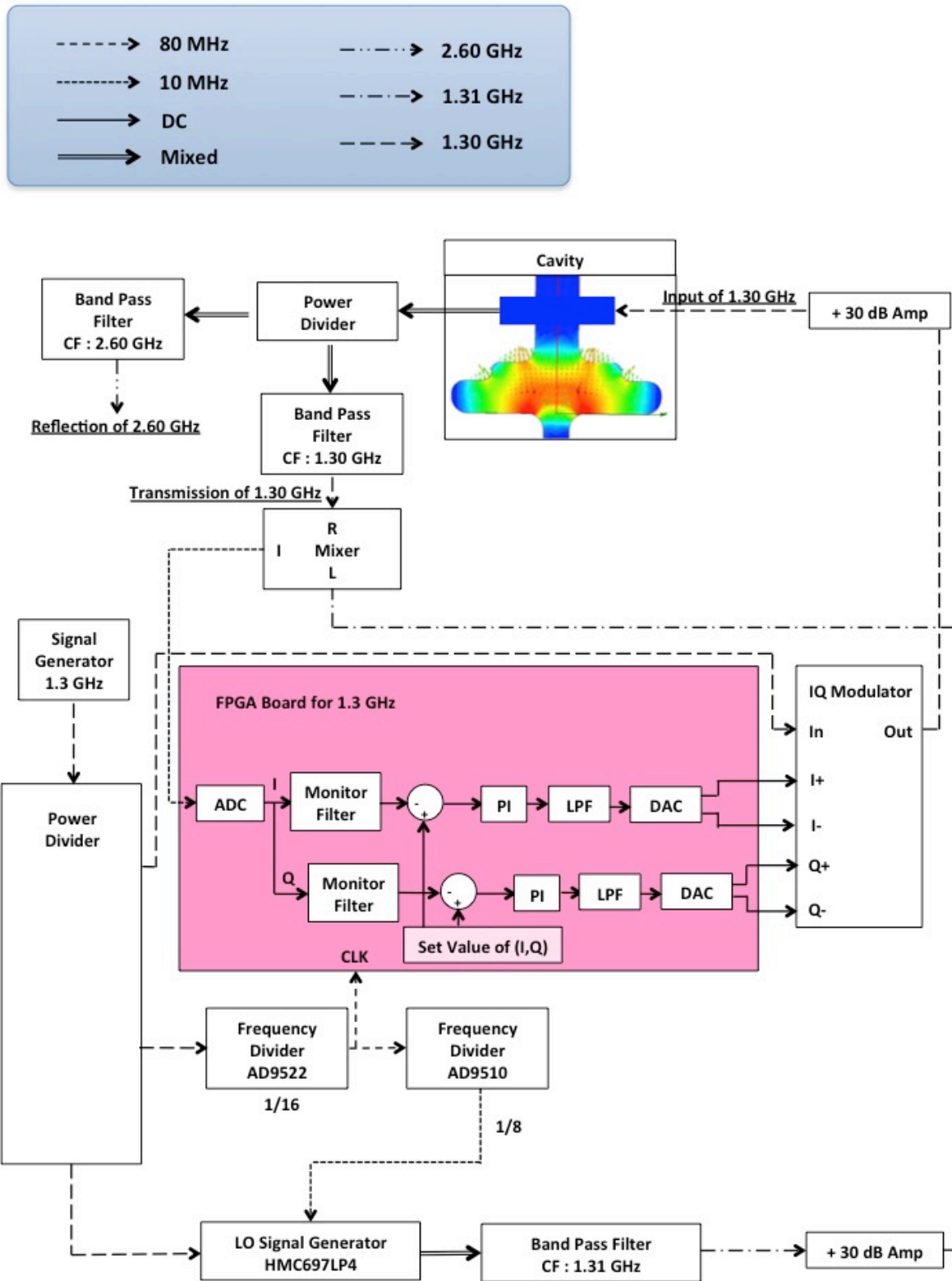


Figure 6.1: The feedback system developed for the two-mode cavity.

## Mixer

The mixer receives two inputs; one is the pickup signal of 1.3 GHz which comes from the two-mode cavity and the other is the LO of 1.31 GHz. In the mixer, two signals are mixed, i.e. multiplied mathematically to generate the intermediate frequency (IF) signal;

$$S_{\text{LO}} \times S_{\text{RF}} = A_{\text{LO}} \sin(2\pi f_{\text{LO}}t + \phi_{\text{LO}}) \times A_{\text{RF}} \sin(2\pi f_{\text{RF}}t + \phi_{\text{RF}}), \quad (6.2.1)$$

where  $A_{\text{LO}}$  is the amplitude of the LO signal,  $f_{\text{LO}}$  is the frequency of the LO, which is 1.31 GHz.  $\phi_{\text{RF}}$  is the phase of the LO signals. The notations for the 1.3 GHz RF signals are defined similarly. In the mixer,  $A_{\text{LO}}$  is set high enough, that is “ $A_{\text{LO}}$ ” is saturated. This enables the IF amplitude  $A_{\text{IF}}$  to be proportional to  $A_{\text{RF}}$ . Therefore the IF signal is generated by using sinusoidal product-sum formulae as

$$S_{\text{LO}} \times S_{\text{RF}} = A_{\text{IF}} \cos(2\pi f_{\text{IF}}t + \phi_{\text{IF}}) \quad (6.2.2)$$

$$A_{\text{IF}} = aA_{\text{RF}} \quad (6.2.3)$$

$$f_{\text{IF}} = f_{\text{LO}} - f_{\text{RF}} = 1.31 \text{ GHz} - 1.30 \text{ GHz} = 10 \text{ MHz} \quad (6.2.4)$$

$$\phi_{\text{IF}} = \phi_{\text{LO}} - \phi_{\text{RF}}, \quad (6.2.5)$$

where  $a$  is a proportional coefficient to convert  $A_{\text{RF}}$  to  $A_{\text{IF}}$ , and is assumed to be a constant. The signal of the frequency  $f_{\text{LO}} + f_{\text{RF}}$ , generated as a by-product, is cut off by the filter equipped with the mixer. Current FPGAs cannot process high frequency signal of  $O(1 \text{ GHz})$ . Therefore it is the common practice to convert a GHz signal to a MHz signal.

## FPGA

This is the key for the feedback. It receives only one signal as an input; down-converted IF signal  $S_{\text{IF}} = A_{\text{IF}} \sin(2\pi f_{\text{IF}}t + \phi_{\text{IF}})$ . Now we would like to measure both the amplitude  $A_{\text{IF}}$  and the phase  $\phi_{\text{IF}}$ , however we can only measure the value of the magnitude of  $S_{\text{IF}}$  at the time  $t$ . Therefore the sampling frequency  $f_s$  plays an active role. Here the idea of IQ sampling is introduced, based on [35]. Now we would like to know  $A$  and  $\phi$ . For this we transform them to  $I$  and  $Q$  as;

$$I = A \cos \phi \quad (6.2.6)$$

$$Q = A \sin \phi \quad (6.2.7)$$

$$A = \sqrt{I^2 + Q^2} \quad (6.2.8)$$

$$\phi = \text{atan} \left( \frac{Q}{I} \right). \quad (6.2.9)$$

Figure 6.2 shows the relation between  $A$ ,  $\phi$  and  $I$ ,  $Q$ . Now what we can do with one ADC is to measure  $x_t$ , the sampled IF signal  $S_{\text{IF}}$  at the time  $t$ . The data is acquired at 80 MHz as mentioned before. Therefore the sampling constant  $m$  is calculated as

$$m = \frac{80 \text{ MHz}}{10 \text{ MHz}} \quad (6.2.10)$$

$$= 8. \quad (6.2.11)$$

This situation is called “Oversampling”, therefore the acquisition phase resolution  $\Delta\phi$  is  $360 \text{ deg.}/8 = 45 \text{ deg.}$ . The value of  $x$  is expressed by using  $I$  and  $Q$  as

$$x_1 = I \cos(\Delta\phi) + Q \sin(\Delta\phi). \quad (6.2.12)$$

Then  $n$  samples are taken,

$$x_2 = I \cos(2\Delta\phi) + Q \sin(2\Delta\phi) \quad (6.2.13)$$

$$\dots \quad (6.2.14)$$

$$x_n = I \cos(n\Delta\phi) + Q \sin(n\Delta\phi). \quad (6.2.15)$$

using the notation of  $a_1, \dots, a_n$  and  $b_1, \dots, b_n$  instead of  $\cos(\Delta\phi), \dots, \cos(n\Delta\phi)$  and  $\sin(\Delta\phi), \dots, \sin(n\Delta\phi)$  then

$$a_1 I + b_1 Q - x_1 = 0 \quad (6.2.16)$$

$$\dots \quad (6.2.17)$$

$$a_n I + b_n Q - x_n = 0. \quad (6.2.18)$$

Multiplying  $a_i$  (or  $b_i$ ) and having sums from  $i$  to  $n$ , then

$$I \sum_{i=1}^n a_i^2 + Q \sum_{i=1}^n a_i b_i - \sum_{i=1}^n a_i x_i = 0 \quad (6.2.19)$$

$$I \sum_{i=1}^n a_i b_i + Q \sum_{i=1}^n b_i^2 - \sum_{i=1}^n b_i x_i = 0. \quad (6.2.20)$$

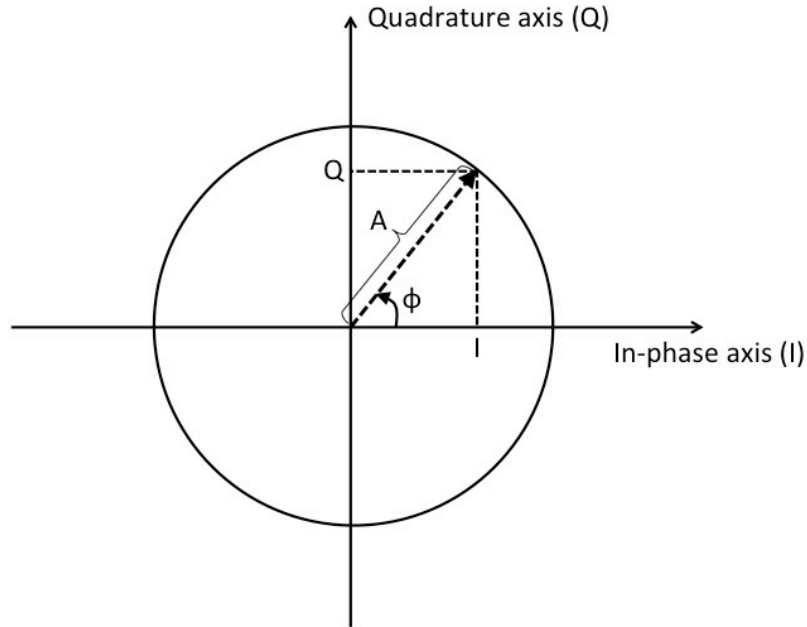


Figure 6.2: The definition of IQ.

Here new notations are introduced as

$$s_1 = \sum_{i=1}^n x_i b_i \quad (6.2.21)$$

$$s_2 = \sum_{i=1}^n x_i a_i \quad (6.2.22)$$

$$\alpha_{11} = \sum_{i=1}^n a_i^2 \quad (6.2.23)$$

$$\alpha_{12} = \alpha_{21} = \sum_{i=1}^n a_i b_i \quad (6.2.24)$$

$$\alpha_{22} = \sum_{i=1}^n b_i^2 \quad (6.2.25)$$

then

$$\alpha_{11}I + \alpha_{12}Q = s_1 \quad (6.2.26)$$

$$\alpha_{12}I + \alpha_{22}Q = s_2. \quad (6.2.27)$$

Now  $n = 8$  and  $\Delta\phi = 45$  deg. then

$$\sum_{i=1}^n \sin(i\Delta\phi) \cos(i\Delta\phi) = \alpha_{12} = \alpha_{21} = 0 \quad (6.2.28)$$

$$\sum_{i=1}^n \sin^2(i\Delta\phi) = \alpha_{22} = \frac{n}{2} = 4 \quad (6.2.29)$$

$$\sum_{i=1}^n \cos^2(i\Delta\phi) = \alpha_{11} = \frac{n}{2} = 4 \quad (6.2.30)$$

are establish. Using these equations with Eq. (6.2.26), (6.2.27),

$$I = \frac{2s_1}{n} \quad (6.2.31)$$

$$Q = \frac{2s_2}{n} \quad (6.2.32)$$

are derived. Substituting Eq. (6.2.21), (6.2.22) into the above equations,

$$I = \frac{2}{n} \sum_{i=1}^n x_i \sin(i\Delta\phi) \quad (6.2.33)$$

$$Q = \frac{2}{n} \sum_{i=1}^n x_i \cos(i\Delta\phi) \quad (6.2.34)$$

are acquired. From these equations,  $I$  and  $Q$  can be calculated using the 8 continuous ADC values.

After calculating  $I$  and  $Q$  from ADC,  $I$  and  $Q$  are compared with the set values. With its difference, “PI control process” is conducted. “P” denotes “proportional control” which outputs the proportional signal against the input. And “I” denotes “integral control” which outputs the time-integral of the input. These control strength can be adjusted to minimize the fluctuation of  $I$  and  $Q$ . After the PI control, the new digital signal are processed at a low pass filter (LPF), then converted into new  $I$  and  $Q$ . In our FPGA circuit, additional LPF called “monitor filter” was installed in front of the PI control in order to reduce the ADC noise. This cut-off frequency was set at 5 kHz.

## 6.3 Performance Test

We did the performance tests in two ways;

1. Single feedback
2. Dual feedback

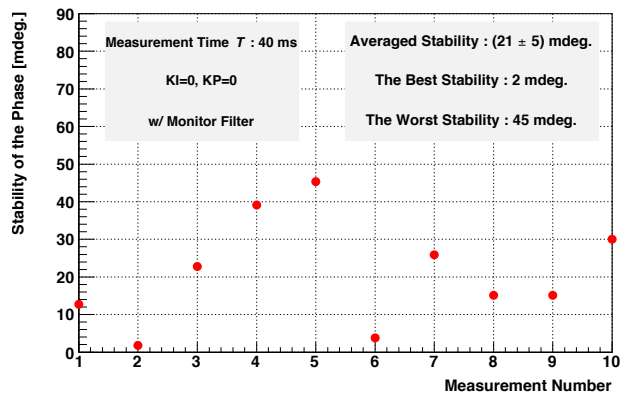
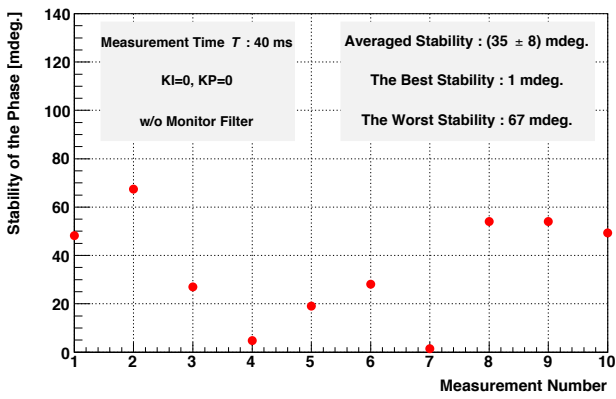
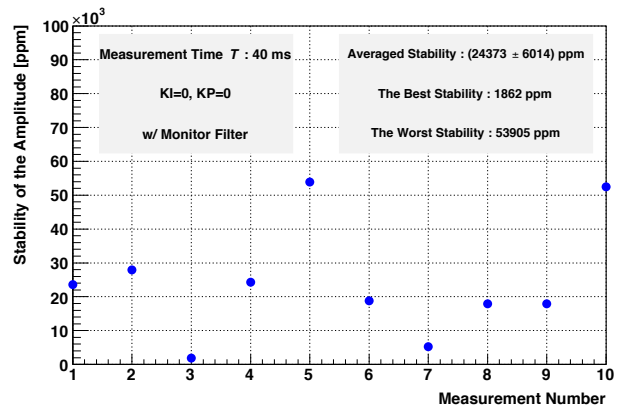
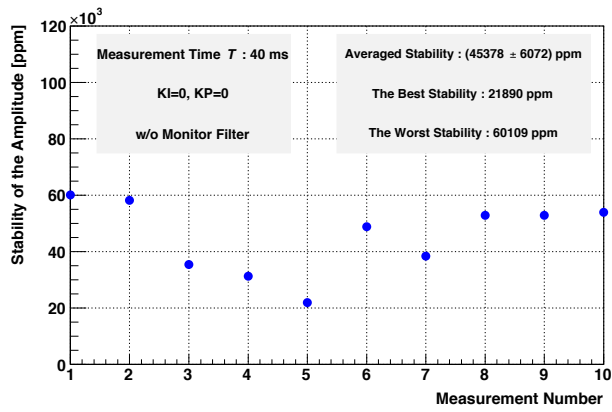
In this order the detailed results will be explained.

### 6.3.1 Single feedback

Here the feedback system functioned only for the  $TM_{020}$  mode. The resonant frequency was 2.59547 GHz. First the stability with no feedback (integral control coefficient KI and proportional control coefficient KP equal to zero) was measured (Figure 6.3). Next KI and KP were increased to see the stabilities (Figure 6.4, 6.5). Table 6.1 summarizes the results of single feedback test, showing the stability of amplitude and phase of the transmitted power  $P_t$ .

Table 6.1: The result of the single feedback.

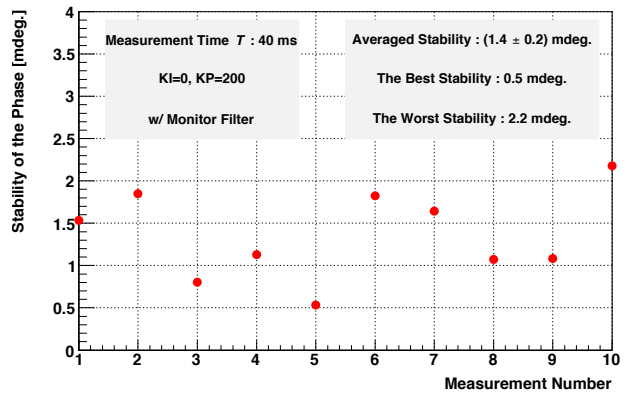
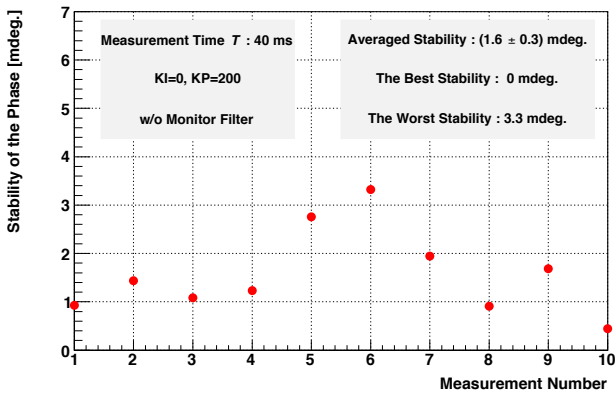
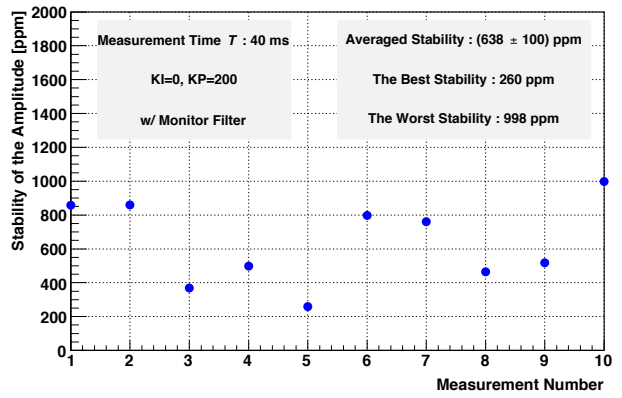
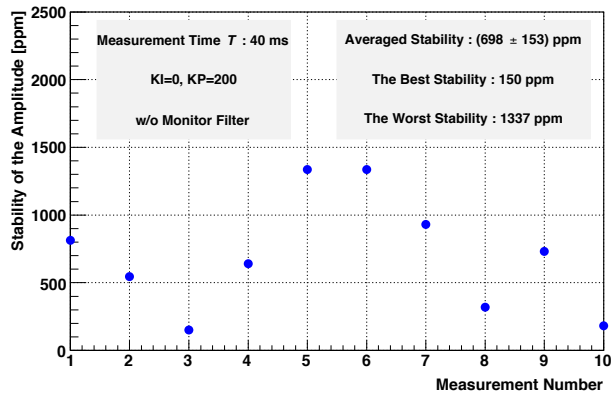
Feedback Constants	Stability of Amplitude	Stability of Phase
KI=0, KP=0	$(2.4 \pm 0.6) \times 10^4$ ppm	$(21 \pm 5)$ mdeg.
KI=0, KP=200	$(6 \pm 1) \times 10^2$ ppm	$(1.4 \pm 0.2)$ mdeg.
KI=2000, KP=200	$(2.2 \pm 0.4) \times 10^2$ ppm	$(0.52 \pm 0.07)$ mdeg.



(a) Without monitor filter

(b) With monitor filter

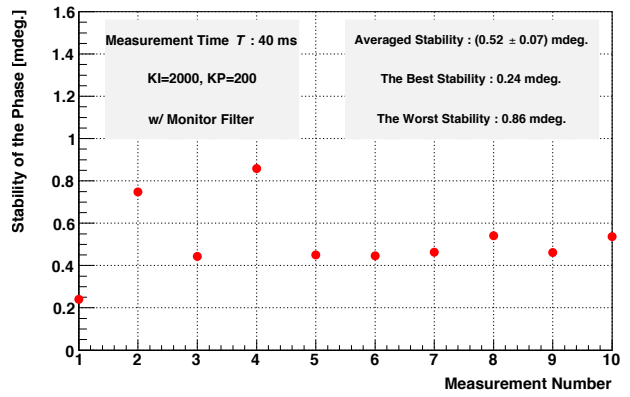
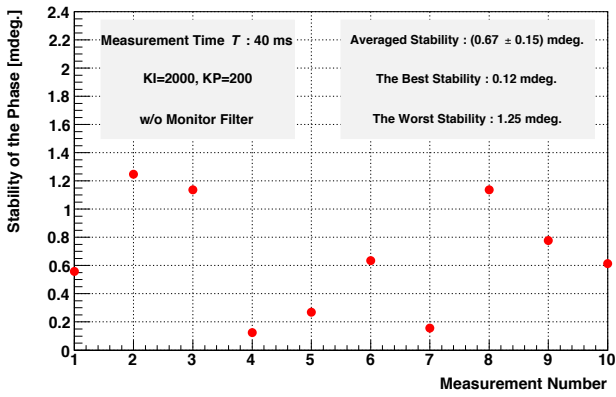
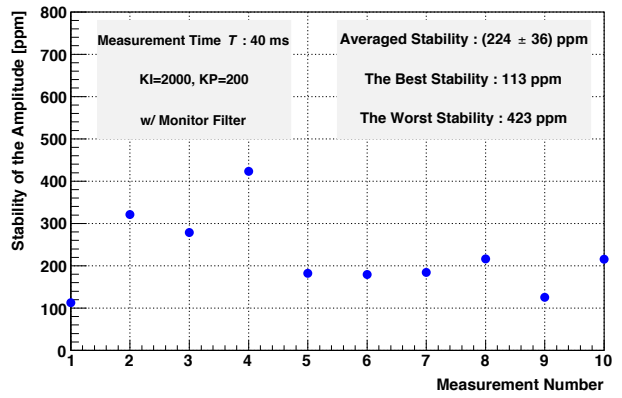
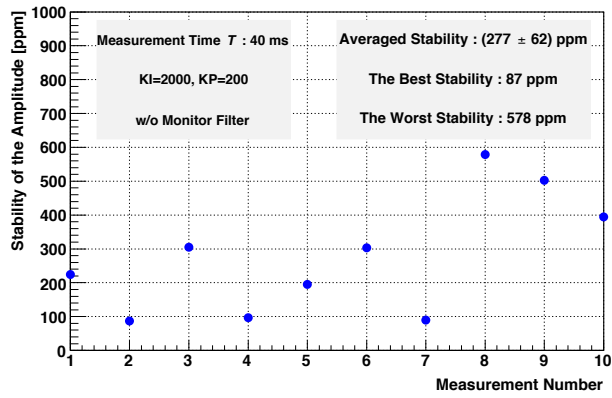
Figure 6.3: The single feedback for the  $TM_{020}$  mode with  $KI=0$ ,  $KP=0$ .



(a) Without monitor filter

(b) With monitor filter

Figure 6.4: The single feedback for the  $TM_{020}$  mode with  $KI=0$ ,  $KP=200$ .



(a) Without monitor filter

(b) With monitor filter

Figure 6.5: The single feedback for the  $TM_{020}$  mode with  $KI=2000$ ,  $KP=200$ .

### 6.3.2 Dual Feedback

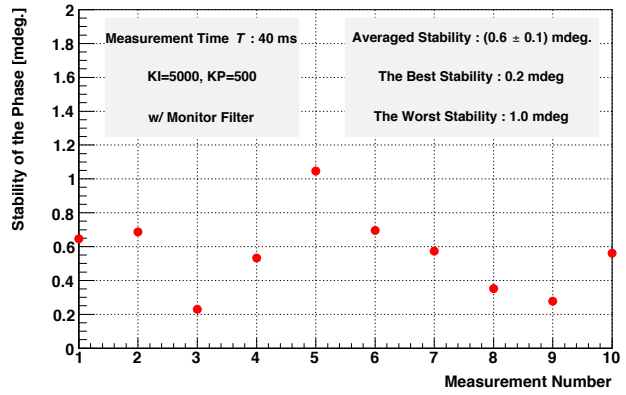
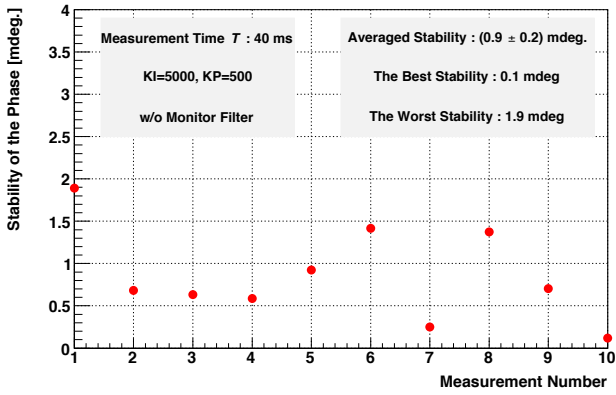
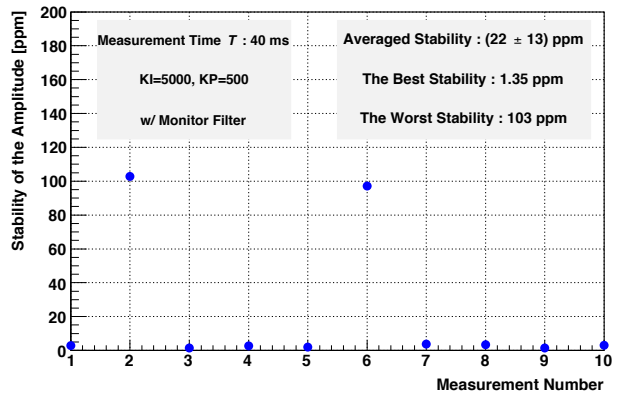
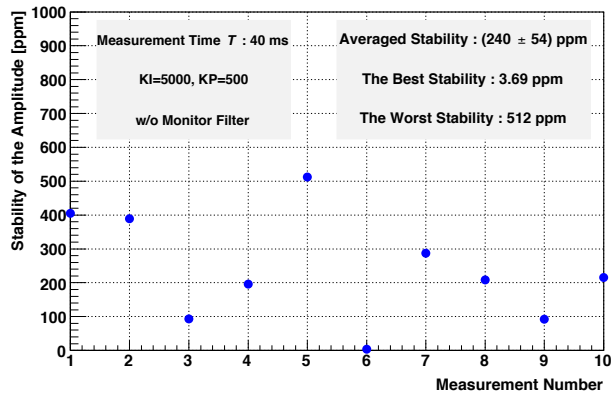
In the dual feedback test, the feedback system functioned for both the  $TM_{010}$  mode and the  $TM_{020}$  mode. KI and KP were set to 5000 and 500 respectively where the deviation of the amplitude and phase were minimized. In this time, the monitor filter and the duration time for the measurement were changed. Figure 6.8 - 6.7 show each result. Table 6.2 and 6.3 summarize the results of dual feedback tests.

Table 6.2: The result of dual feedback for the  $TM_{010}$  mode.

Measurement Time	Monitor Filter	Stability of Amplitude	Stability of Phase
$T=40$ ms	w/o	$(2.4 \pm 0.5) \times 10^2$ ppm	$(0.9 \pm 0.2)$ mdeg.
	w/	$(2 \pm 1) \times 10$ ppm	$(0.6 \pm 0.1)$ mdeg.
$T=50$ $\mu s$	w/o	$(3.4 \pm 0.9) \times 10^2$ ppm	$(0.5 \pm 0.1)$ mdeg.
	w/	$(2.4 \pm 0.6) \times 10$ ppm	$(0.04 \pm 0.01)$ mdeg.

Table 6.3: The result of dual feedback for the  $TM_{020}$  mode.

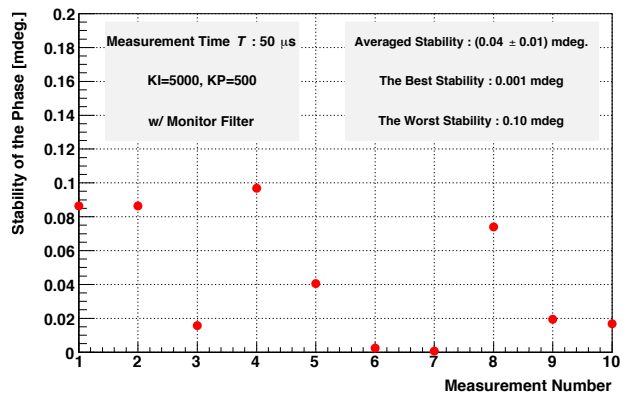
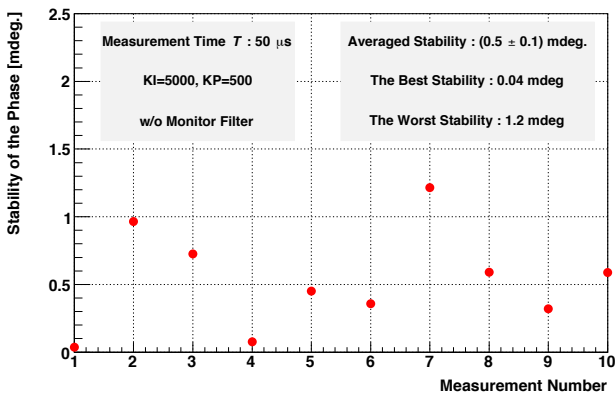
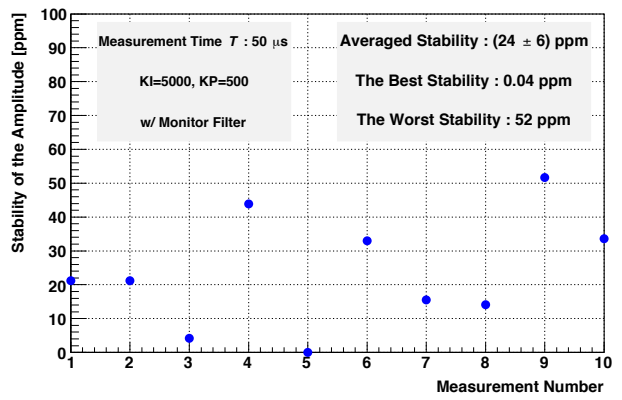
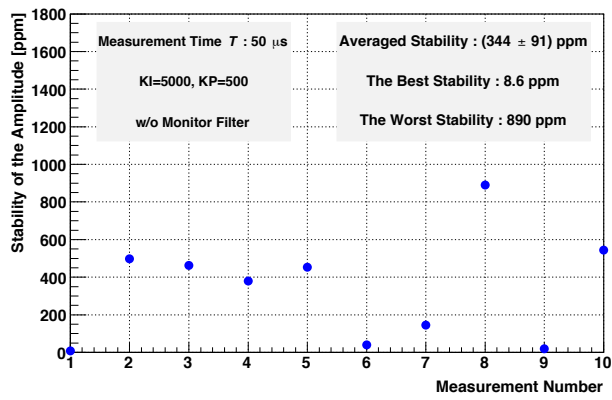
Measurement Time	Monitor Filter	Stability of Amplitude	Stability of Phase
$T=40$ ms	w/o	$(1.0 \pm 0.3) \times 10^2$ ppm	$(0.21 \pm 0.05)$ mdeg.
	w/	$(5 \pm 2) \times 10$ ppm	$(0.06 \pm 0.01)$ mdeg.
$T=50$ $\mu s$	w/o	$(9 \pm 4) \times 10$ ppm	$(0.23 \pm 0.08)$ mdeg.
	w/	$(9 \pm 8)$ ppm	$(0.03 \pm 0.01)$ mdeg.



(a) Without monitor filter

(b) With monitor filter

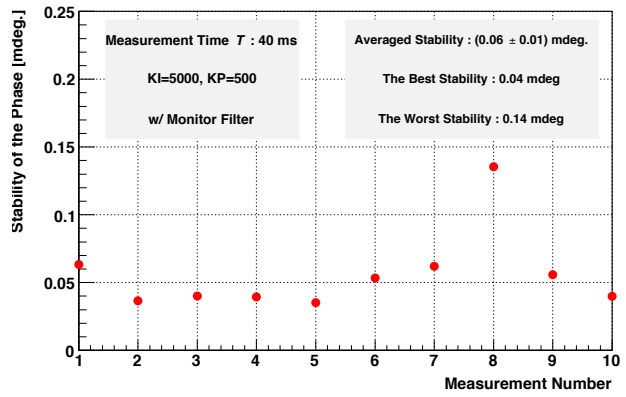
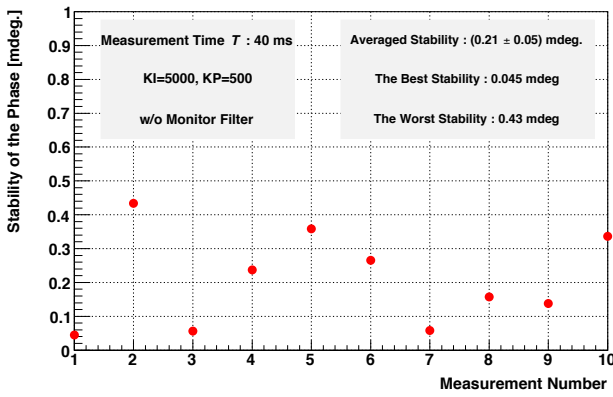
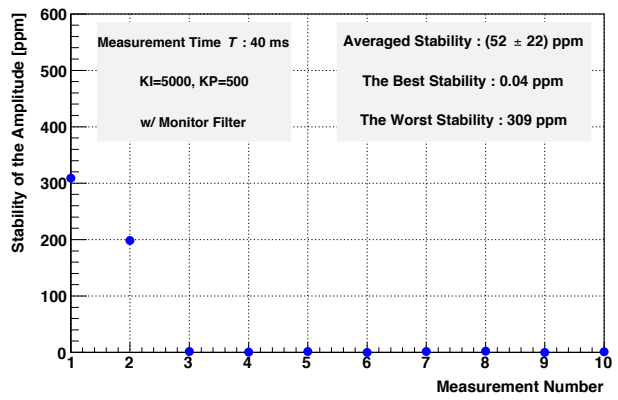
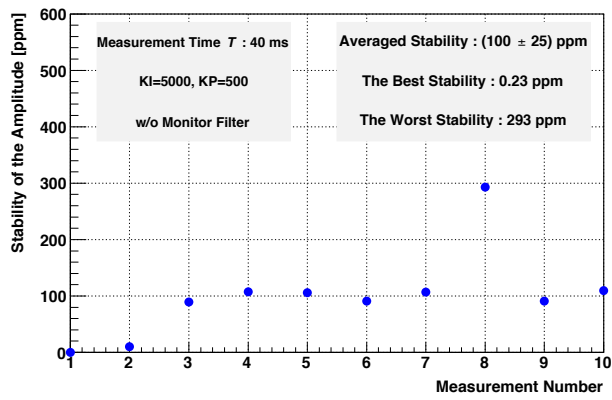
Figure 6.6: The dual feedback for the  $TM_{010}$  mode with  $KI=5000$ ,  $KP=500$  for  $T = 40$  ms.



(a) Without monitor filter

(b) With monitor filter

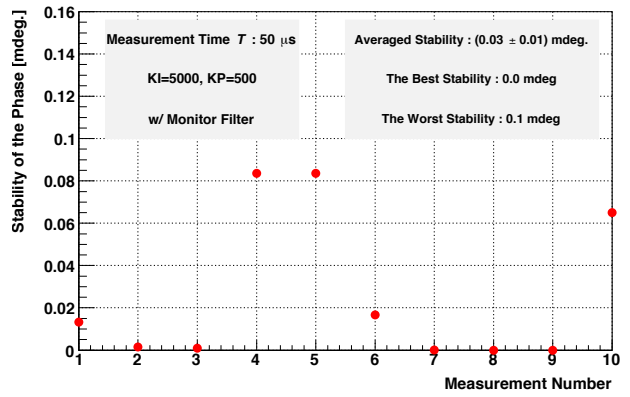
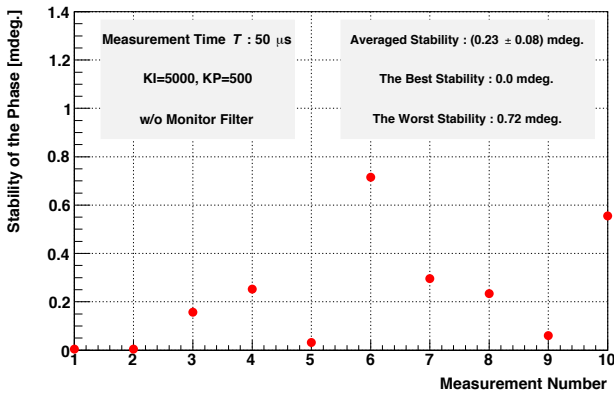
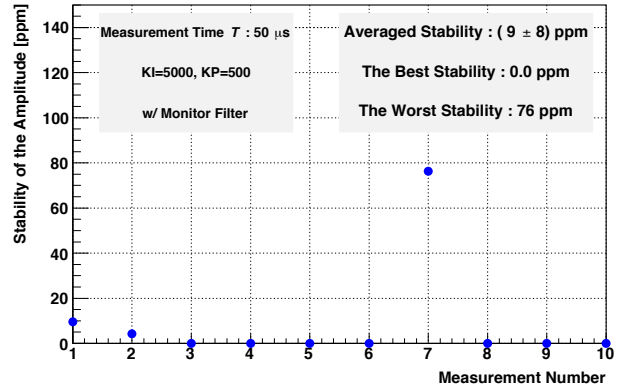
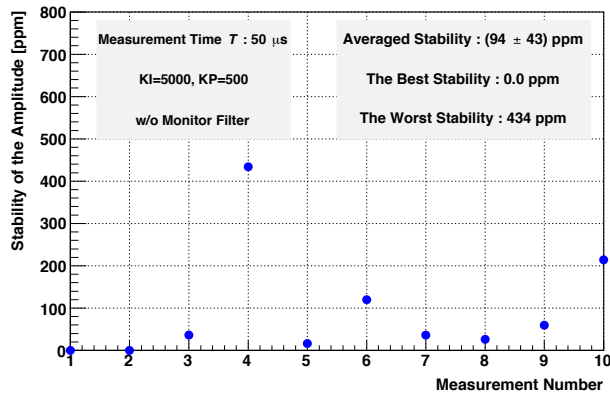
Figure 6.7: The dual feedback for the  $TM_{010}$  mode with  $KI=5000$ ,  $KP=500$  for  $T = 50 \mu s$ .



(a) Without monitor filter

(b) With monitor filter

Figure 6.8: The dual feedback for the  $TM_{020}$  mode with  $KI=5000$ ,  $KP=500$  for  $T = 40$  ms.



(a) Without monitor filter

(b) With monitor filter

Figure 6.9: The dual feedback for the  $TM_{020}$  mode with  $KI=5000$ ,  $KP=500$  for  $T = 50 \mu s$ .

### 6.3.3 Consideration of Ultimate Control Stability

Up to this point, the stabilities are measured at the ADCs in the form of the power in the intermediate frequency;

$$S_{\text{IF}} = A_{\text{IF}} \cos(2\pi f_{\text{IF}}t + \phi_{\text{IF}}) \quad (6.3.1)$$

$$A_{\text{IF}} = aA_{\text{RF}} \quad (6.3.2)$$

$$f_{\text{IF}} = f_{\text{LO}} - f_{\text{RF}} \quad (6.3.3)$$

$$\phi_{\text{IF}} = \phi_{\text{LO}} - \phi_{\text{RF}}. \quad (6.3.4)$$

The form that should be compared with the requirement given by GPT simulations is  $E_{\text{ap}} = E_0 \cos(2\pi f_{\text{RF}}t + \phi_{\text{RF}})$ . In order to convert the stabilities for  $A_{\text{IF}}$  and  $\phi_{\text{IF}}$  into the stabilities for  $E_0$  and  $\phi_{\text{RF}}$ , some steps are made;

- $\Delta A_{\text{IF}}/A_{\text{IF}} \rightarrow \Delta A_{\text{RF}}/A_{\text{RF}} \rightarrow \Delta E_0/E_0$
- $\Delta \phi_{\text{IF}} \rightarrow \Delta \phi_{\text{RF}} \rightarrow \Delta \phi_{\text{ap}}$ .

For the amplitude, under the transformation from  $\Delta A_{\text{IF}}/A_{\text{IF}}$  to  $\Delta A_{\text{RF}}/A_{\text{RF}}$ , the stability does not change because the sinusoidal product-sum transformation in the mixer is performed in a saturated range. The next transformation from  $\Delta A_{\text{RF}}/A_{\text{RF}}$  to  $\Delta E_0/E_0$  uses the following relation;

$$\frac{\Delta E_0}{E_0} = \frac{1}{2} \frac{\Delta A_{\text{RF}}}{A_{\text{RF}}} \quad (6.3.5)$$

from the relation of Eq. (5.3.25).

For the phase,  $\Delta \phi_{\text{IF}}$  includes both  $\Delta \phi_{\text{LO}}$  and  $\Delta \phi_{\text{RF}}$ . Therefore the relation  $\Delta \phi_{\text{IF}} \geq \Delta \phi_{\text{RF}}$  holds. Since  $\Delta \phi_{\text{ap}} = \Delta \phi_{\text{RF}}$ ,  $\Delta \phi_{\text{IF}}$  is a conservative estimate of the stability of phase  $\Delta \phi_{\text{ap}}$ .

From the above consideration, the best results of the dual feedback test are summarized in Table 6.4.

Table 6.4: The result of dual feedback for  $E_{\text{ap}}$ . The measurement time  $T$  is 50  $\mu\text{s}$  and the monitor filter is turned on.

Resonant Mode	Stability of Amplitude	Stability of Phase
TM <sub>010</sub>	(12 $\pm$ 3) ppm	(0.04 $\pm$ 0.01) mdeg.
TM <sub>020</sub>	(5 $\pm$ 4) ppm	(0.03 $\pm$ 0.01) mdeg.

# Chapter 7

## Ultimate Performance of Superconducting-Radio-Frequency Transmission Electron Microscope

In previous chapters, the development of the essential technologies for the superconducting radio frequency transmission electron Microscope (SRF-TEM) was discussed. In this chapter, the performance of each technology is summarized. Then the ultimate performance of the 300 kV SRF-TEM is estimated. After that, the future perspectives for the SRF-TEM are considered. Finally, the achievements in this study is summarized.

### 7.1 Performance Summary of Essential Technology for Superconducting Radio Frequency Transmission Electron Microscope

This section describes the performance of each essential technology for SRF-TEM. The technologies are;

1. The two-mode cavity which realizes low energy dispersion required for the SRF-TEM,
2. The RF feedback system which enables the two-mode cavity to generate stable accelerating fields.

#### 7.1.1 Performance of the Two-mode Cavity

We manufactured two two-mode cavities and performed performance tests twice for each two-mode cavity. The most important performance index determining the spatial resolution of the 300 kV SRF-TEM prototype is the accelerating field  $E_{ap}$ . Table 7.1 summarizes  $E_{ap}$  of both the  $TM_{010}$  mode and the  $TM_{020}$  mode, achieved in the last performance test of the second two-mode cavity. The requirements for  $E_{ap}$  which is calculated in Chapter 4 is also

Table 7.1: The comparison of the requirement and the achievement of  $E_{ap}$ . The requirements is in the case of 300 kV SRF-TEM. The values of the achievement are measured in the last performance test of two-mode cavity manufactured as the second prototype.

	Requirement	Achievement
TM <sub>010</sub>	7.46 MV/m	(11.0 ± 0.3) MV/m
TM <sub>020</sub>	7.20 MV/m	(7.8 ± 0.3) MV/m

Table 7.2: The result of the accelerating field feedback.

		Requirement	Achievement
TM <sub>010</sub>	Amplitude	0.0040 %	(0.0012 ± 0.0003) %
	Phase	150 mdeg.	(0.04 ± 0.01) mdeg.
TM <sub>020</sub>	Amplitude	0.0140 %	(0.0005 ± 0.0004) %
	Phase	55 mdeg.	(0.03 ± 0.01) mdeg.

shown. Table 7.1 indicates that the measured  $E_{ap}$  satisfies the requirements for both the TM<sub>010</sub> mode and the TM<sub>020</sub> mode.

### 7.1.2 Performance of RF Feedback System

The RF feedback system for the two-mode cavity is necessary in order to stabilize the high accelerating fields for minimizing the energy dispersion. Table 7.2 compares the requirements for the stable drive and the achievement of the performance test of the RF feedback system. The requirements are determined in order to achieve the energy dispersion of  $4.0 \times 10^{-5}$  (Chapter 4). The achievement values are the best ones recored in the performance tests. The measurement time is 50  $\mu s$ , that is four times the typical image acquisition time, and the monitor filter is used. Table 7.2 indicates that the developed feedback system satisfies the requirement for the energy dispersion of  $4.0 \times 10^{-5}$ .

Based on the result of the RF feedback test, we can estimate the energy dispersion from Table 7.2 and the relation described in Figure 4.11 - 4.14. The expected value of energy dispersion is  $1.6 \times 10^{-5}$ , a two times better figure than the requirement.

## 7.2 Estimation of Ultimate Performance of 300 kV Superconducting Radio Frequency Transmission Electron Microscope

As described in the previous section, the energy dispersion is estimated as  $1.6 \times 10^{-5}$  from the performance tests for the 300 kV SRF-TEM. This corresponds to the energy spread of 5 eV for the 300 kV SRF-TEM system employing the developed technologies of the two-mode

cavity and the RF feedback system. Using Eq. (3.3.4) and the lens parameters of H-9000 NAR in Table 7.3,  $\Delta'' = 36$  nm is obtained. Figure 7.1 shows a LTF with this value and 15 nm defocus. The spatial resolution reaches the best value of 333 pm.

Table 7.3: Parameters of Hitachi 300 kV TEM H-9000 NAR. The values of  $\sigma(x)$  and  $\beta$  are not published, then values of Hitachi 1.2 MV FE-TEM are used.

$C_3$	0.7 $\mu$ m
$C_c$	1.4 mm
$\Delta J/J$	$1.0 \times 10^{-5}$
$\sigma(x)$	10 pm
$\beta$	0.05 mdeg.

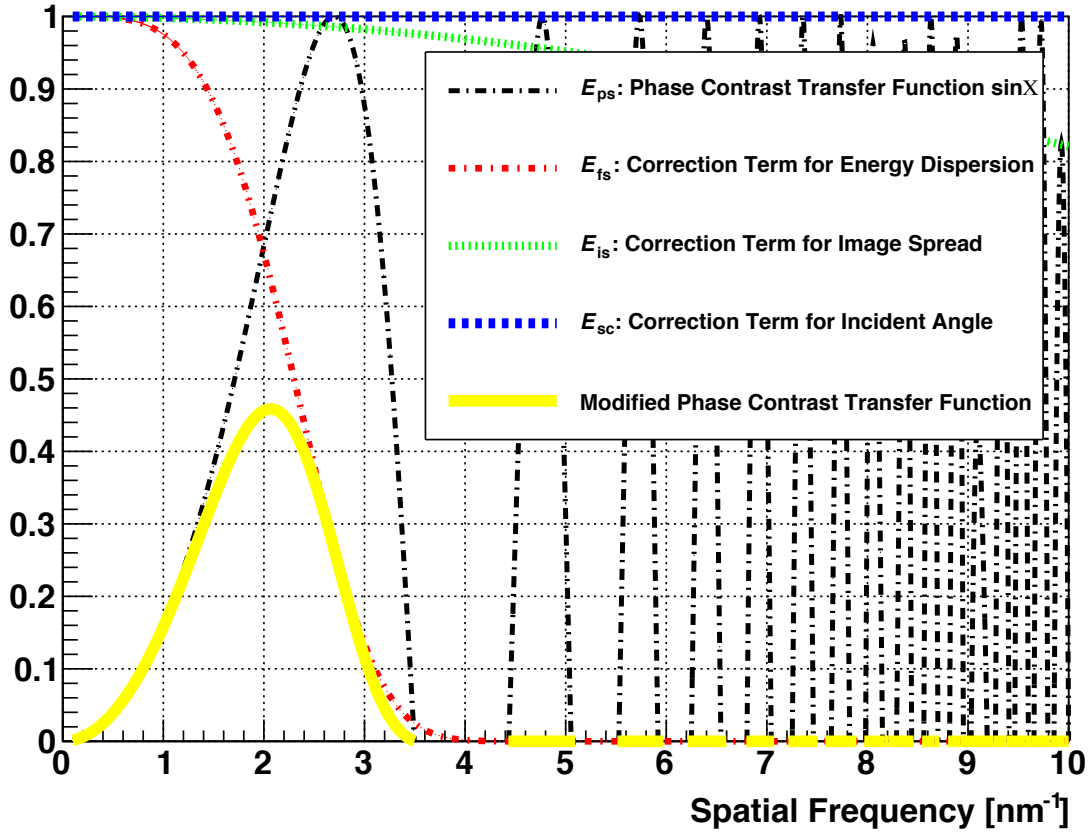


Figure 7.1: The lens transfer function of 300 kV SRF-TEM in the case of  $\Delta'' = 36$  nm and  $\Delta f = 15$  nm. The  $u_{\max}$  is  $3.0 \text{ nm}^{-1}$ , and the resulting spatial resolution is 333 pm.

## 7.3 Future Perspective

This thesis reports the overall system design and the establishment of the essential technologies for the SRF-TEM. This section describes the future perspectives to develop and study the first prototype of the 300 kV SRF-TEM, the 3 MV and 10 MV machines.

### 7.3.1 Fabrication of Cryostat for Two-mode Cavity

The acceleration voltage of the first prototype is 300 kV. Our photocathode gun can accelerate electrons with up to 100 kV. In this situation, we accelerate electrons with 60 kV with this DC gun, and then other 240 kV is given by the two-mode cavity. The accelerating performance of these technologies are already confirmed.

In order to cool the developed two-mode cavity to 4.2 K, we need a cryostat installed into the 300 kV SRF-TEM prototype. The designed performances are summarized in Table 7.4. It is noted that accelerators are usually constructed horizontally, while our SRF-TEM will be assembled vertically. Therefore, the countermeasure against the terrestrial magnetism will be modified compared with the conventional ones.

Table 7.4: The designed performance of the cryostat installed into the 300 kV SRF-TEM prototype.

Operating Temperature	4.2 K
Vacuum Level for Two-mode Cavity	$1.0 \times 10^{-7}$ Pa
Dissipating Power of Two-mode Cavity	17 W
Heat Intrusion	5 W
Volume of Liquid Helium	100 $\ell$
Volume of Liquid Nitrogen	10 $\ell$
Frequency Tuner (Mechanical)	$\pm 2$ MHz (TM <sub>010</sub> mode), $\pm 4$ MHz (TM <sub>020</sub> mode)
Magnetic Shield	up to 20 mG

### 7.3.2 Performance Evaluation of 300 kV SRF-TEM Prototype

After Assembling the 300 kV SRF-TEM prototype, we will conduct the performance evaluation test. This is composed of three processes;

1. Measurement of the energy spread of the beam
2. Measurement of the spatial resolution using an amorphous specimen
3. Observation of each kind of specimens.

The first one indicates the direct measurement of the energy spread  $\Delta T$  using the device called “Electron Energy Loss Spectrometer (EELS)”. Originally, this device is utilized to measure the energy loss at specimens in order to study the characteristics of specimens in TEM observations. In our measurement, we won’t set any specimens, then the genuine energy spread of the beam can be estimated quantitatively.

The second one is the common method to estimate the spatial resolution. The specimen composed of amorphous carbon and gold crystal is utilized (Figure 7.2). Carbons are distributed with a random spacing, then observing the specimen in diffraction mode, a diffraction pattern corresponding to each defocus  $\Delta f$  is acquired, and the reciprocal space distance  $u$  is estimated.  $u_{\max}$ , the maximum value of  $u$  becomes the inverse of the spatial resolution  $\Delta r$  of the machine<sup>1</sup>.

In order to study the performance of the prototype quantitatively, the first and the second measurements are conducted. Additionally, the third test is conducted as the investigation for the practical uses.

With the above, the performance of the 300 kV SRF-TEM prototype will be confirmed.

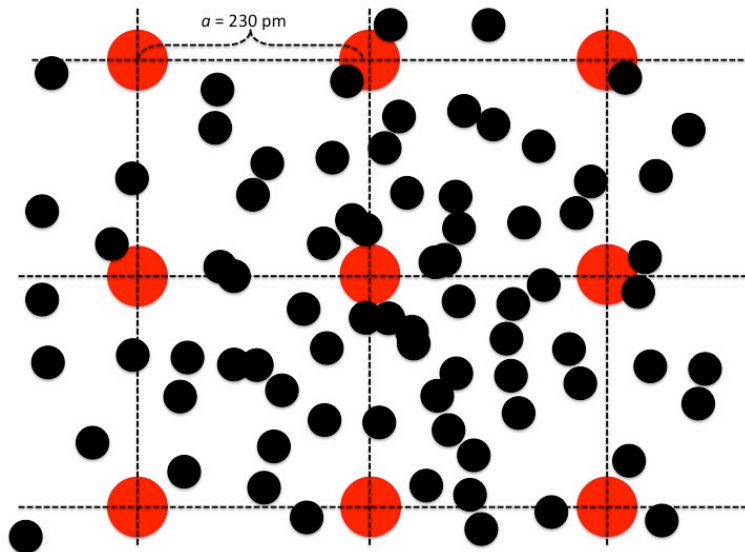


Figure 7.2: The schematic figure of the specimen utilized in the measurement of the spatial resolution  $\Delta r$ . The red circle indicates a gold atom, and the black one indicates a carbon atom. Here, the lattice constant of golds is 230 pm.

### 7.3.3 Future SRF-TEM with Higher Accelerating Voltage than 300 kV

The 300 kV SRF-TEM is the first prototype for the proof-of-principle of the SRF technology application into TEMs. As described in Sec. 3.3.1, the great advantage of the SRF-TEM

<sup>1</sup>To estimate each  $u$ , the lattice constant of gold crystal is used to know the scaling factor of  $u$ .

appears when the accelerating voltage exceeds 3 MV that is the world's highest value at the present moment. Here, tasks for the developments of the future 3 MV and 10 MV SRF-TEMs are summarized.

### **Magnetic Field of Lens**

The magnetic field of the objective lens of a conventional TEM reaches about 2 T. In the case of the higher voltage than 3 MV, the conventional TEM technology cannot handle this situation. The established technology of superconducting magnet utilized in high energy accelerators is expected to realize the strong magnetic field needed for the high energy SRF-TEMs. NbTi is a typical material for superconducting magnet coil. In the Large Hadron Collider (LHC), the dipole magnets with the magnetic field of 8.3 T have been operated[36]. The high energy SRF-TEMs can be realized by replacing the conventional normal conducting magnets with superconducting magnets as well as the accelerating part.

### **Optimization of Two-mode Cavity**

The current two-mode cavity was designed for the acceleration from 60 kV to 300 KV. The gap length of the cavity is too narrow to efficiently accelerate electrons with the energy higher than 300 kV. It is expected that a new design of two-mode cavity with the gap length larger than the current prototype realize a more effective acceleration, and a downsizing of the high energy SRF-TEM.

### **Requirement for RF Feedback Control**

Currently we consider the 4 K operation for the 300 kV SRF-TEM. However, the dissipating power becomes larger for the high energy SRF-TEMs of 3 MV and 10 MV. In order to suppress this, the 2 K operation is effective. However, the RF control is further more difficult for large quality factor  $Q_0$  as seen in Eq. (6.1.3) - (6.1.4). In practical development of high energy SRF-TEMs, it has to be studied whether the 2 K operation or the 4 K operation is appropriate.

## **7.4 Achievement in This Thesis**

We aim to develop a SRF-TEM, the world's first TEM machine employing superconducting RF technologies. This technology is expected to enable TEMs of higher beam energy above 3 MeV, the highest value of the present TEMs. The key is the two-mode accelerating cavity. Very low energy dispersion is required for TEM in order to achieve good spatial resolution. This is not achievable by the conventional RF cavities used for high energy accelerators, but it is possible with the two-mode cavity as proven by the numerical simulation and demonstrated by the tests of prototype cavities. This new type of acceleration scheme is realized by the two-mode cavity of original design employing the superconducting technology. Based on the electric field distribution calculated for the configuration of the prototype two-mode

cavity, an optimization of the overall design of 300 kV SRF-TEM and 3 MV SRF-TEM was performed. The values of electric field and its error margin were used respectively to define the requirements for the two-mode cavity construction and the RF feedback system.

Based on the experiences and knowledge that have been cultivated for high energy accelerators, we established the process to fabricate the two-mode cavity, and conducted the performance tests. This confirms that the developed two-mode cavity satisfies the requirements set by the design optimization of the 300 kV SRF-TEM.

In order to minimize the energy dispersion of electron beam arising from fluctuation of the electric field and the waveform, the operation of the two-mode cavity has to be stabilized. We introduced a RF feedback system. Based on the technology of cERL accelerator, we established the special feedback system dedicated to SRF-TEM, and conducted the performance tests. We confirmed that the developed system satisfies the requirements set by the overall design optimization.

From the above, we established the fundamental technologies for SRF-TEM and pioneered the application of superconducting RF technologies to TEMs with higher energy and good spatial resolution allowing observation of thicker objects than ever, opening a new powerful views for researches in variety of scientific field.



# Appendix A

## Imaging Theory of High-Resolution Transmission Electron Microscope

This part is a supplement for 2.3 to explain the imaging theory in more detail, then there are some overlaps with 2.3.

### A.1 Phase Change by Electrostatic Potential

Phase Contrast Theory uses a wave function to consider a phase change of electron wave by a nucleus. This means that image contrast is generated for to see how the phase of incident electrons' wave functions is altered by nuclei's electrostatic potential.

Generally a refraction index  $n$  is defined by

$$n = \frac{\lambda_1}{\lambda_2}, \quad (\text{A.1.1})$$

where  $\lambda_1$  is a de Broglie wave length of an electron propagating in a space free from any electrostatic potentials of nuclei and  $\lambda_2$  is one in a space in potential  $V$ . Using  $\lambda = h/p$ , Each  $\lambda$  is

$$\lambda_1 = \frac{hc}{\sqrt{2Tm_e c^2 + T^2}} \quad (\text{A.1.2})$$

$$\lambda_2 = \frac{hc}{\sqrt{2(T+eV)m_e c^2 + (T+eV)^2}} \quad (\text{A.1.3})$$

where  $m_e c^2$  is a rest mass of electron equal to 511 keV,  $e$  is elementary charge, equal to  $1.60 \times 10^{-19}$ C. The dependence of de Broglie wave length of a electron on accelerating energy  $T$  is illustrated in Figure A.1.

Substituting Eq.(A.1.2), Eq.(A.1.3) into Eq.(A.1.1) and ignore the second order of  $V$  ( $V \ll E$ ,  $m_e c^2$  is reasonable here), relativistic refraction index  $n_r$  is followed as

$$n_r \cong 1 + \frac{V(m_e c^2 + T)}{E(2m_e c^2 + T)}, \quad (\text{A.1.4})$$

where  $E$  is an accelerating voltage of TEM and  $T = eE$ . Phase change  $\eta$  can be written as

$$\eta = \frac{2\pi}{\lambda}(n - 1)\Delta z \quad (\text{A.1.5})$$

Substituting the equation of relativistic refraction index Eq.(A.1.4), we get relativistic phase change  $\eta_r$  as

$$\eta_r = \frac{2\pi}{\lambda E} \frac{m_e c^2 + T}{2m_e c^2 + T} V(\mathbf{r})\Delta z. \quad (\text{A.1.6})$$

Here a new characteristic "interaction coefficient"  $\sigma_r$  is introduced as  $\sigma_r = 2\pi(m_e c^2 + T)/\lambda E(2m_e c^2 + T)$ , then the wave function for a relativistic phase change satisfies

$$\psi_r(x, y) = \exp \{i\sigma_r V(\mathbf{r})\Delta z\}. \quad (\text{A.1.7})$$

It is usual for TEMs to take the accelerating energy from  $O(100 \text{ kV})$  to  $O(1 \text{ MV})$  therefore  $T \sim O(m_e c^2)$ . Therefore non-relativistic interaction coefficient  $\sigma_c$  comes to  $\pi/\lambda E$  in non-relativistic energy region. A wave function for a non-relativistic phase change can be defined as

$$\psi_c(x, y) = \exp \{i\sigma_c V(\mathbf{r})\Delta z\}. \quad (\text{A.1.8})$$

An interaction coefficient  $\sigma_r$  decides how much an electrostatic potential in a specimen contributes to a phase change and in higher energy region, it gets smaller and comes closer to

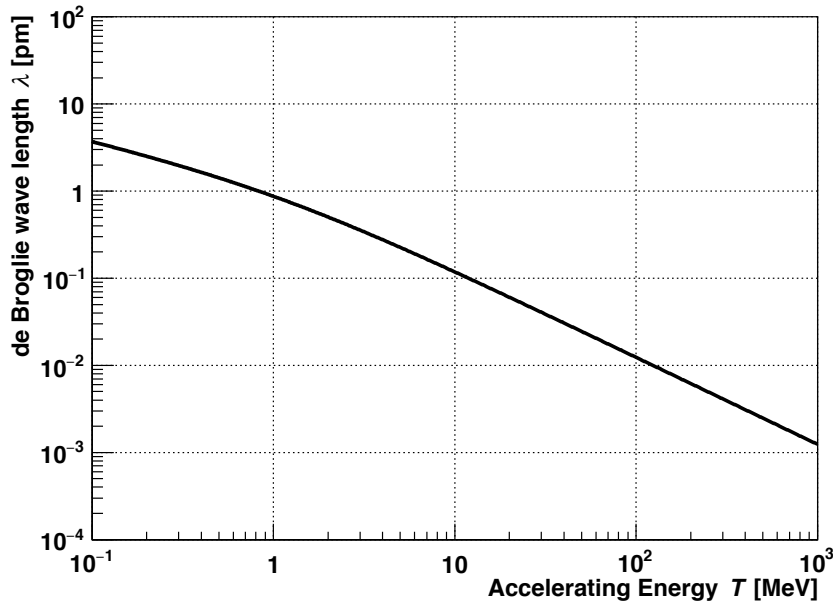


Figure A.1: de Broglie wave length varying along with the accelerating energy  $T$ .

$2\pi e/hc$  (see Figure A.2). For example,  $\sigma_{100 \text{ kV}}$ , the interaction coefficient in the accelerating voltage of 100 kV can be compared with one in 10 MV,  $\sigma_{10 \text{ MV}}$ . Then,

$$\frac{\sigma_{10 \text{ MV}}}{\sigma_{100 \text{ kV}}} = \frac{8.13 \times 10^{-13} \text{m}^{-1} \text{eV}^{-1}}{1.48 \times 10^{-12} \text{m}^{-1} \text{eV}^{-1}} \simeq 0.55. \quad (\text{A.1.9})$$

This means that TEMs with 10 MV accelerating voltage has a half of ability to transfer electrostatic potentials in a specimen to a phase change compared with that of 100 kV TEM.

Incoming electrons pass through a specimen feeling a potential  $V(\mathbf{r})$ , then coming to an objective lens.  $\eta_{\text{net}}$ , the net path difference generated by potentials  $V(\mathbf{r})$  in a specimen is calculated as

$$\eta_{\text{net}} = \sigma_r \int V(\mathbf{r}) dz = \sigma_r \int V(x, y, z) dz = \sigma_r V_p(x, y), \quad (\text{A.1.10})$$

where  $V_p(x, y)$  is called as a projection potential which is integrated all potentials belong beam axis. Here  $\eta_{\text{net}} \ll 1$ , then the phase wave function  $\psi_i$  can be approximated like

$$\psi_i = \exp(i\sigma V_p) \quad (\text{A.1.11})$$

$$= \exp(i\eta_{\text{net}}) \quad (\text{A.1.12})$$

$$= 1 + i\eta_{\text{net}}. \quad (\text{A.1.13})$$

The image intensity  $I$  can be determine by  $I = \psi_i^* \psi_i$ , however  $\eta_{\text{net}} \ll 1$  works here then the

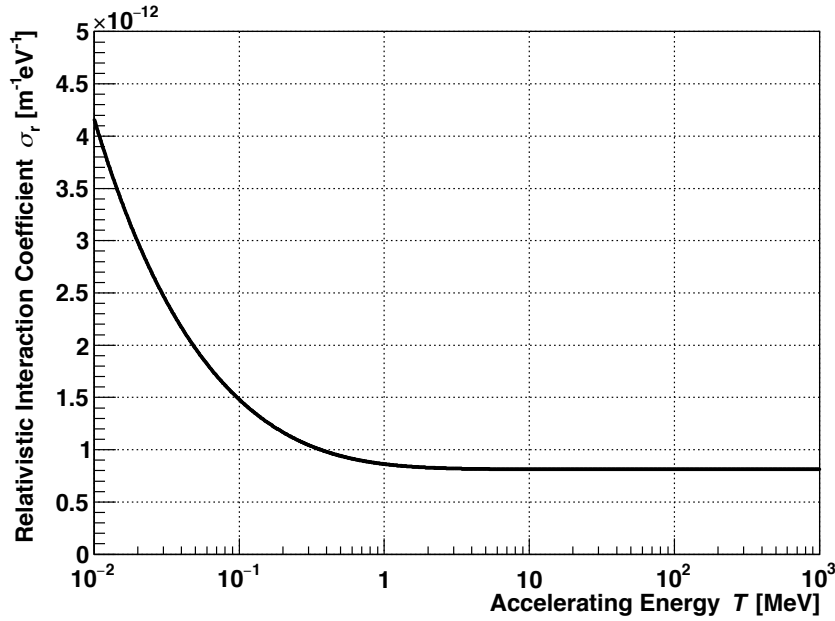


Figure A.2: Variation of Interaction Coefficient  $\sigma$  When Accelerating Voltage Is Changed.

higher order larger including the second order of  $\eta_{\text{net}}$  should be ignored, then

$$I = \psi_i^* \psi_i \quad (\text{A.1.14})$$

$$= (1 - i\eta_{\text{net}})(1 + i\eta_{\text{net}}) \quad (\text{A.1.15})$$

$$= 1, \quad (\text{A.1.16})$$

which means the image has no contrast.

## A.2 Phase Shift at Objective Lens

Here the effect of the phase shift by the objective lens shall be considered then it can be explained that in practice TEMs can get a contrast images. The wave function that corresponds to the phase shift by the objective lens is called “Lens Transfer Function (LTF)”, and is expressed as

$$\text{LTF} = \exp(-i\chi_{\text{ps}}) \exp(\chi_{\text{fs}}) \exp(\chi_{\text{is}}) \exp(\chi_{\text{sc}}) \quad (\text{A.2.1})$$

$$\chi_{\text{ps}} = \frac{\pi}{2} C_3 \lambda^3 u^4 + \frac{\pi}{3} C_5 \lambda^5 u^6 + \pi \Delta f \lambda u^2 \quad (\text{A.2.2})$$

$$\chi_{\text{fs}} = -\frac{\pi^2}{2} \lambda^2 \Delta^2 u^4 \quad (\text{A.2.3})$$

$$\chi_{\text{is}} = -2\pi^2 \sigma^2(x) u^2 \quad (\text{A.2.4})$$

$$\chi_{\text{sc}} = -\pi^2 u_0^2 \{ (C_3 \lambda^2 u^2 + \Delta f) \lambda u \}^2, \quad (\text{A.2.5})$$

where the notations were explained before in 2.3.

The phase wave function  $\psi_i$  in Eq. (A.1.13) is modified as

$$\psi_i = 1 + i\sigma V_p \otimes \hat{F} [\text{LTF}] \quad (\text{A.2.6})$$

$$= 1 + i\sigma V_p \otimes \hat{F} [\exp(-i\chi_{\text{ps}} + \chi_{\text{fs}} + \chi_{\text{is}} + \chi_{\text{sc}})] \quad (\text{A.2.7})$$

$$= 1 + i\sigma V_p \otimes \hat{F} [\exp(-i\chi_{\text{ps}} + \chi_{\text{R}})], \quad (\text{A.2.8})$$

where  $\otimes$  represents convolution,  $\hat{F}$  stands for inverse Fourier transformation and replaced  $\chi_{\text{fs}} + \chi_{\text{is}} + \chi_{\text{sc}}$  with  $\chi_{\text{R}}$ . Then the image intensity  $I$  becomes

$$I = \left\{ 1 + i\sigma V_p \otimes \hat{F} [\exp(-i\chi_{\text{ps}} + \chi_{\text{R}})] \right\} \left\{ 1 - i\sigma V_p \otimes \hat{F} [\exp(+i\chi_{\text{ps}} + \chi_{\text{R}})] \right\} \quad (\text{A.2.9})$$

$$= 1 - i\sigma V_p \otimes \hat{F} [\exp(i\chi_{\text{ps}} + \chi_{\text{R}})] + i\sigma V_p \otimes \hat{F} [\exp(-i\chi_{\text{ps}} + \chi_{\text{R}})] \quad (\text{A.2.10})$$

$$= 1 + 2\sigma V_p \otimes \hat{F} [\sin(\chi_{\text{ps}}) \cdot \exp(\chi_{\text{R}})] \quad (\text{A.2.11})$$

$$= 1 + 2\sigma V_p \otimes \hat{F} [\sin(\chi_{\text{ps}}) \cdot \exp(\chi_{\text{fs}} + \chi_{\text{is}} + \chi_{\text{sc}})]. \quad (\text{A.2.12})$$

# Appendix B

## Response Calculation of Superconducting Cavity by Lumped-constant Circuit Modeling

It is useful that superconducting cavities are modeled as lumped-constant circuit in order to consider the operation. This description is based on [37].

### B.1 Relation Between Cavity and Coupler

Figure B.1 shows the lumped-constant circuit model of the two-mode cavity and the power transmission lines. The left part represents the power source including the reflection power. The right part represents the transmitted power. The resistance  $R_c$ , the coil  $L_c$  and the capacitor  $C_c$  represents the two-mode cavity. The Voltage  $V_{in}$  and the current  $I_{in}$  travel from the RF source  $G$  to the cavity, and the Voltage  $V_r$  and the current  $I_r$  comes back to the source of  $G$ , reflected at the cavity.  $z_0$  represents the characteristic impedance of the transmitted lines. The Voltage  $V_t$ , the current  $I_t$  and the power  $P_t$  travel from cavity to an external circuit.  $I_{in}$  and  $I_{c1}$  indicates currents flowing at a voltage transformer that represents the

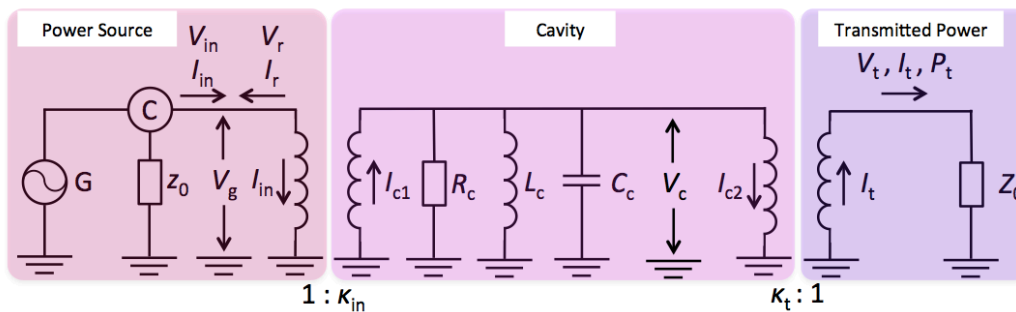


Figure B.1: The lumped-constant circuit model of the two-mode cavity.

input power coupler whose coupling ratio is  $1 : \kappa_{\text{in}}$ . Similarly,  $I_t$  and  $I_{c2}$  indicates currents flowing at a voltage transformer that represents the output power coupler whose coupling ratio is  $1 : \kappa_t$ . The Voltage of  $V_g$  represents the voltage of the power source, and the voltage of  $V_c$  represents the cavity voltage.

One relation is established among the input voltage  $V_{\text{in}}$ , the reflection voltage  $V_r$  and the power source voltage  $V_g$  as

$$V_g = V_{\text{in}} + V_r. \quad (\text{B.1.1})$$

Additionally,

$$V_{\text{in}} = z_0 I_{\text{in}} \quad (\text{B.1.2})$$

$$V_r = z_0 I_r \quad (\text{B.1.3})$$

$$I_g = I_{\text{in}} - I_r \quad (\text{B.1.4})$$

are established. Therefore,

$$V_{\text{in}} - V_r = z_0 I_g \quad (\text{B.1.5})$$

is derived. Using  $V_{\text{in}}$  and  $V_r$ , the cavity voltage  $V_c$  and the coupling current  $I_{c1}$  can be expressed as

$$V_c = \kappa_{\text{in}} V_g = \kappa_{\text{in}} (V_{\text{in}} + V_r) \quad (\text{B.1.6})$$

$$I_{c1} = \frac{I_g}{\kappa_{\text{in}}} = \frac{1}{\kappa_{\text{in}} z_0} (V_{\text{in}} - V_r). \quad (\text{B.1.7})$$

Using the above equations,

$$I_{c1} = -\frac{V_c}{\kappa_{\text{in}}^2 z_0} + \frac{2V_{\text{in}}}{\kappa_{\text{in}} z_0} \quad (\text{B.1.8})$$

$$V_r = \frac{V_c}{\kappa_{\text{in}}} - V_{\text{in}} \quad (\text{B.1.9})$$

are established. Similarly, the voltage  $V_t$  and the current  $I_{c2}$  are expressed as

$$V_t = z_0 I_t \quad (\text{B.1.10})$$

$$V_c = \kappa_t V_t \quad (\text{B.1.11})$$

$$I_{c2} = -\frac{I_t}{\kappa_t}, \quad (\text{B.1.12})$$

then,

$$I_{c2} = -\frac{V_c}{\kappa_t^2 z_0} \quad (\text{B.1.13})$$

$$(\text{B.1.14})$$

is derived. Each power has a relation with its corresponding voltage as

$$P_{\text{in}} = \frac{1}{2z_0} |V_{\text{in}}|^2 \quad (\text{B.1.15})$$

$$P_{\text{r}} = \frac{1}{2z_0} |V_{\text{r}}|^2 \quad (\text{B.1.16})$$

$$P_{\text{t}} = \frac{1}{2z_0} |V_{\text{t}}|^2 \quad (\text{B.1.17})$$

$$P_{\text{c}} = \frac{1}{2R_{\text{c}}} |V_{\text{c}}|^2. \quad (\text{B.1.18})$$

## B.2 Differential Equation for Superconducting Cavity and General Solution

Considering Kirchhoff's circuit law for the cavity,

$$C_{\text{c}} \frac{d}{dt} V_{\text{c}} + \frac{1}{R_{\text{c}}} + \frac{1}{L_{\text{c}}} \int V_{\text{c}} dt = I_{\text{c1}} + I_{\text{c2}} \quad (\text{B.2.1})$$

is established. Substituting Eq. (B.1.8) and (B.1.13) into the above equation and taking a temporal differentiation,

$$\frac{d^2}{dt^2} V_{\text{c}} + 2\lambda^* \frac{d}{dt} V_{\text{c}} + \omega_0^2 V_{\text{c}} = \frac{d}{dt} \left( \frac{2V_{\text{in}}}{\kappa_{\text{in}} z_0 C_{\text{c}}} \right) \quad (\text{B.2.2})$$

$$2\lambda^* = \frac{1}{R_{\text{c}} C_{\text{c}}} \frac{1}{\kappa_{\text{in}}^2 z_0 C_{\text{c}}} + \frac{1}{\kappa_{\text{t}}^2 z_0 C_{\text{c}}} \quad (\text{B.2.3})$$

$$\omega_0^2 = \frac{1}{L_{\text{c}} C_{\text{c}}} \quad (\text{B.2.4})$$

are derived, where  $\omega_0$  is the resonant angular frequency of the superconducting cavity. As explained in Sec. 5.1.3, the quality factor  $Q_0$  is written as

$$Q_0 = \frac{\omega_0 U}{P_{\text{c}}}, \quad (\text{B.2.5})$$

and the stored energy  $U$  is described as

$$U = \frac{1}{2} C_{\text{c}} V_{\text{c}}^2 \quad (\text{B.2.6})$$

$$= \frac{1}{2} L_{\text{c}} I_{\text{c}}^2, \quad (\text{B.2.7})$$

then substituting Eq. (B.1.18) in place of  $P_{\text{c}}$ , the quality factor is expressed as

$$Q_0 = \sqrt{\frac{C_{\text{c}}}{L_{\text{c}}}} R_{\text{c}}. \quad (\text{B.2.8})$$

The shunt impedance of the cavity  $R_a$  is defined as

$$R_a = \frac{V_c}{P_c}. \quad (\text{B.2.9})$$

Substituting Eq. (B.1.18),  $R_a$  is written as

$$R_a = 2R_c. \quad (\text{B.2.10})$$

Additionally, new parameters are introduced as

$$\beta_{\text{in}} = \frac{R_c}{\kappa_{\text{in}}^2 z_0} \quad (\text{B.2.11})$$

$$\beta_{\text{t}} = \frac{R_c}{\kappa_{\text{t}}^2 z_0}. \quad (\text{B.2.12})$$

Theses are determined by the coupling strength of  $\kappa_{\text{in}}$  and  $\kappa_{\text{t}}$ . The loaded quality factor  $Q_L$  is expressed as

$$\frac{1}{Q_L} = \frac{1}{Q_0} (1 + \beta_{\text{in}} + \beta_{\text{t}}) \quad (\text{B.2.13})$$

$$= \frac{1}{Q_0} (1 + \beta^*). \quad (\text{B.2.14})$$

Then,

$$2\lambda^* = \frac{1}{R_c C_c} + \frac{1}{\kappa_{\text{in}}^2 z_0 C_c} + \frac{1}{\kappa_{\text{t}}^2 z_0 C_c} \quad (\text{B.2.15})$$

$$= \frac{1}{R_c C_c} \left( 1 + \frac{R_c}{\kappa_{\text{in}}^2 z_0} + \frac{R_c}{\kappa_{\text{t}}^2 z_0} \right) \quad (\text{B.2.16})$$

$$= \frac{\omega_0}{Q_0} (1 + \beta_{\text{in}} + \beta_{\text{t}}) \quad (\text{B.2.17})$$

$$= \frac{\omega_0}{Q_0} (1 + \beta^*) \quad (\text{B.2.18})$$

$$= \frac{\omega_0}{Q_L}. \quad (\text{B.2.19})$$

Eq. (B.1.9) and (B.2.2) are expressed using  $\beta^*$  and  $R_a$  as

$$V_r = \sqrt{\frac{2\beta^* z_0}{R_a}} V_c - V_{\text{in}} \quad (\text{B.2.20})$$

$$\frac{d^2}{dt^2} V_c + 2\lambda^* \frac{d}{dt} V_c + \omega_0^2 V_c = 2\lambda^* \frac{2\sqrt{\beta^*}}{1 + \beta^*} \sqrt{\frac{R_a}{2z_0}} \frac{d}{dt} V_{\text{in}}. \quad (\text{B.2.21})$$

Eq. (B.2.21) is rewritten as a general form like

$$\frac{d^2}{dt^2} V_c + 2\lambda^* \frac{d}{dt} V_c + \omega_0^2 V_c = \frac{d}{dt} f(t) \quad (\text{B.2.22})$$

and its general solution  $V_f$  is

$$V_f = C_+ e^{-\lambda_+ t} + C_- e^{-\lambda_- t} + \frac{1}{\lambda_+ - \lambda_-} \int_{-\infty}^t \{\lambda_+ e^{-\lambda_+(t-t')} - \lambda_- e^{-\lambda_-(t-t')}\} f(t') dt' \quad (\text{B.2.23})$$

$$\lambda_{\pm} = \lambda^* \pm \sqrt{\lambda^{*2} - \omega_0^2} \quad (\text{B.2.24})$$

where  $C_{\pm}$  are the constants determined by the initial conditions. In the case of superconducting cavities,  $\lambda^* \ll \omega_0$ , then the above equations are rewritten as

$$V_f \simeq C_+ e^{-\lambda_+ t} + C_- e^{-\lambda_- t} + \frac{1}{2} \int_{-\infty}^t \{e^{-\lambda_+(t-t')} + e^{-\lambda_-(t-t')}\} f(t') dt' \quad (\text{B.2.25})$$

$$\lambda_{\pm} = \lambda^* \pm i\omega_0. \quad (\text{B.2.26})$$

### B.3 Stationary State of Superconducting Cavity

To satisfy Eq. (B.1.15), the input voltage is defined as

$$V_{\text{in}} = \sqrt{2z_0 P_{\text{in}}} e^{i\omega t} \quad (\text{B.3.1})$$

where  $\omega$  is the angular frequency of the signal generator, and  $\omega - \omega_0$  is finite. In order to acquire the stationary solution for Eq. (B.2.25), setting  $C_{\pm} = 0$ , and substituting Eq. (B.3.1) in place of  $f(t')$  in Eq. (B.2.25),

$$V_c \simeq \frac{2\sqrt{\beta^*}}{1 + \beta^*} \sqrt{R_a P_{\text{in}}} \times \int_{-\infty}^t \left( \lambda^* e^{-\lambda_+(t-t')} + \lambda^* e^{-\lambda_-(t-t')} \right) e^{i\omega t'} dt' \quad (\text{B.3.2})$$

is derived. Setting the integrand  $G^{\pm}(t)$  as

$$G^{\pm}(t) = \int_{-\infty}^t \lambda^* e^{-\lambda_{\pm}(t-t')} e^{i\omega t'} dt', \quad (\text{B.3.3})$$

and substituting Eq. (B.2.19) in place of  $\lambda^*$ ,

$$G^{\pm}(t) = \frac{\lambda^*}{\lambda^* + i(\omega \pm \omega_0)} e^{i\omega t} \quad (\text{B.3.4})$$

$$= \frac{1}{1 + 2iQ_L} \frac{\omega \pm \omega_0}{\omega_0} e^{i\omega t}. \quad (\text{B.3.5})$$

In the case of Superconducting cavities,  $Q_L \gg 1$  and  $\omega \simeq \omega_0$ , then  $|G^+(t)| \ll |G^-(t)|$  is established. Therefore, ignoring  $G^+(t)$ , Eq. (B.3.2) is rewritten as

$$V_c \simeq \frac{2\sqrt{\beta^*}}{1 + \beta^*} \sqrt{R_a P_{\text{in}}} \frac{1}{1 + 2iQ_L} \frac{\omega - \omega_0}{\omega_0} e^{i\omega t} \quad (\text{B.3.6})$$

$$= \frac{2\sqrt{\beta^*}}{1 + \beta^*} \sqrt{R_a P_{\text{in}}} \frac{1}{1 - i \tan \theta} e^{i\omega t} \quad (\text{B.3.7})$$

$$= \frac{2\sqrt{\beta^*}}{1 + \beta^*} \sqrt{R_a P_{\text{in}}} \cos \theta e^{i(\omega t + \theta)} \quad (\text{B.3.8})$$

$$\tan \theta = -2Q_L \frac{\omega - \omega_0}{\omega_0}. \quad (\text{B.3.9})$$

This  $\theta$  is called as “ tuning angle ”.

Substituting Eq. (B.3.8) in place of  $V_c$  and Eq. (B.3.1) in place of  $V_{\text{in}}$  in Eq. (B.2.20) respectively, the reflection voltage  $V_r$  in stationary states is calculated as

$$V_r = \sqrt{2z_0 P_{\text{in}}} \left( \frac{2\beta^*}{1 + \beta^*} \cos \theta e^{i\theta} - 1 \right) e^{i\omega t} \quad (\text{B.3.10})$$

$$= \sqrt{2z_0 P_{\text{in}}} \frac{\beta^* e^{i2\theta} - 1}{1 + \beta^*} e^{i\omega t}. \quad (\text{B.3.11})$$

Using Eq. (B.1.16) and (B.3.11), the reflection power  $P_r$  is calculated as

$$P_r = \left| \frac{\beta^* e^{i2\theta} - 1}{1 + \beta^*} \right|^2 P_{\text{in}} \quad (\text{B.3.12})$$

$$= \frac{1 - 2\beta^* \cos 2\theta + \beta^{*2}}{(1 + \beta^*)^2} P_{\text{in}}. \quad (\text{B.3.13})$$

When  $\omega = \omega_0$  ( $\theta = 0$ ),

$$P_r = \left( \frac{1 - \beta^*}{1 + \beta^*} \right)^2 P_{\text{in}} \quad (\text{B.3.14})$$

is established, and when  $\omega \neq \omega_0$ ,  $P_r$  gets the minimum value

$$P_r = \sin^2 \theta P_{\text{in}} \quad (\text{B.3.15})$$

at  $\beta^* = 1$ . Our two-mode cavity was manufactured to satisfy  $\beta^* = 1$  in order to minimize the reflection power. Similar, from Eq. (B.1.18), (B.2.10) and (B.3.8), the dissipating power  $P_c$  in stationary states is calculated as

$$P_c = \frac{4\beta^* \cos^2 \theta}{(1 + \beta^*)^2} P_{\text{in}}. \quad (\text{B.3.16})$$

From Eq. (B.1.11), (B.1.17) and (B.3.8), the transmitted power  $P_t$  is calculated as

$$P_t = \frac{4\beta^* \beta_t \cos^2 \theta}{(1 + \beta^*)^2} P_{\text{in}}. \quad (\text{B.3.17})$$

## B.4 Response to Pulsed Power

Here, it is considered that the input power is pulsed. Owing to monitor the response of the cavity to the pulsed input power,  $\beta^*$ ,  $Q_L$ ,  $\beta_{\text{in}}$  and  $\beta_t$  can be estimated. The indices of  $\beta_{\text{in}}$  and  $\beta_t$  can be considered stable, then the transition of  $Q_0$  and  $V_c$  can be estimated with only once measurement of the pulsed input power.

Now, considering the situation of  $\omega = \omega_0$ . when  $t = 0$ , the switch of the input power turns on, and when  $t = t_{\text{off}}$ , the switch turns off. The amplitude of the input power is considered constant (Figure B.2). Given the initial condition of  $V_c = 0$ ,  $dV_c/dt = 0$  at  $t = 0$ , Eq. (B.2.25) becomes

$$V_c(t) \simeq \frac{2\sqrt{\beta^*}}{1 + \beta^*} \sqrt{R_a P_{\text{in}}} (1 - e^{-\lambda^* t}) e^{i\omega_0 t} \quad (0 \leq t < t_{\text{off}}). \quad (\text{B.4.1})$$

From Eq. (B.2.20), (B.3.1) and (B.4.1),

$$V_r(t) = \sqrt{2z_0 P_{\text{in}}} \left( \frac{2\beta^*}{1 + \beta^*} (1 - e^{-\lambda^* t}) - 1 \right) e^{i\omega_0 t} \quad (\text{B.4.2})$$

$$= -\sqrt{2z_0 P_{\text{in}}} \frac{1 - \beta^* + 2\beta^* e^{-\lambda^* t}}{1 + \beta^*} e^{i\omega_0 t} \quad (0 \leq t < t_{\text{off}}). \quad (\text{B.4.3})$$

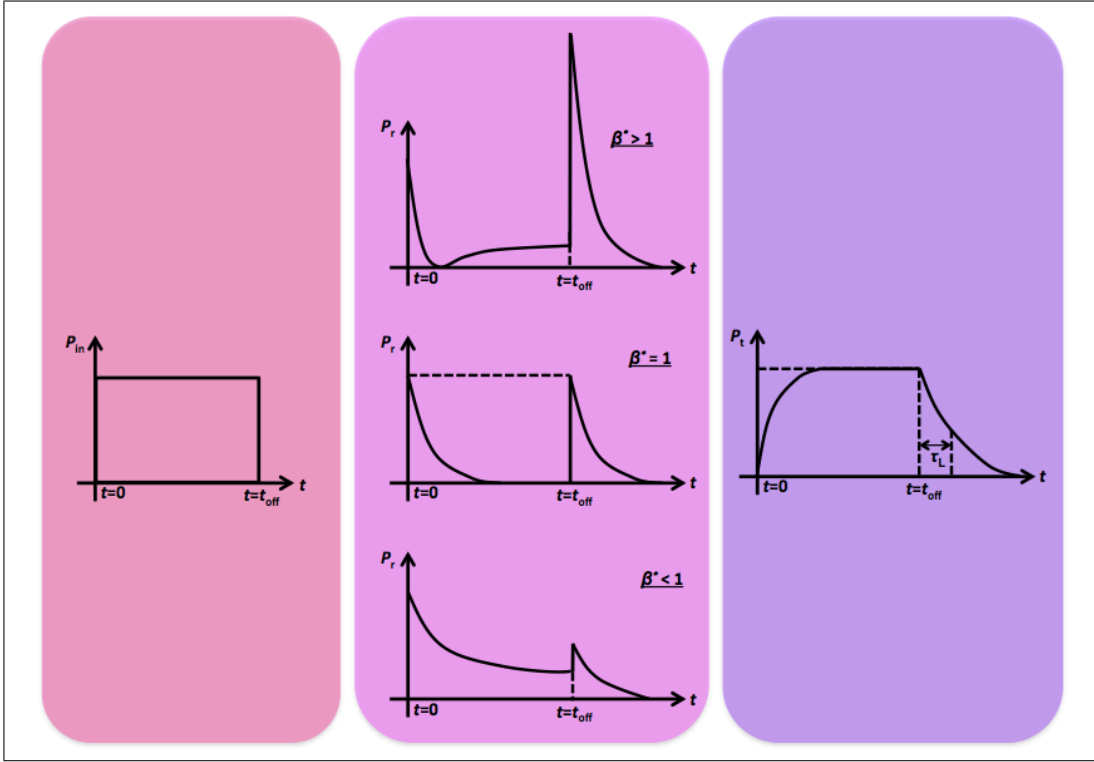


Figure B.2: Power responses to the pulsed input power.

are derived. From the above equation and Eq. (B.1.16),

$$P_r = \left( \frac{1 - \beta^* + 2\beta^* e^{-\lambda^* t}}{1 + \beta^*} \right)^2 P_{\text{in}} \quad (0 \leq t < t_{\text{off}}). \quad (\text{B.4.4})$$

is derived. Similarly, from Eq. (B.1.17), (B.1.18) and (B.4.1),

$$P_t = \frac{4\beta^* \beta_t (1 - e^{-\lambda^* t})^2}{(1 + \beta^*)^2} P_{\text{in}} \quad (0 \leq t < t_{\text{off}}) \quad (\text{B.4.5})$$

$$P_c = \frac{4\beta^* (1 - e^{-\lambda^* t})^2}{(1 + \beta^*)^2} P_{\text{in}} \quad (0 \leq t < t_{\text{off}}) \quad (\text{B.4.6})$$

are derived. Next, the case is considered that the switch turns off at  $t = t_{\text{off}}$ . In this case, the amplitude of  $V_c$  at  $t = t_{\text{off}}$  equals to the magnitude of Eq. (B.3.8), then

$$V_c \simeq \frac{2\sqrt{\beta^*}}{1 + \beta^*} \sqrt{R_a P_{\text{in}}} e^{-\lambda^*(t-t_{\text{off}})} e^{i(\omega t + \theta)} \quad (\text{B.4.7})$$

$$(\text{B.4.8})$$

is established. From Eq. (B.2.20), (B.4.7) and substituting  $V_{\text{in}} = 0$ ,

$$V_r = \sqrt{2z_0 P_{\text{in}}} \frac{2\beta^*}{1 + \beta^*} e^{-\lambda^*(t-t_{\text{off}})} e^{i\omega_0 t} \quad (t \geq t_{\text{off}}) \quad (\text{B.4.9})$$

is derived. From Eq. (B.1.16) and (B.4.9),

$$P_r(t) = \left( \frac{2\beta^*}{1 + \beta^*} \right)^2 e^{-2\lambda^*(t-t_{\text{off}})} P_{\text{in}} \quad (t \geq t_{\text{off}}) \quad (\text{B.4.10})$$

is derived. Similarly, from Eq. (B.1.11), (B.1.17), (B.1.18) and (B.4.7),

$$P_t = \frac{4\beta^* \beta_t}{(1 + \beta^*)^2} e^{-2\lambda^*(t-t_{\text{off}})} P_{\text{in}} \quad (t \geq t_{\text{off}}) \quad (\text{B.4.11})$$

$$P_c = \frac{4\beta^*}{(1 + \beta^*)^2} e^{-2\lambda^*(t-t_{\text{off}})} P_{\text{in}} \quad (t \geq t_{\text{off}}) \quad (\text{B.4.12})$$

are derived. Figure B.2) shows the various patterns of  $V_r$  whose amplitude at  $t = t_{\text{off}}$  is depend on  $\beta^*$ . The situation of  $\beta^* > 1$  is called “over-coupling” and  $\beta^* < 1$  is called “under-coupling”. Using the information of the  $P_r$  patterns, the coupling strength of  $\beta^*$  can be determined.

Moreover, measuring the decay slope of  $P_t$ , the loaded quality factor  $Q_0$  can be determined. From Eq. (B.4.11), the decay time  $t - t_{\text{off}} = \tau_L$  elapsed to reach a half value of the peak is expressed as

$$e^{-2\lambda^* \tau_L} = \frac{1}{2}. \quad (\text{B.4.13})$$

Then,  $Q_L$  is calculated as

$$Q_L \simeq 0.6931 \times \tau_L \times \omega_0. \quad (\text{B.4.14})$$

## B.5 Estimate $Q_0$ and $V_c$

Now, we know the coupling strength of  $\beta^*$  (overcooling or under-coupling) and the value of  $Q_L$ . In order to estimate the value of  $Q_0$ , it is necessary to estimate  $\beta^*$ . As described in Sec. B.3, the reflected power  $P_r$  in stationary states are given as

$$P_r = \left( \frac{1 - \beta^*}{1 + \beta^*} \right)^2 P_{in} \quad (\text{B.5.1})$$

which is already shown as Eq. (B.3.14). Solving this equation in terms of  $\beta^*$ ,

$$\beta^* = \frac{1 \pm \sqrt{\frac{P_r}{P_{in}}}}{1 \mp \sqrt{\frac{P_r}{P_{in}}}} \quad (\text{B.5.2})$$

is derived, where the upper double-sign corresponds is chosen for  $\beta^* \geq 1$  (over-coupling) and the down one is chosen for  $\beta^* < 1$  (under-coupling). Then, from Eq. (B.2.14), the value of  $Q_0$  is estimated. It should be noted that,  $Q_0$  is always changed because the dissipating power in the cavity  $P_c$  gets larger at a high accelerating field. On the other hand,  $Q_t$  and  $Q_e$  are static in the process of performance tests because  $U/P_t$  and  $U/P_e$  are determined only by the shape of the cavity.

The amplitude of the accelerating voltage  $|V_c|$  is estimated by Eq. (B.3.8) as

$$|V_c| = \frac{2\sqrt{\beta^*}}{1 + \beta^*} \sqrt{R_a P_{in}}. \quad (\text{B.5.3})$$

Using Eq. (B.4.11), Eq. (B.5.3) is expressed as

$$|V_c| = \sqrt{R_a P_t}. \quad (\text{B.5.4})$$

As Eq. (5.1.60), the accelerating field  $E_{acc}$  is expressed as

$$E_{acc} = \frac{\sqrt{R_a/Q_0}}{d} \sqrt{Q_t P_t}. \quad (\text{B.5.5})$$

There is a relation between  $E_{acc}$  and  $E_{ap}$  as

$$E_{ap} \propto E_{acc}, \quad (\text{B.5.6})$$

then  $E_{ap}$  is expressed as

$$E_{ap} = A \sqrt{Q_t P_t}, \quad (\text{B.5.7})$$

where  $A$  is a constant and can be estimated by the numerical simulation.



# Bibliography

- [1] A. Tonomura, et al., “Observation of individual vortices trapped along columnar defects in high-temperature superconductors”, *Nature*, vol412, 620-622, (2001)
- [2] X. Z. Yu, et al., “Real-space observation of a two-dimensional skyrmion crystal”, *Nature*, 465, 901, (2010)
- [3] F. N. Rybakov, et al., “New spiral state and skyrmion lattice in 3D model of chiral magnets”, *New J. Phys.* 18, 045002 (2016)
- [4] T. Akashi, et al., “Aberration corrected 1.2-MV cold field-emission transmission electron microscope with a sub-50-pm resolution”, *Applied Physics Letters*, 106, 074101, (2015)
- [5] 大木正路, ”高電圧工学”, 槇書店, (1982)
- [6] T. Akashi, et al., “Aberration corrected 1.2-MV cold field-emission transmission electron microscope with a sub-50-pm resolution (Supplementary material)”, *Applied Physics Letters* 106, 074101 (2015)
- [7] Nakamura et al., “Expandable Megakaryocyte Cell Lines Enable Clinically Applicable Generation of Platelets from Human Induced Pluripotent Stem Cells”, *Cell Stem Cell*, 14, 1-14, (2014)
- [8] M. Haider et al., “Electron Microscopy Image Enhanced”, *Nature* 392, 768, (1998)
- [9] M. Kuwahara, et al., “30-kV spin-polarized transmission electron microscope with GaAs-GaAsP strained superlattice photocathode”, *Appl. Phys. Lett.* 101, 033102, (2012)
- [10] Ray F. Egerton, “Physical Principles of Electron Microscopy -An Introduction to TEM, SEM, and AEM-”, Springer, (2005)
- [11] N. Yamamoto, et al., “High brightness and high polarization electron source using transmission photocathode with GaAs-GaAsP superlattice layers”, *JOURNAL OF APPLIED PHYSICS*, 103, 064905, (2008)
- [12] S. Pastuszka, et al., “Preparation and performance of transmission-mode GaAs photocathodes as sources for cold dc electron beams”, *JOURNAL OF APPLIED PHYSICS*, 88, 6788, (2000)

- [13] L. Reimer, H. Kohl, “Transmission Electron Microscopy -Physics of Image Formation-Fifth Edition”, Springer, (2008)
- [14] 田中信夫, “電子線ナノイメージング-高分解能 TEM と STEM による可視化-”, 内田老鶴圃, (2009)
- [15] M. Haider, et al., “Information Transfer in a TEM Corrected for Spherical and Chromatic Aberration”, Microscopy and Microanalysis, 16, 393-408, (2010)
- [16] PDG, “Particle Physics Booklet”, (2014)
- [17] 松葉俊哉, 本田洋介, “拡散モデルによるカソードの時間応答の計算”, KEK cERL internal report, (2010)
- [18] B. W. Reed et al. , “Electron Optical Requirements for Sub-Nanosecond Microscopy” , Microscopy and Microanalysis, Volume 11, Supplement S02, 1480-1481, (2005)
- [19] General Particle Tracer, “General Particle Tracer User Manual Version 2.82” , Pulser Physics, (2012)
- [20] William H. Press, Saul A. Teukolsky, William T. Vetterling and Brian P. Flannery, “Numerical Recipes in C++ Second Edition” , Cambridge University Press, (2002)
- [21] J. Bardeen et al. , “Microscopic Theory of Superconductivity” , Phys. Rev. 108:1175(1957)
- [22] 渡辺正, “元素大百科事典” , 朝倉書店, (2007)
- [23] ESPI Metals, “Technical Data Niobium” , <http://www.espimetals.com/index.php/technicaldata/170-niobium>, (2012)
- [24] W. M. Haynes et al. , “CRC handbook of Chemistry and Physics” , CRC Press, (2012)
- [25] Hasan Padamsee et al. , “RF Superconductivity for Accelerators” , (1998)
- [26] 齋藤健治, 東京大学大学院理学系研究科物理学専攻集中講義ノート, (2011)
- [27] K. Halbach and R. F. Holsinger, “SUPERFISH-A COMPUTER PROGRAM FOR EVALUATION OF RF CAVITIES WITH CYLINDRICAL SYMMETRY” , Particle Accelerators, Vol. 7, pp. 213 - 222, (1976)
- [28] P. Kneisel, “Surface Preparation of Niobium” , Proceedings of SRF Workshop 1980, (1980)
- [29] Y. Morita et al. , “ILC 超伝導加速空洞のための電解研磨法における研磨量の電極間距離依存に関する研究” , Proceedings of the 5th Annual Meeting of Particle Accelerator Society of Japan and the 33rd Linear Accelerator Meeting in Japan, (2008)

- [30] M. L. Kinter et al., “Chemical Polish for Niobium Microwave Structures”, J. Appl. Phys. 41, 828, (1970)
- [31] 日本工業規格, “B9920 クリーンルームの空気清浄度の評価方法”, (2002)
- [32] 日本工業規格, “K0552 超純水の電気伝導率試験方法”, (1994)
- [33] 国立天文台編纂, “理科年表平成5年”, 丸善株式会社, (1992)
- [34] HP, “HP 5350B/5351B/5352B マイクロ波周波数カウンタ 操作ガイド”, (1988)
- [35] M. Omet, “Doctoral Thesis, Digital Low Level RF Control Techniques and Procedures Towards the International Linear Collider”, (2014)
- [36] L. Bottura ,et al., “Superconducting Magnets for Particle Accelerators”, IEEE TRANSACTIONS ON NUCLEAR SCIENCE, VOL. 63, NO. 2, APRIL 2016, 751-776, (2016)
- [37] 中里俊晴, 博士論文 “超伝導 500MHz 加速空洞の研究”, (1981)



# Acknowledgement

This thesis would not have been accomplished without the supports of many people. I will express my gratitude to them.

First of all, I would like to express my deepest gratitude to my supervisor, Prof. Satoru Yamashita. He gave the opportunity to participate in this study, which became a desirable experience for me. He gave me a lot of advices and guidances through many discussions continuously, which always encouraged me to accomplish this study.

This study is carried out in High Energy Accelerator Research Organization (KEK). I would like to thank all members of the KEK research team.

I would like to express my special gratitude to Dr. Yukihide Kamiya. He gave me a lot of advices about the entire study, the presentations of the conferences and papers. Additionally, he spent an enormous amount of time to equip me the knowledge of accelerators. I would like to express my appreciation to Dr. Atsushi Enomoto. He gave me the knowledge about accelerators and shared his valuable experiences with Dr. Yukihide Kamiya. He also created a comfortable environment for me to study in KEK.

I would like to express my best gratitude to Prof. Takaaki Furuya for the development of the superconducting cavities. His knowledge and experience created in the longtime research in KEK led us to the success of the production of the unprecedented cavity. As well as the manufacturing the cavity, he gave me a technique of the vertical test of superconducting cavities. It was memorable that he and I carried out the performance tests late into the night. I would like to express my appreciation to Mr. Yoshisato Funahashi. He supported me at the every moment of manufacturing cavities, including EBW and polishing. I would like to thank Mr. Motoaki Sawabe for the support of the cavity polishing. With his extensive knowledge and experience, we performed the polishing of the complicated-shape cavity successfully. I would express my appreciation to Prof. Hiroshi Sakai and Dr. Michiru Nishiwaki for the support of the vertical tests of the cavities. Moreover, they helped me to carry out the study by teaching me about superconducting cavities.

I would like to express my special thanks to Prof. Shinichiro Michizono for the development of the feedback system. With his expertise of the feedback system, we realized the stable control system for the superconducting cavity. I also would like to express my thanks to Dr. Qiu Feng. He helped us to perform the feedback tests for a long time. With his dedicated cooperation, we measured the stability of our feedback system.

I would like to thanks to Dr. Masahiro Yamamoto. He is a expert of photocathode gun, and gave me a lot of guidance for the electron gun and the beam dynamic simulation. I

would also express my gratitude to Prof. Masao Kuriki of Hiroshima University, who taught me the implementation of the beam dynamics simulation.

I would like to express my special thanks to Mr. Yoichi Ose of Hitachi High-Technologies Corporation. He gave us a plenty of expertise of electron microscopy. In addition, I would like to thank Mr. Shigeto Isakozawa of Hitachi High-Technologies Corporation and Dr. Takeshi Kawasaki of Hitachi for their generous supports.

I would like to express my gratitude to Prof. Yukinori Kobayashi, Dr. Jacqueline Yan, Prof. Takako Miura, Dr. Jin Xiuguang, Prof. Tsukasa Miyajima of KEK, and Dr. Koji Kimono of National Institute for Materials Science.

I would like to express my thanks to all members of the Yamashita group of ICEPP in the university of Tokyo: Dr. Tomohiko Tanabe, Dr. Masakazu Kurata, Mr. Ryo Katayama, Mr. Takahito Yamada, Ms. Sei Ieki, Mr. Naoki Nagakura, Mr. Shohei Fujikura and Mr. Yu Kato. I would also express my gratitude to the old members of the Yamashita group: Prof. Kenji Mishima, Dr. Taikan Suehara, Dr. Takashi Kubota, Dr. Yuichi Morita, Dr. Hidetoshi Otono, Dr. Hideyuki Oide, Mr. Harumichi Yokoyama, Mr. Takuaki Mori and Mr. Kento Kasuya. I am honored to have been a colleague of them.

I would like to express my deepest gratitude to ICEPP secretaries during my belonging: Ms. Masako Shiota, Ms. Yoko Takemoto, Ms. Kayo Yamaura, Ms. Yoshie Tezuka, Ms. Akiko Miyazono, Ms. Ritsuko Ambiru, Ms. Megumi Suzuki. With their generous supports, I accomplished this study.

Finally, I would like to thank my mother Sakae and my father Toru, who have given me a plenty of opportunities and encouraged me all the time.